AD_________________

Award Number: W81XWH-09-1-0528

TITLE: Autophagy Signaling in Prostate Cancer: Identification of a Novel Phosphatase

PRINCIPAL INVESTIGATOR: Jeffrey P. MacKeigan, Ph.D.

CONTRACTING ORGANIZATION: Van Andel Research Institute
Grand Rapids, MI 49503

REPORT DATE: January 2013

TYPE OF REPORT: Final

PREPARED FOR: U.S. Army Medical Research and Materiel Command
Fort Detrick, Maryland 21702-5012

DISTRIBUTION STATEMENT: Approved for Public Release;
Distribution Unlimited

REPORT DOCUMENTATION PAGE	*Form Approved* *OMB No. 0704-0188*

1. REPORT DATE January 2013	**2. REPORT TYPE** Final	**3. DATES COVERED** 23 July 2009 – 22 January 2013

4. TITLE AND SUBTITLE

Autophagy Signaling in Prostate Cancer: Identification of a Novel Phosphatase

5a. CONTRACT NUMBER

5b. GRANT NUMBER
W81XWH-09-1-0528

5c. PROGRAM ELEMENT NUMBER

6. AUTHOR(S)
MacKeigan, Jeffrey P., Ph.D.
Martin, Katie R., Ph.D.

E-Mail: jeff.mackeigan@vai.org

5d. PROJECT NUMBER

5e. TASK NUMBER

5f. WORK UNIT NUMBER

7. PERFORMING ORGANIZATION NAME(S) AND ADDRESS(ES)

Van Andel Research Institute
333 Bostwick Ave NE
Grand Rapids, MI 49503-2518

8. PERFORMING ORGANIZATION REPORT NUMBER

9. SPONSORING / MONITORING AGENCY NAME(S) AND ADDRESS(ES)
U.S. Army Medical Research and Materiel Command
Fort Detrick, Maryland 21702-5012

10. SPONSOR/MONITOR'S ACRONYM(S)

11. SPONSOR/MONITOR'S REPORT NUMBER(S)

12. DISTRIBUTION / AVAILABILITY STATEMENT
Approved for Public Release; Distribution Unlimited

13. SUPPLEMENTARY NOTES

14. ABSTRACT

Phosphatidylinositol-3-phosphate (PI(3)P) is concentrated on endocytic and autophagic vesicles and recruits effector proteins critical for these processes. In an effort to understand the phosphatase regulation of PI(3)P, we performed an RNA interference (RNAi) screen and found that knockdown of PTPRS (PTPsigma), a dual-domain protein tyrosine phosphatase (PTP), increases cellular PI(3)P and hyperactivates both constitutive and induced autophagy. We have found that PTPsigma localizes to PI(3)P-positive membranes in cells and its vesicular localization is enhanced during autophagy. Furthermore, PTPsigma is proteolytically processed from its location at the cell surface into a membrane-bound C-terminal fragment, which appears to be targeted to the lysosome. Taken together, our findings propose a novel role for PTPsigma and provide insight into the regulation of PI(3)P and autophagy. Intriguingly, we have previously demonstrated that RNAi-mediated knockdown of PTPsigma confers chemoresistance to cancer cells in culture. In addition, reduced expression of PTPsigma was found during the progression from primary prostate cancer to metastatic disease. Accordingly, our central hypothesis is that autophagy is activated in the absence of PTPsigma as a mechanism of chemoresistance, thereby densensitizing prostate cancer cells to chemotherapeutic stress and supporting disease progression.

15. SUBJECT TERMS
Autophagy, prostate cancer, phosphatase, lipid signaling

16. SECURITY CLASSIFICATION OF:			**17. LIMITATION OF ABSTRACT**	**18. NUMBER OF PAGES**	**19a. NAME OF RESPONSIBLE PERSON** USAMRMC
a. REPORT U	**b. ABSTRACT** U	**c. THIS PAGE** U	UU	72	**19b. TELEPHONE NUMBER** *(include area code)*

Table of Contents

Appendices

INTRODUCTION:

The concept of prostate tumor development as a multi-step process has been well documented. Analysis of human prostate cancer specimens has revealed a variety of deviant tissue states, from early carcinomas and highly malignant tissue, to invasive carcinoma and distant metastases. The many steps of prostate cancer tumor progression are evident from the accumulation of mutant genes in cells as they evolve from a benign to a malignant state. The loss of PTEN (chromosome 10q), pRB (chromosome 13q) and p53 (chromosome 17p) is coupled with a large percentage of tumors harboring Myc amplifications, AR mutations and Bcl-2 overexpression [1-4]. In agreement with this, our data indicate a stage or metastasis-dependent loss of PTPsigma (PTPRS) mRNA. Importantly, we have previously discovered that loss of PTPsigma expression promotes resistance to several chemotherapeutics [5]. In the work supported by this grant, we have demonstrated that loss of PTPsigma hyperactivates autophagy, a cell survival program that promotes cell survival and drug resistance. Taken together, these data suggest that PTPsigma may be involved in prostate progression, perhaps through activation of autophagy-mediated chemoresistance after loss of PTPsigma.

Here, we summarize our efforts to investigate the role of PTPsigma in autophagy and prostate cancer progression throughout the entire funding period. Figures referenced for all tasks outlined in the Statement of Work include unpublished data (Figures 1-6 in the *Supplementary Data*) as well as those published within the articles attached in the *Appendix* [4, 6-8]. In addition, we make reference to data presented in prior annual reports.

BODY:

Aim #1: Identify the catalytic mechanism whereby PTPRS regulates PI(3)P levels.

We first uncovered a role for PTPsigma in PI(3)P signaling when we observed that PTPsigma knockdown significantly increased the abundance of PI(3)P-positive vesicles in cells (**Fig. 1 of [5])**. This observation, and subsequent experiments, led to the hypothesis that PTPsigma may control PI(3)P through direct dephosphorylation. To test this hypothesis, we generated recombinant PTPsigma in both wildtype and catalytically inactive protein tyrosine phosphatase (PTP) domains. Specifically, we utilized site-directed mutagenesis to introduce point mutations into the D1 (C1589S), D2 (C1880S), and both D1 and D2 PTP domains (*task 1*). These mutations were sequence-verified and characterized for phosphatase activity *in vitro* (*task 2*). In addition to inserting these constructs into mammalian expression vectors, used throughout most of the work presented here, each construct was subcloned into bacterial vectors (pGEXKG) for recombinant protein purification. We enzymatically characterized PTPsigma using a colorimetric phosphatase substrate, pNPP, and determined its Km towards this substrate to be ~ 250 µM, very similar to a well-characterized PTP, PTP1B (**Fig. 1A-C of 2012 Annual Report**). To determine which domain (D1 or D2) of PTPsigma this activity could be attributed to, we measured the activity of wildtype or mutant PTPsigma using a phospho-tyrosine (pTyr) peptide and malachite green free phosphate detection. We confirmed that the catalytic activity resides exclusively within the D1 domain (**Fig. 1D of 2012 Annual Report**). In contrast to PTPsigma activity towards protein substrates, we have failed to detect robust PI(3)P-phosphatase activity after extensive investigation using standard lipid phosphatase assays (**Fig. S3 of [6]**).

This finding has prompted us to explore alternative hypotheses, as outlined in *Potential Pitfalls and Alternative Approaches* of Aim 1. Specifically, we have determined that PTPsigma knockdown increases the abundance of several tyrosine-phosphorylated proteins in U2OS cells. The identity of such proteins, which represent potential substrates of PTPsigma, can be pursued using mass spectrometry, a technique we have recently utilized [7]. In this study, we confirmed the endocytic localization of PTPsigma, consistent with our observations that it regulates cellular PI(3)P dynamics [7]. In addition, we have utilized recombinant protein substrate trapping techniques to enrich for proteins that associate with the D1 active site of PTPsigma. We are actively investigating the hypothesis that PTPsigma may elicit its control of PI(3)P by directly regulating VPS34 or a VPS34-associated protein. These experiments are ongoing and the focus of new laboratory projects.

Next, we sought to investigate the hypothesis that loss of PTPsigma hyperactivates autophagy. To this end, we have completed a number of autophagy assays including LC3 Western blots (*task 4*) and immunofluorescence for endogenous LC3 (*task 5*) (**Figs. 1, 2, S2 of [6]**). We have monitored autophagic vesicles by electron microscopy (*task 6*) at the Michigan State University Center for Advanced Microscopy (**Fig. 3 of [6]**). We have also quantified the number of autophagic vesicles per cell, for both cells containing wild-type PTPsigma and those subjected to siRNA-mediated knockdown of PTPsigma (*task 7*) (**Figs. 2, S2 of [6]**). This work is described in more detail within the attached referenced article **[6]**. Of note, the development and refinement of these assays allowed us to contribute to a collaborative manuscript [8].

With this data and model in place, we began to investigate the contribution of PTPsigma to autophagy in prostate cancer. We began by surveying a panel of metastatic prostate cancer cell lines for their relative level of autophagic flux. We measured LC3-II formation and turnover under conditions of basal and induced autophagy in PC3, DU145, LNCaP, and C4-2B cells (**Fig. 2A-B of 2012 Annual Report**). The results of these experiments suggest that *a)* PC3 cells contain abundant LC3 that is conjugated to autophagic vesicles (processed into LC3-II) and delivered to lysosomes; *b)* DU145 cells, in our hands, fail to form LC3-II in response to autophagy stimuli or lysosome inhibition; *c)* LNCaP and the spontaneously metastatic derivative, C4-2B, have similar levels of dynamic autophagic flux as determined by LC3-II formation and accumulation upon lysosome inhibition. Consistent with our data, a recent publication reported a similar autophagic defect in DU145 cells, which they determined was a result of a lack of full-length ATG5 expression, an autophagy protein required for LC3 conjugation [9]. We proposed to focus on C4-2B cells *in vivo* because this line forms primary prostate tumors and metastasizes to the lungs and bone within 10 weeks of injection in SCID mice [10-13]. The functional autophagy observed in C4-2B cells supports this choice as a model as we investigate autophagy in prostate cancer *in vivo*. To begin to establish the role of PTPsigma in C4-2B cells, we again used LC3 immunoblotting to analyze autophagic flux. As in U2OS cells, we found that loss of PTPsigma caused an increased accumulation of endogenous LC3 in response to lysosome inhibition, consistent with a hyperactivation of autophagy (**Fig. 2C of 2012 Annual Report**). For this Aim, the *task 3* includes testing the mutants in C4-2B cells to determine the necessity of the active site in prostate cancer cells, as compared to immortalized normal PEC36 prostate cells. We generated stable cell lines lacking PTPsigma expression (by shRNA) or exogenously expressing PTPsigma (wild-type or active site mutants). Western blot analysis was used to confirm the desired PTPsigma expression in these lines **(Fig. 1A-B).**

It is important to note that we developed several small molecule inhibitors of PTPsigma [4]. These compounds directly inhibit the catalytic activity of PTPsigma *in vitro*, and ongoing efforts are aimed to improve the selectivity of these agents while assessing their utility in cells. These molecules may serve as useful chemical tools for our continued investigations into the role of PTPsigma in prostate cancer progression.

Aim #2: Determine the regulation and subcellular localization of PTPRS during autophagy.

In order for PTPsigma to regulate PI(3)P dynamics and autophagy, it must become internalized from the cell surface to be in proximity of PI(3)P-positive vesicles. PTPsigma has been previously reported to shed its ectodomain and internalize from the cell surface as a membrane-bound C-terminal fragment (CTF) [14]. The intracellular destination of this CTF, and any further processing to a soluble intracellular domain (ICD), has not been studied. We aimed to determine if PTPsigma exists as a CTF and/or ICD in our cell model, and if autophagy induction triggers proteolytic changes in PTPsigma.

To this end, we expressed full-length untagged exogenous PTPsigma in U2OS cells and used western blots to determine the presence of all potential fragments– the pro-subunit, P-subunit, CTF, and ICD – each distinguished by a unique molecular weight of ~170 kDa, 85 kDa, 76 kDa, and 72 kDa, respectively (*task 1;* **Fig. 3 of 2012 Annual Report**). Because processing into each of these forms occurs upstream of the D1 domain, we used a D1-directed antibody for detection. First, we analyzed basal processing of PTPsigma which occurs during normal growth conditions. We found that PTPsigma exists predominantly as a full-length pro-subunit and as a cell surface-expressed P-subunit. When lysosomes were inhibited with bafilomycin A1 (BafA1), a smaller band of a molecular weight consistent with a CTF appeared within 15 to 30 minutes and accumulated kinetically. To determine if this fragment was in fact processed from the P-subunit , we inhibited extracellular metalloproteases responsible for P-subunit-to-CTF processing using a small molecule inhibitor, Batimastat [15]. In contrast to the vehicle control, cells pre-treated with Batimastat failed to produce this fragment, supporting its identity as a processed P-subunit fragment, likely a CTF. To determine if PTPsigma processing is altered during autophagy induction, we kinetically starved cells of amino acids and probed for PTPsigma fragments. Starvation induced the generation of a novel PTPsigma fragment of lower molecular weight than the putative CTF. When cells were concurrently starved of amino acids and treated with BafA1, the apparent CTF accumulated once again, but this smaller fragment did so only slightly if at all. This suggests that although the membrane-bound CTF is degraded in the lysosome, this novel fragment is likely not regulated in the same manner. Importantly, we have also observed the same accumulation of the PTPsigma CTF in response to lysosome inhibition in C4-2B cells, suggesting this processing is also relevant in prostate cancer cells (**Fig. 3**).

We monitored PTPsigma localization using standard immunofluorescence microscopy. We introduced full-length, untagged PTPsigma into both U2OS and C4-2B cells and followed the C-terminus using D1-targeted monoclonal antibodies (*task 5*). This was a refinement of the original approach using C-terminal V5-tagged PTPsigma. We compared PTPsigma distribution to both EGFP-2xFYVE and RFP-labeled LC3 to find PTPsigma on both PI(3)P and LC3-positive vesicles (*task 6*) (**Figs. 4, 5, S3 of [6]**). We assessed the enrichment of PTPsigma in an autophagic fraction during autophagy by comparing cells cultured in full nutrients to those starved of amino acids (*task 8*). We hypothesized that PTPsigma would be similarly localized to intracellular vesicles in C4-2B cells and tested this prediction. Again, full-length untagged PTPsigma was transfected into C4-2B cells and its localization assessed by immunostaining with

D1-targeted antibodies. We observed wildtype PTPsigma to localize in a perinuclear compartment, likely representing the ER and/or golgi where it is produced and processed, as well as numerous intracellular vesicles. Introduction of an inactivating mutation in the D1 active site (C1589S) did not affect the localization of PTPsigma. As observed in U2OS cells, treatment with the lysosome inhibitor, Bafilomycin A1, increased the abundance of vesicular PTPsigma, suggesting PTPsigma may normally be turned over in the lysosome (**Fig. 4 of 2012 Annual Report**). Finally, we completed numerous autophagy assays which we will continue to pursue in prostate cancer cells (*task 2, task 3, task 4*) (**Fig. 2C of 2012 Annual Report; Figs. 1-3, S2 of [6]**).

Task 7 includes the isolation of autophagosomes by differential centrifugation from cells. We optimized this protocol and confirmed the identity of fractions. We feel our extensive immunofluorescent assays have localized PTPsigma to intracellular compartments sufficiently and do not see the value in conducting the immunogold electron microscopy (*task 9-10*). When using primary and secondary antibodies labeling, an inherent limitation is that the gold particle can be over 30 nm away from the site to which the primary antibody is bound; therefore, the precise location of PTPsigma would not be further elucidated.

Specific Aim #3: Establish the role of PTPRS in prostate cancer chemoresistance.
The purpose of this Aim is to evaluate the role of PTPsigma in prostate cancer chemoresistance using an androgen-independent C4-2B metastatic model of prostate cancer. We originally proposed to generate stable C4-2B cell lines expressing EGFP; however, we modified this approach to use a more sensitive *in vivo* tracer (*task 1*). We obtained a C4-2B cell line stably expressing luciferase (C4-2B-luc) from Dr. Evan Keller, who has successfully used this and similar lines to investigate prostate cancer using murine models [16]. The luciferase expressed in cells utilizes a luciferin substrate to catalyze a light-producing reaction. This emitted light can be detected and quantified by bioluminescent imaging (BLI), which we have purchased during this award period and optimized in our Small Animal Imaging Facility.

We established stable C4-2B-luc cell lines with altered PTPsigma expression. In addition to a C-terminal fragment of PTPsigma (**Fig. 1A**), we introduced full-length PTPsigma into C4-2B-luc cells using viral vectors and infection (**Fig. 4D of 2012 Annual Report**). Both the pro-subunit and P-subunit can be easily detected by immunoblotting, above the endogenous level which is very low, as we would predict for a metastatic prostate cancer cell line. These constructs are present in both wildtype and catalytically inactive (D1, D2, or both D1 and D2) forms. To complement exogenous expression studies, we stably introduced shRNA constructs targeting PTPsigma into C4-2B-luc cells. As observed with two unique shRNA sequences, we can effectively reduce the level of endogenous PTPsigma (**Fig. 1B**). These cell lines have been characterized for growth and autophagic properties *in vitro* and are critical for use *in vivo*, as described below.

We completed a series of *in vivo* studies to optimize the orthotopic injection of C4-2B-luc cells into the prostate gland of athymic nude mice (*task 2*). While optimizing surgical technique to ensure the safety and recovery of animals, we determined that $1x10^6$ cells, prepared individually in separate syringes for each animal, yields robust and consistent tumor growth. Tumors can be detected within 2 weeks post-injection and we observed a 100% take-rate for tumor initiation.

We monitored tumor growth using both ultrasound and BLI. Specifically, we used the dimensions derived from ultrasound images to calculate and monitor tumor volume as a function of time, out to 9 weeks post-injection (**Fig. 5A-B of 2012 Annual Report**). Similarly, we imaged animals using BLI through 9 weeks post-injection and plotted RLU across time (**Fig. 5C-D of 2012 Annual Report**). We observed a positive correlation between BLI measurements and ultrasound dimension, fostering confidence in using BLI as a primary method to monitor tumors throughout the remainder of the study.

Tumors from mice were harvested and used to optimize immunohistochemistry (IHC) protocols. Compared to the normal architecture of the prostate epithelium, we observed a complete ablation of this cellular organization in favor of a highly proliferative, hypervascular primary tumor which invaded both the normal prostate and the surrounding mouse stroma (**Fig. 6A-B of 2012 Annual Report**). While vasculature was present throughout, overall integrity of these vessels was limited and as a result primary tumors contained areas of necrosis. Taken together, these findings suggest tumors had outgrown their blood supply. We confirmed minimal apoptosis (cleaved caspase 3), and a high level of proliferation and aggressiveness (Ki67) in orthotopic tumors (**Fig. 6C-D of 2012 Annual Report**). To confirm that these cells were the C4-2B-luc cells injected orthotopically into the prostate gland, we immunostained for the human specific marker, MHC class I and firefly luciferase (**Fig. 6E-F of 2012 Annual Report**). Throughout these studies, we optimized two antibodies as indicators: LC3B (discussed previously) and p62 (a cargo of the autophagosome and direct LC3 interactor). We stained tumors with LC3B and observed detectable staining, including many cells with intracellular punctae (**Fig. 6G of 2012 Annual Report**).

Importantly, we observed micrometastases in the lung tissue harvested from all mice that developed primary tumors in our studies. These metastases were observed as small clusters of large cells with substantial nuclei which stained positive for firefly luciferase (**Fig. 6H-I of 2012 Annual Report**). All animals developed tumors detectable by BLI within 2 weeks of injection and met criteria for euthanasia by 9 weeks. The micrometastases also occurred during this time frame.

Having implemented a model of prostate tumor growth and metastasis in our laboratory, we next determined the consequences of PTPsigma knockdown on tumor growth and metastasis. C4-2B-luc cell lines stably expressing a control shRNA, or one of two PTPsigma-direct shRNAs (shRNA sequence #1 and #3; those assessed in **Fig. 1B**), were injected into the prostate glands of athymic nude mice, along with a PBS mock injection control. Five mice were injected per group (n=20 for the experiment) and tumor growth was monitored weekly by BLI. This shRNA-based approach was in addition to the original proposed work which we feel is a natural extension from our siRNA work in cultured cells, and an informative complement to the exogenous PTPsigma experiments. In this study, we found that tumor growth was heightened in animals injected with PTPsigma shRNA-expressing cells. Specifically, 4 weeks after implantation, 20% of animals from each PTPsigma shRNA-expressing group (shRNA #1 and #3) had primary tumors that exceeded $1x10^5$ RLU as measured by BLI (**Fig. 4A-B**). In contrast, no control shRNA animal tumors exceeded this threshold, even 8 weeks after implantation (**Fig. 4C-D**). Furthermore, when we analyzed the distribution of tumors according to luminescence, we observed a shift towards larger RLU values from 4 weeks to 8 weeks post-injection for both PTPsigma shRNA groups, but not for the control shRNA group (**Fig. 4B, D**).

After assessing primary tumor growth, we investigated the presence of micrometastases in the lungs of several tumor-bearing animals. We found that metastases, identified by positive staining with firefly luciferase antibodies, were present in all tumor-bearing animals evaluated. However, while relatively few metastatic foci were present in control shRNA and PTPsigma shRNA #1 animals, they were considerably more abundant in animals harboring tumors driven by C4-2B-luc cells expressing PTPsigma shRNA #3 (**Fig. 6B**). It must be noted that only a single experimental animal from in the PTPsigma shRNA #1 group was analyzed for metastases (having met criteria for euthanasia). Therefore, it is difficult to make general conclusions about this group given the biological variability we would expect within a single group. Ongoing analysis of the remaining animals from this group will determine the incidence of metastasis associated with PTPsigma shRNA #1. If it remains true that there is a divergent metastatic phenotype between the individual PTPsigma shRNA sequences, this may reflect different levels of stable PTPsigma knockdown over time *in vivo*, or different cellular properties conferred by each shRNA. In fact, when the growth properties of each cell line were evaluated in culture using a real-time impedance assay, we found that cells expressing PTPsigma shRNA #3 proliferate more rapidly than both control and PTPsigma shRNA #1 expressing cells (**Fig. 2**). PTPsigma shRNA #1 confers a proliferative advantage over control cells, albeit much more modest than shRNA #3. Accordingly, it is possible that the more robust tumor growth and metastatic potential induced by PTPsigma shRNA #3 *in vivo* may stem from this substantially heightened proliferation. Finally, while the cellular impedance (xCELLigence) platform is commonly used to measure proliferation, cell index results do not account for potential changes in cell size or positions within the cell cycle. Therefore, we will complement this data with more standard approaches used for investigating cell proliferation.

It is important to note that when analyzing the presence of lung metastases, we observed a positive correlation between the size of the primary tumor and the incidence of metastatic foci, regardless of shRNA. This suggests that growth and progression of the primary tumor may be a key determinant of metastasis in this model. This is in agreement with published data reporting the considerable metastatic potential of C4-2B cells, a cell line originally derived from a metastatic lesion [10-13].

Next, we examined whether PTPsigma knockdown altered the autophagic properties of tumors *in vivo*. To this end, we analyzed two autophagy-specific markers, LC3B (described earlier) and p62, a protein that directly binds LC3 and recruits cargo into the autophagosome, by IHC. We found considerable heterogeneity in LC3B staining throughout individual tumors, suggesting autophagy may be differentially activated in certain subsets of the tumor. Overall, we observed an increase in granular LC3B-staining in PTPsigma shRNA-expressing tumors, compared to control shRNA tumors, which showed primarily diffuse cytoplasmic staining of LC3B (**Fig. 5A**). We found very little p62 staining in any tumor, suggesting p62 expression may be low or the autophagic cargo protein may be efficiently turned over in these tumors (**Fig. 5B**).

We have now initiated a follow-up *in vivo* study to investigate how PTPsigma expression affects chemosensitivity *in vivo*. In this study, mice are randomly assigned to treatment groups (n=10 each) 4 weeks after orthotopic injection (when tumors are at approximately 100 mm^3). Each group of mice are then treated by intravenous injection with vehicle or docetaxel (low and high dose) (*task 3*). Injections are continued for three weeks, after which, mice will be euthanized and tumors dissected (*tasks 3-5*). As we have done thus far, lungs will be excised, fixed, and micrometastases quantified (*task 7*) and tissues analyzed by immunohistochemistry (*tasks 7, 10*) This strategy will be followed using stable clones expressing high levels of wildtype, D1-inactive (C1589A), or D2-inactive (C1880A) PTPsigma (*tasks 8-9*). Protocols for all tasks have been approved by the IACUC committee at VAI. Owing to the success of the orthotopic model of prostate tumor growth and metastasis, we are satisfied using intratibial inoculation of C42B-luc cells, which will allow us to determine the role of PTPsigma in prostate cancer pathogenesis. However, in the event that we have difficulty establishing tumors or driving metastasis using PTPsigma-modulated cells, we will use these to directly inoculate cells in the tibia (a technique we have optimized) and quantify tumor burden in this metastatic relevant site after docetaxel treatment (*task 11-14*).

To establish working concentrations of taxol for our preliminary investigations of chemoresistance, we treated the C4-2B-luc cell line with a range of taxol doses for 48 hours and measured viability (**Fig. 7A**). At the highest dose used (175 nM), we observed less than a 50% decrease in viability, suggesting a high rate of C4-2B-luc survival in the face of taxol exposure. To determine if autophagy was activated by taxol treatment, which may contribute to cell survival, we monitored autophagic flux during treatment. Briefly, cells were treated for 1 to 4 hours with taxol or a vehicle control in the presence or absence of bafilomycin A1 to assess LC3-II accumulation as an indicator of autophagic flux. We found that taxol increased the amount of LC3-II accumulation in response to bafilomycin A1 treatment, suggesting this treatment increases autophagic flux (**Fig. 7B**). This observation supports our overarching hypothesis that chemotherapeutics activate autophagy as a means of acquired drug resistance and cancer cell survival. Moreover, this finding supports the investigation of PTPsigma and autophagy in taxane resistance and tumor progression *in vivo*.

KEY RESEARCH ACCOMPLISHMENTS:

- RNAi screen identifies PTPsigma as a modulator of PI(3)P signaling
- Loss of PTPsigma hyperactivates constitutive and induced autophagy
- PTPsigma localizes to PI(3)P-positive vesicles and rescues the siRNA phenotype
- The vesicular localization of PTPsigma does not require PI(3)P
- PTPsigma harbors robust protein tyrosine phosphatase activity, but not PI(3)P-phosphatase activity, and this is harbored within the D1 PTP domain
- PTPsigma is processed into a CTF during constitutive autophagy and targeted to the lysosome in U2OS and C4-2B cells
- PTPsigma is processed into a putative ICD during starvation-induced autophagy
- PTPsigma localizes to intracellular vesicles in the metastatic prostate cancer cell line, C42B, and these vesicles accumulate upon lysosomal inhibition
- Stable C42B cell lines have been generated expressing wildtype or mutant PTPsigma, or shRNAs targeting PTPsigma
- Luciferase-expressing C42B cells can be injected orthotopically into the prostate epithelium and develop tumors, detectable by BLI, within 2 weeks of injection

- All mice injected with wild-type luciferase-expressing C42B cells develop primary tumors and 100% have developed micrometastases, detectable by immunohistochemistry of harvested lung tissue
- shRNA-mediated knockdown of PTPsigma in C4-2B-luc cells may increase tumor growth when injected orthotopically into prostates and may facilitate metastases to the lungs
- PTPsigma knockdown may increase punctate (autophagic) LC3 staining in primary C4-2B-luc tumors
- Taxol increases autophagy in C4-2B-luc cells in culture

REPORTABLE OUTCOMES:

Publications

Martin KR, Xu Y, Looyenga BD, Davis RJ, Wu CL, Tremblay ML, Xu HE, MacKeigan JP (2011). Identification of PTPsigma as an autophagic phosphatase. *J Cell Sci*. 2011 Mar 1;124(Pt 5):812-9.

He Y, Xu Y, Zhang C, Gao X, Dykema KJ, Martin KR, Ke J, Hudson EA, Khoo SK, Resau JH, Alberts AS, MacKeigan JP, Furge KA, Xu HE. Identification of a lysosomal pathway that modulates glucocorticoid signaling and the inflammatory response. *Sci Signal.* 2011 Jul 5;4(180):ra44

Looyenga, BD and Mackeigan JP. Characterization of Differential Protein Tethering at the Plasma Membrane in Response to Epidermal Growth Factor Signaling. *J Proteome Res.* 2012.

Martin KR, Narang P, Xu Y, Kauffman AL, Petit J, Xu HE, Meurice N, and MacKeigan JP. (2012) Identification of Small Molecule Inhibitors of PTPsigma through an Integrative Virtual and Biochemical Approach. *PLoS ONE* 7(11): e50217. doi:10.1371/journal.pone.0050217

List of personnel (receiving pay from the research effort)

Jeffrey P. MacKeigan, PhD, Principal Investigator
Katie R. Martin (Sian), PhD, former Graduate Student, Michigan State University
Megan L. Goodall, BS, Graduate Student, Michigan State University

Abstracts/Presentations

Martin KR, Narang, P, Xu Y, Kauffman AL, Petit J, Xu HE, Meurice N, and MacKeigan JP, 2011. In silico-based identification of small molecule inhibitors targeted to PTPsigma. TGen/VARI Scientific Retreat, Phoenix, AZ (*Poster*)

Martin KR, Xu Y, Looyenga BD, Davis RJ, Wu CL, Tremblay ML, Xu HE, Mackeigan JP, 2011. Identification of PTPsigma as an autophagic phosphatase. AACR 102nd Annual Meeting, Orlando, FL (*Poster*)

Martin KR, Xu Y, Looyenga BD, Davis RJ, Wu CL, Tremblay ML, Xu HE, Mackeigan JP, 2011. Identification of PTPsigma as an autophagic phosphatase. 2011 US Department of Defense PCRP Impact Conference, Orlando, FL (*Poster*)

Martin KR, 2010. Identification of PTPsigma as an autophagic phosphatase. VARI/TGen Scientific Retreat, Thompsonville, MI (*Presentation*)

Martin KR, 2010. Identification of PTPsigma as an autophagic phosphatase. MSU Annual CMB/Genetics Retreat, Laingsburg, MI (*Presentation*)

Degrees obtained

Katie R. Martin, Doctorate of Philosophy, Cell and Molecular Biology, Michigan State University, August 2011

Cell lines developed

Modified C42B luciferase-expressing cells:
  Stable PTPsigma shRNA cell line
  Stable cell lines with exogenous expression of PTPsigma (wild-type and catalytically inactive)

CONCLUSION:

Through use of a high-content cell-based RNAi screen, we have identified phosphatases whose knockdown elevates cellular PI(3)P. Notably, RNAi-mediated knockdown of PTPsigma caused a striking increase in intracellular PI(3)P-positive vesicles which phenocopied that of an autophagic cell. We confirmed hyperactive autophagy in the absence of PTPsigma through use of multiple autophagy markers, as well as electron microscopy. ATG12 and LC3-positive autophagic vesicles were substantially more abundant in the absence of PTPsigma when cells were cultured in full nutrients (constitutive AVs) or treated with rapamycin (induced AVs). These autophagic vesicles accumulated upon treatment with the lysosomal inhibitors, Baf-A1 and chloroquine, demonstrating that they were functional and destined for lysosomal degradation. This phenotype suggests PTPsigma regulates an early step in autophagy induction and its loss results in increased autophagic vesicle generation. This is consistent with the fact that PI(3)P is generated on early phagophores and is required for proper autophagic vesicle formation. A role for PTPsigma in autophagy induction and specifically, PI(3)P regulation, is supported by our findings that PTPsigma localizes to PI(3)P-positive vesicles which increase in number during autophagy.

It remains to be addressed how PTPsigma is targeted to autophagic vesicles. PTPsigma is expressed at the cell surface in a two subunit complex comprised of a large ectodomain and a membrane-spanning intracellular domain. Accordingly, it is implicated in cell-cell and cell-ECM interactions, and it is a critical regulator of axon homeostasis and neuronal development [14, 17-19]. Relevant to our own work, ectodomain shedding and internalization of a membrane-bound carboxy-terminal fragment has been demonstrated previously [14]. Through immunofluorescent analysis of PTPsigma using D1 domain-specific antibodies, we place intracellular PTPsigma on PI(3)P-positive autophagic vesicles, a localization observed in both U2OS and C4-2B cells, among others. Autophagosomes frequently fuse with endosomes during their maturation, forming hybrid organelles called amphisomes, establishing the possibility that PTPsigma is internalized by endocytosis to arrive at autophagic vesicles [20]. Further, the close relative of PTPsigma, LAR (PTPRF), undergoes an additional proteolytic event whereby a soluble intracellular domain is formed and targeted inside the cell, similar to the Notch receptor [15].

PTPsigma contains similar cleavage residues to LAR, making it therefore plausible that PTPsigma is targeted from the plasma membrane to autophagic vesicles through a series of proteolytic events in response to autophagic stimuli. Thus, this phosphatase may serve several unique functions during various cellular conditions which are governed by its subcellular localization.

A critical finding presented here is the recruitment of PTPsigma to vesicular structures during amino acid-starvation which occurs even in the absence of PI(3)P generation. This finding, together with the hyperactivation of autophagy elicited by PTPsigma knockdown (as measured by PI(3)P, ATG12, and LC3), suggests PTPsigma regulates autophagy at an early step upstream of this lipid. In further support of this, we found that while almost all PTPsigma-positive vesicles are also positive for PI(3)P (EGFP-2xFYVE presence), fewer harbored LC3, a marker which is incorporated into AVs at later maturation stages.

There are several potential mechanisms by which PTPsigma may function to regulate autophagy. First, it is possible that PTPsigma could directly dephosphorylate PI(3)P following recruitment to AVs. We did test the activity of recombinant PTPsigma in vitro, and while we could not detect PI(3)P-phosphatase activity, it cannot be entirely excluded that PI(3)P does not serve as a direct substrate *in vivo*. It is also possible that PTPsigma uses its robust protein phosphatase activity to regulate the function of a PI(3)P-modifying enzyme, such as a PI(3)P-phosphatase or a PI(4)- or PI(5)-kinase. Alternatively, PTPsigma could control the activity of VPS34, which contains at least one phosphotyrosine site, or another component within the larger VPS34 complex [21]. Finally, PTPsigma may contribute to the regulation of autophagy at the earliest initiation step, which is executed by a complex of autophagy proteins, namely ULK1 and ATG13. The functional formation of this complex, which permits the generation of the PI(3)P-positive phagophore, is tightly regulated by phosphorylation events [22-25]. The aim of future work will be to determine the precise mechanism by which PTPsigma functions to regulate autophagy.

We also found that PTPsigma was processed from its P-subunit into a putative C-terminal fragment (CTF). This processing occurs under normal growth conditions and results in CTF targeting and turnover in the lysosome. Further, we uncovered evidence that PTPsigma is processed into a fragment smaller than the CTF during starvation-induced autophagy. This fragment does not appear to be targeted to the lysosome and while it is logical to assume it is an ICD, its molecular weight is smaller than that reported for a LAR ICD [26]. PTPsigma does in fact have residues that are similar to those in Notch that are required for gamma-secretase-mediated ICD formation [27]. However, mutation of the analogous residues in LAR did not impair the ability of gamma secretase to generate an ICD so they may not be critical for a PTPsigma-ICD either [26]. If this detected fragment is in fact an ICD, it may be generated through a unique mechanism or from a site downstream of its transmembrane domain, resulting in a smaller size. Regardless, because PTPsigma exerts its inhibitory effect on autophagy in the presence of nutrients, it is likely that the CTF is the fragment relevant to PI(3)P suppression. The fact that the CTF is membrane-bound and turned over in the lysosome supports a model where PTPsigma is processed and internalized from the cell surface as part of the endocytic pathway. It would likely be during this trafficking that PTPsigma resides on PI(3)P-positive endocytic vesicles and likely suppresses VPS34 signaling to impede the maturation of both endosomal and autophagic vesicles.

To investigate the role of PTPsigma and autophagy in prostate cancer chemoresistance and metastasis, we developed an orthotopic *in vivo* model using luciferase-expressing C42B cells. These cells develop primary tumors at the site of injection (prostate epithelium) within 2 weeks of initiation, reach $100\,\mathrm{mm}^3$ by approximately 4 weeks, and all tumor-bearing mice require euthanasia by 9 weeks. Importantly, we have detected micrometastases in all tumor-bearing mice, consistent with the known metastatic potential of C4-2B cells and confirming this model is a robust tool to study metastasis. We have engineered luciferase-expressing C42B cells to express or lack PTPsigma. Specifically, we have exogenously introduced, by viral infection, wildtype or a series of catalytically inactive PTPsigma mutants. As a complement, we have stably expressed shRNAs that effectively reduce PTPsigma protein levels. We found that PTPsigma shRNA-expressing cells gave rise to more robust primary tumors in this orthotopic C4-2B-luc model, compared to control shRNA-expressing cells. In addition, lung micrometastases were more abundant in animals injected with cells expressing one of two PTPsigma shRNAs compared to those injected with control cells. Future work will determine whether this increased metastasis is attributed to specific knockdown of PTPsigma. Importantly, tumors driven from PTPsigma shRNA-expressing cells appear to contain increased punctate LC3 staining (as determined by IHC). We will continue to use these cell lines and the established model of tumor growth and metastasis to further impact the understanding of autophagy and chemoresistance in prostate cancer.

REFERENCES:

1. Ittmann, M.M., *Chromosome 10 alterations in prostate adenocarcinoma (review).* Oncol Rep, 1998. **5**(6): p. 1329-35.
2. Li, J., et al., *PTEN, a putative protein tyrosine phosphatase gene mutated in human brain, breast, and prostate cancer.* Science, 1997. **275**(5308): p. 1943-7.
3. Feldman, B.J. and D. Feldman, *The development of androgen-independent prostate cancer.* Nat Rev Cancer, 2001. **1**(1): p. 34-45.
4. Martin, K.R., et al., *Identification of small molecule inhibitors of PTPsigma through an integrative virtual and biochemical approach.* PLoS One, 2012. **7**(11): p. e50217.
5. MacKeigan, J.P., L.O. Murphy, and J. Blenis, *Sensitized RNAi screen of human kinases and phosphatases identifies new regulators of apoptosis and chemoresistance.* Nat Cell Biol, 2005. **7**(6): p. 591-600.
6. Martin, K.R., et al., *Identification of PTPsigma as an autophagic phosphatase.* J Cell Sci, 2011. **124**(Pt 5): p. 812-9.
7. Looyenga, B.D. and J.P. Mackeigan, *Characterization of Differential Protein Tethering at the Plasma Membrane in Response to Epidermal Growth Factor Signaling.* J Proteome Res, 2012.
8. He, Y., et al., *Identification of a lysosomal pathway that modulates glucocorticoid signaling and the inflammatory response.* Sci Signal, 2011. **4**(180): p. ra44.
9. Ouyang, D.Y., et al., *Autophagy is differentially induced in prostate cancer LNCaP, DU145 and PC-3 cells via distinct splicing profiles of ATG5.* Autophagy, 2013. **9**(1): p. 20-32.
10. Thalmann, G.N., et al., *Androgen-independent cancer progression and bone metastasis in the LNCaP model of human prostate cancer.* Cancer Res, 1994. **54**(10): p. 2577-81.

11. Bastide, C., et al., *A Nod Scid mouse model to study human prostate cancer.* Prostate Cancer Prostatic Dis, 2002. **5**(4): p. 311-5.
12. Fu, Z., et al., *Effects of raf kinase inhibitor protein expression on suppression of prostate cancer metastasis.* J Natl Cancer Inst, 2003. **95**(12): p. 878-89.
13. Pfitzenmaier, J., et al., *Characterization of C4-2 prostate cancer bone metastases and their response to castration.* J Bone Miner Res, 2003. **18**(10): p. 1882-8.
14. Aicher, B., et al., *Cellular redistribution of protein tyrosine phosphatases LAR and PTPsigma by inducible proteolytic processing.* J Cell Biol, 1997. **138**(3): p. 681-96.
15. Ruhe, J.E., et al., *EGFR signaling leads to downregulation of PTP-LAR via TACE-mediated proteolytic processing.* Cell Signal, 2006. **18**(9): p. 1515-27.
16. Havens, A.M., et al., *An in vivo mouse model for human prostate cancer metastasis.* Neoplasia, 2008. **10**(4): p. 371-80.
17. Elchebly, M., et al., *Neuroendocrine dysplasia in mice lacking protein tyrosine phosphatase sigma.* Nat Genet, 1999. **21**(3): p. 330-3.
18. Wallace, M.J., et al., *Neuronal defects and posterior pituitary hypoplasia in mice lacking the receptor tyrosine phosphatase PTPsigma.* Nat Genet, 1999. **21**(3): p. 334-8.
19. Uetani, N., et al., *Mammalian motoneuron axon targeting requires receptor protein tyrosine phosphatases sigma and delta.* J Neurosci, 2006. **26**(22): p. 5872-80.
20. Klionsky, D.J., *Autophagy: from phenomenology to molecular understanding in less than a decade.* Nat Rev Mol Cell Biol, 2007. **8**(11): p. 931-7.
21. Imami, K., et al., *Automated phosphoproteome analysis for cultured cancer cells by two-dimensional nanoLC-MS using a calcined titania/C18 biphasic column.* Anal Sci, 2008. **24**(1): p. 161-6.
22. Chang, Y.Y. and T.P. Neufeld, *An Atg1/Atg13 complex with multiple roles in TOR-mediated autophagy regulation.* Mol Biol Cell, 2009. **20**(7): p. 2004-14.
23. Ganley, I.G., et al., *ULK1.ATG13.FIP200 complex mediates mTOR signaling and is essential for autophagy.* J Biol Chem, 2009. **284**(18): p. 12297-305.
24. Hosokawa, N., et al., *Nutrient-dependent mTORC1 association with the ULK1-Atg13-FIP200 complex required for autophagy.* Mol Biol Cell, 2009. **20**(7): p. 1981-91.
25. Jung, C.H., et al., *ULK-Atg13-FIP200 complexes mediate mTOR signaling to the autophagy machinery.* Mol Biol Cell, 2009. **20**(7): p. 1992-2003.
26. Haapasalo, A., et al., *Presenilin/gamma-secretase-mediated cleavage regulates association of leukocyte-common antigen-related (LAR) receptor tyrosine phosphatase with beta-catenin.* J Biol Chem, 2007. **282**(12): p. 9063-72.
27. Gupta-Rossi, N., et al., *Monoubiquitination and endocytosis direct gamma-secretase cleavage of activated Notch receptor.* J Cell Biol, 2004. **166**(1): p. 73-83.

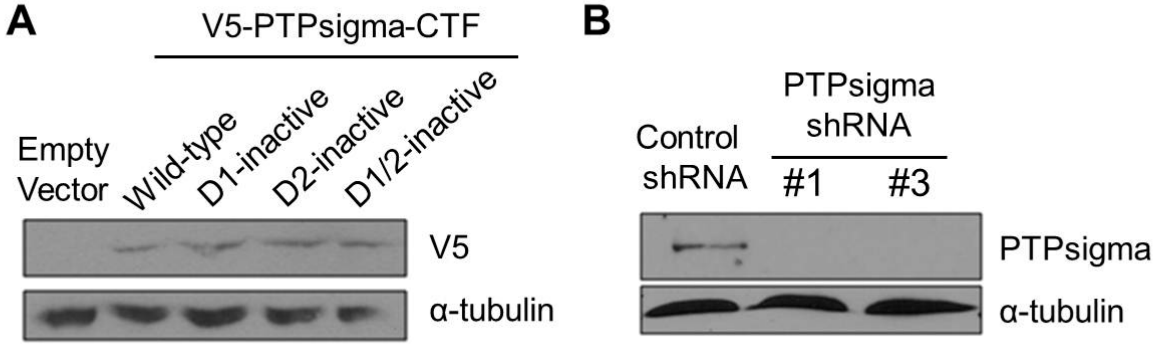

Figure 1. Generation of stable cell lines with modified expression of PTPsigma. (A) Luciferase-expressing C4-2B cells (C4-2B-luc) were infected with viral vectors encoding an empty vector, or the C-terminus of PTPsigma (containing residues including, and C-terminal, to the transmembrane domain; designated PTPsigma-CTF) fused to a V5-tag. Four V5-PTPsigma-CTF vectors were used including wild-type catalytic domains, an inactive D1 domain (C1589A), an inactive D2 domain (C1880A), or both inactive domains (residues numbers correspond to the longest PTPsigma isoform, NM_002850). Cells were lysed and immunoblotted using V5 antibodies. Tubulin was probed as a loading control. **(B)** C4-2B-luc cells were infected with viral vectors encoding control (non-targeting) shRNAs, or each of two unique shRNAs targeting PTPsigma (shRNA #1 and #3). Cells were lysed and immunoblotted with D1-targeted PTPsigma antibodies. Tubulin was probed as a loading control.

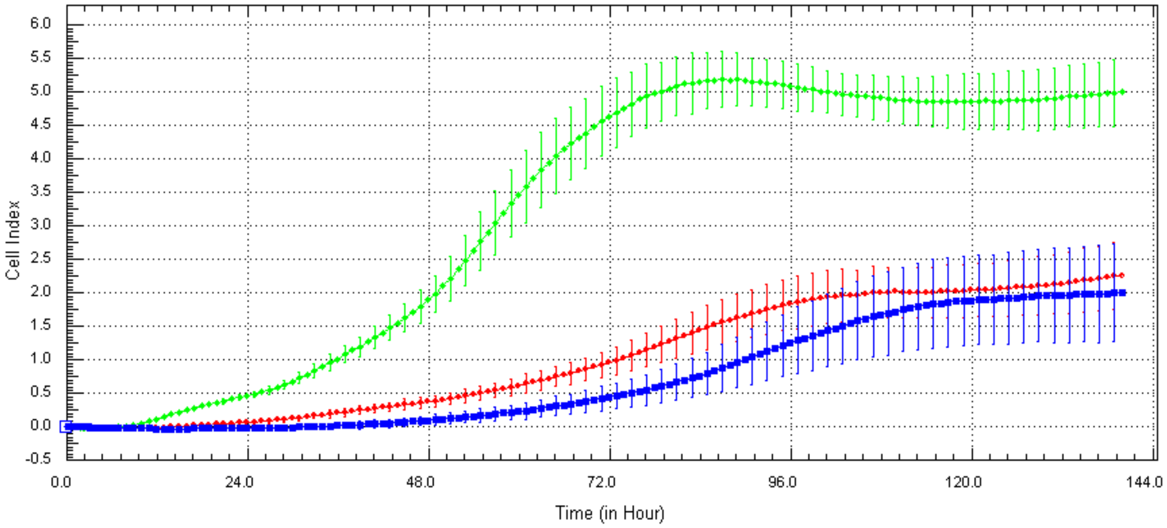

Figure 2. Loss of PTPsigma enhances proliferation in C4-2B-luc cells. Stable loss-of-function C4-2B-luc cells were plated in a 96-well format and allowed to grow until confluence. Using the xCELLigence system, real-time impedence was assessed and shown above as cell index with time (hours). Green: PTPsigma shRNA #3, red: PTPsigma shRNA #1, blue: control shRNA.

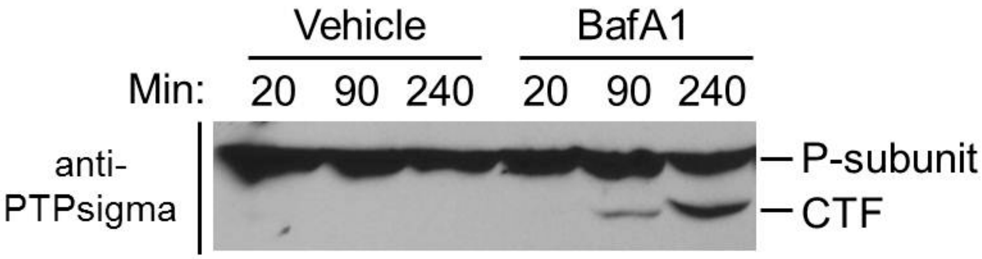

Figure 3. A PTPsigma C-terminal fragment (CTF) is generated and processed in a lysosomal pathway in C4-2B cells. C4-2B cells expressing full-length untagged PTPsigma (FL-PTPsigma) were treated with bafilomycin A1 (BafA1; a lysosomal inhibitor,) or a DMSO vehicle control for 0, 90, or 240 minutes, as indicated. Lysates were probed by western blot with D1-targeted PTPsigma antibodies. The plasma membrane resident P-subunit and cleaved C-terminal fragment (CTF) are identified according to molecular weight.

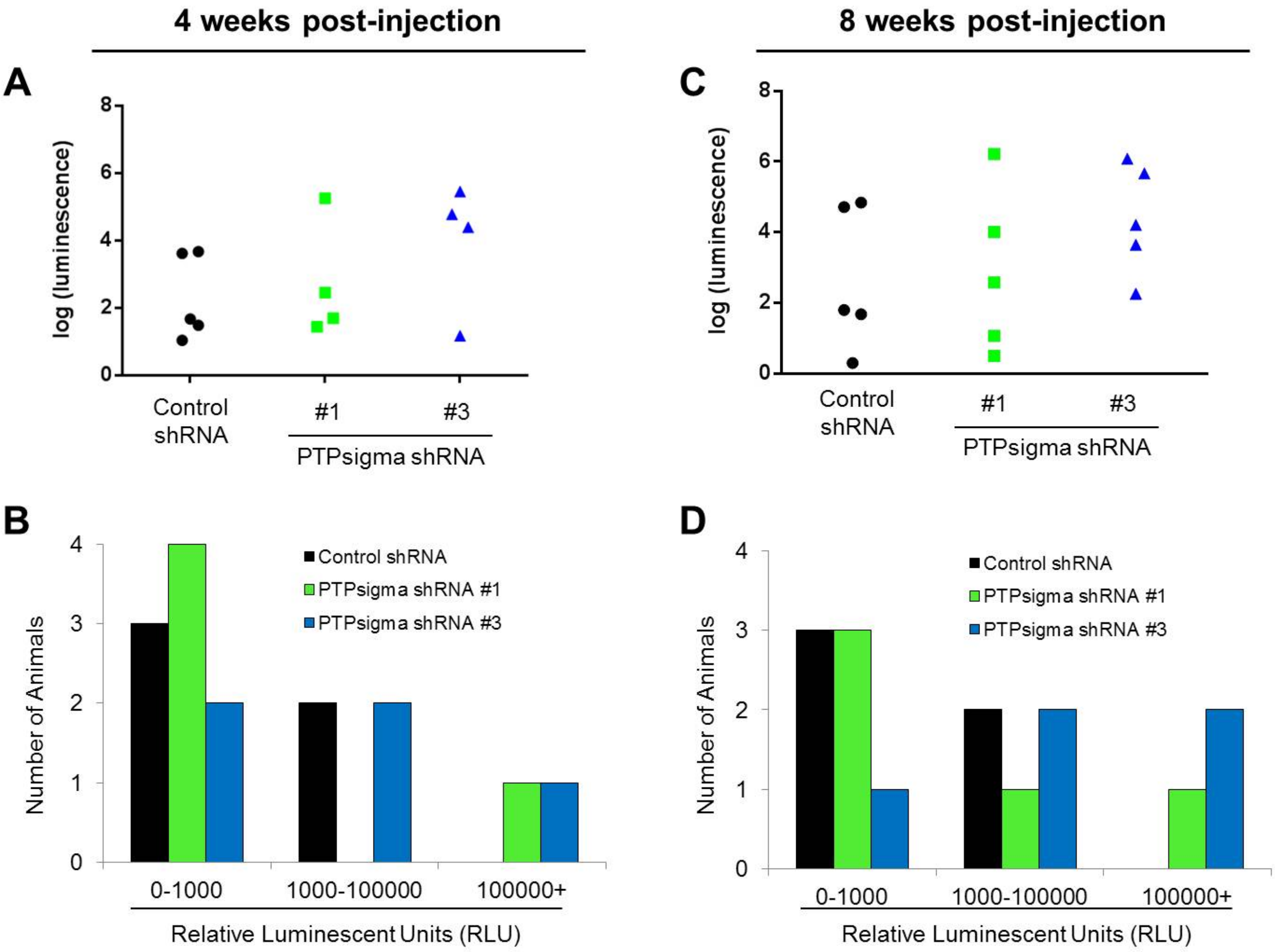

Figure 4. In vivo measurements of tumor growth in an orthotopic prostate cancer model. C4-2B-luc cells were injected into prostates of male athymic nude mice. Five mice per group were injected with the following cells: a) control shRNA, b) PTPsigma shRNA #1, c) PTPsigma shRNA #3, or d) PBS mock injection control. Tumors were monitored weekly by injecting mice with luciferin before bioluminescent imaging (BLI). The relative luminescence of each detectable tumor is indicated as a data point for the indicated mice (black: control shRNA; green: PTPsigma shRNA #1; blue: PTPsigma shRNA #3) 4 weeks (A) or 8 weeks (C) following cell injection. Note the log scale. Tumors were binned according to relative luminescent units (RLU) or tumors as indicated. The number of animals harboring a tumor within each range is plotted as a bar for each group (black: control shRNA; green: PTPsigma shRNA #1; blue: PTPsigma shRNA #3) 4 weeks (B) or 8 weeks (D) following cell injection.

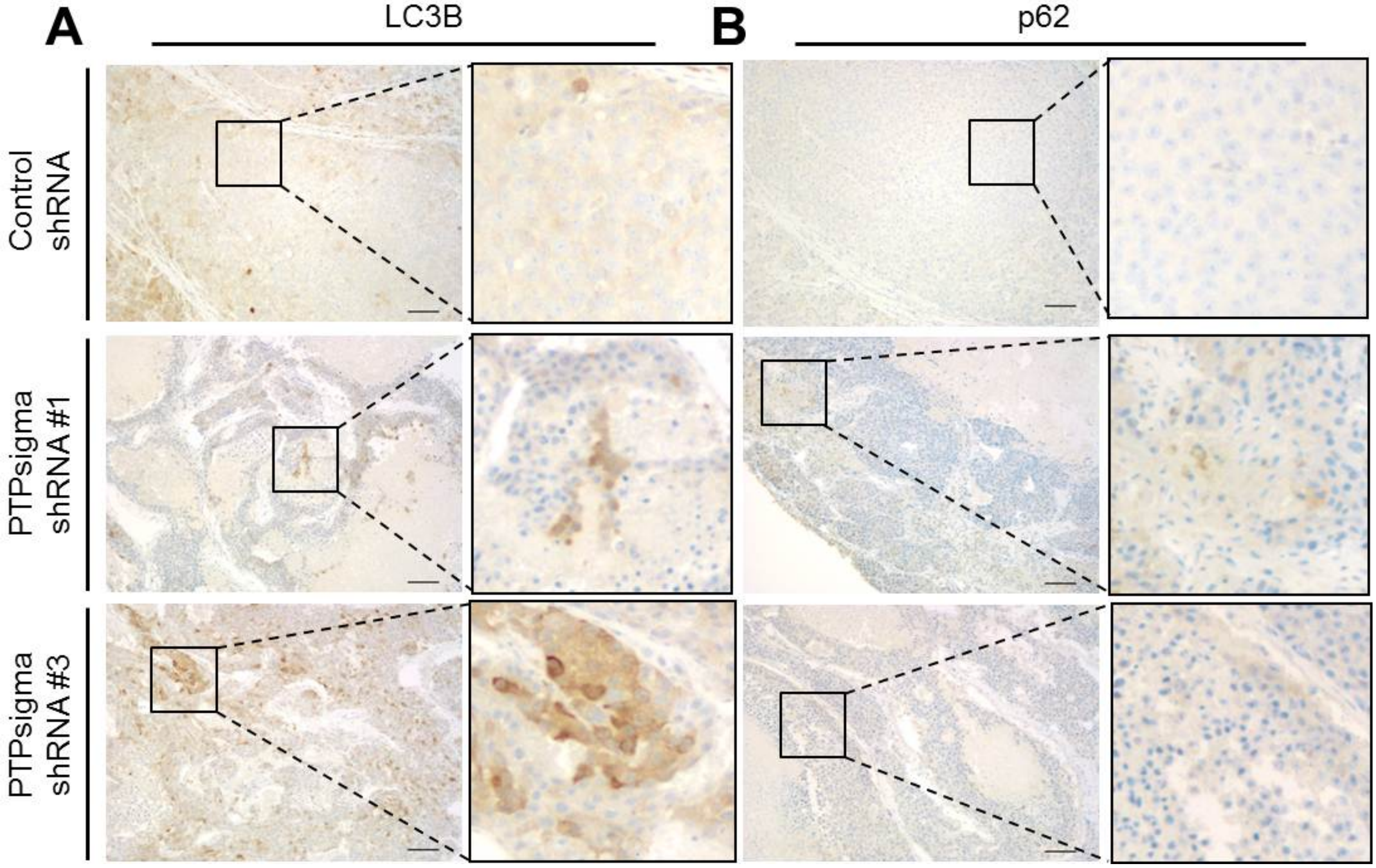

Figure 5. Immunohistochemistry (IHC) analysis of primary tumors from the orthotopic prostate cancer model. Luciferase-expressing C4-2B cells were injected into prostates of male athymic nude mice. Tumors grew until criteria for euthanasia were met (PTPsigma shRNA; 14 weeks), or the end of study (control shRNA; 18 weeks). Primary prostate tumors were harvested and analyzed by immunohistochemistry. Representative tumor specimens are shown from a mouse injected with C4-2B-luc cells expressing a control shRNA, PTPsigma shRNA #1, or PTPsigma shRNA #3, as indicated. Tumors were stained with antibodies to LC3B, a protein that becomes conjugated to autophagic membranes during autophagy (A) or p62, a protein that binds LC3 and recruits ubiquitinated cargoes into the autophagic vesicle (B). Images shown were captured at 10x. Scale bars are 100 µm. Panels at the right are magnifications of boxed regions.

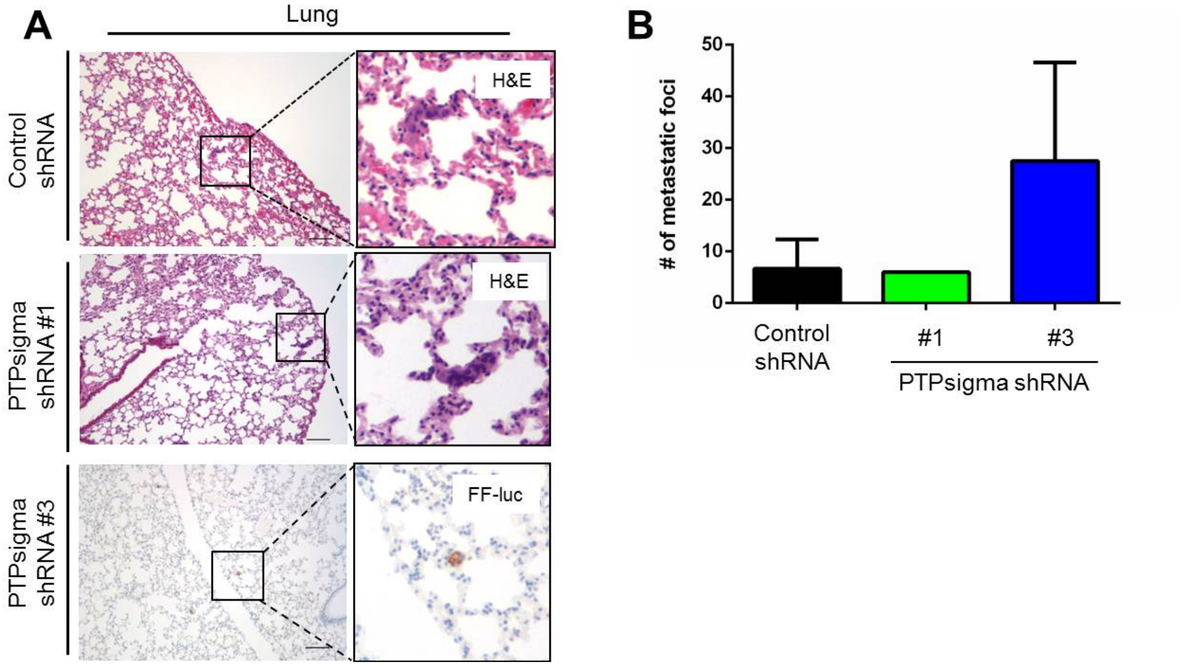

Figure 6. Analysis of lung micrometastases from the orthotopic prostate cancer model. Micrometastases were observed in lung tissue harvested from the animals described in *Figure 4* (control shRNA, PTPsigma shRNA #1, and PTPsigma shRNA #3). **(A)** Small clusters of cancer cells were observed by H&E staining and distinguished by their size and large nuclei. Staining with antibodies to firefly luciferase confirmed their C4-2B-luc identity (shown for PTPsigma shRNA #3, bottom panel). Panels at the right represent magnifications of boxed region. Scale bars are 100 µm. **(B)** Micrometastases were counted using firefly luciferase-stained tissue specimens. Total lung area was counted for experimental animals within each group (control shRNA: n=3, PTPsigma shRNA #1: n=1, PTPsigma shRNA #3: n=2). Mean number of metastases is plotted. Bar represents standard deviation.

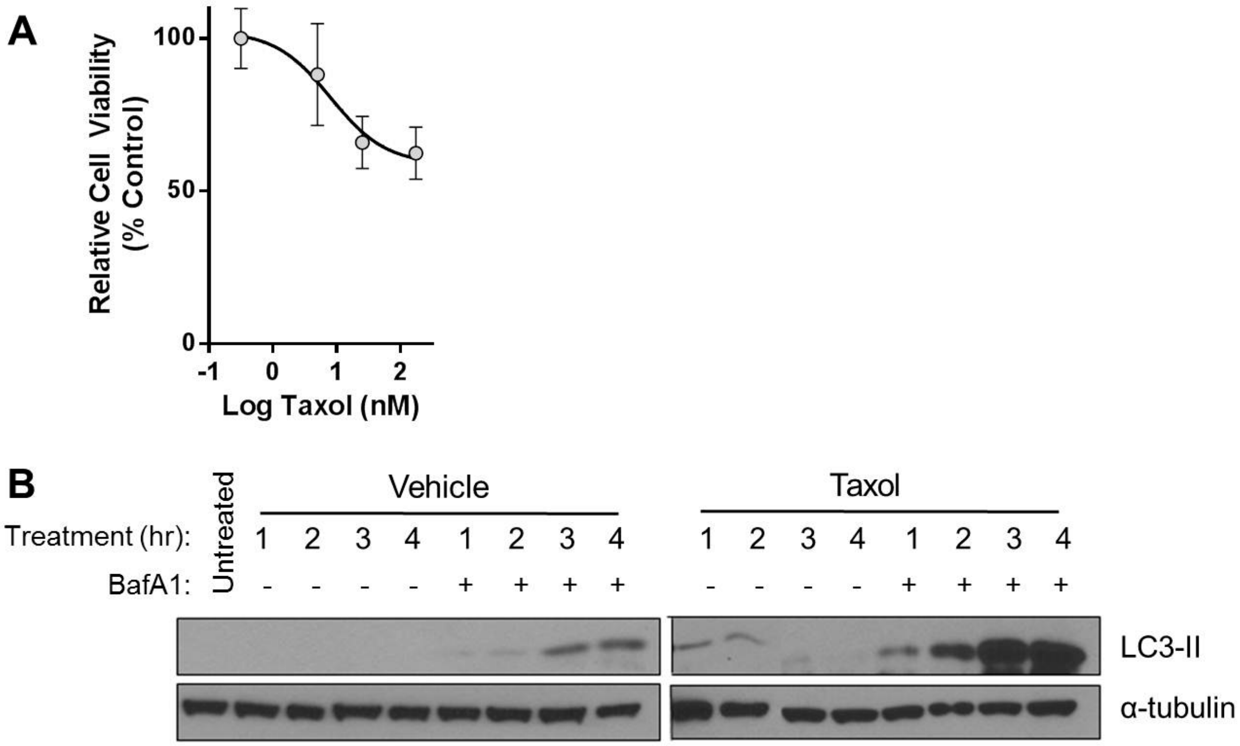

Figure 7. Cellular consequences of taxol treatment. **(A)** C4-2B-luc cells were treated with a range of paclitaxel (Taxol) doses to determine level of sensitivity *in vitro*. Cell viability was assessed using CyQuant and plotted as relative cell number. Bars represent standard deviation. **(B)** C4-2B-luc cells were treated with 500 nM Taxol or a DMSO vehicle control for 1, 2, 3, or 4 hours, as indicated. In addition, media was supplemented with (+) or without (-) bafilomycin A1 (BafA1) to inhibit lysosomal turnover of LC3-II. Lysates were collected and probed by immunoblotting with LC3B-targeted antibodies to detect LC3-II. Tubulin was probed as a loading control. An untreated cell lysate was also included.

Identification of PTPs as an autophagic phosphatase

Katie R. Martin[1,2], Yong Xu[3], Brendan D. Looyenga[1], Ryan J. Davis[1], Chia-Lun Wu[4], Michel L. Tremblay[4], H. Eric Xu[3] and Jeffrey P. MacKeigan[1,*]

[1]Laboratory of Systems Biology, Van Andel Research Institute, Grand Rapids, MI 49503, USA
[2]Cell and Molecular Biology Graduate Program, Michigan State University, East Lansing, MI 48824-4320, USA
[3]Laboratory of Structural Sciences, Van Andel Research Institute, Grand Rapids, MI 49503, USA
[4]Goodman Cancer Centre, Department of Biochemistry, McGill University, Montreal, QC H3A 1A3, Canada
*Author for correspondence (jeff.mackeigan@vai.org)

Accepted 9 November 2010
Journal of Cell Science 124, 812-819

doi:10.1242/jcs.080341

Summary

Macroautophagy is a dynamic process whereby portions of the cytosol are encapsulated in double-membrane vesicles and delivered to the lysosome for degradation. Phosphatidylinositol-3-phosphate (PtdIns3*P*) is concentrated on autophagic vesicles and recruits effector proteins that are crucial for this process. The production of PtdIns3*P* by the class III phosphatidylinositol 3-kinase Vps34, has been well established; however, protein phosphatases that antagonize this early step in autophagy remain to be identified. To identify such enzymes, we screened human phosphatase genes by RNA interference and found that loss of PTPs, a dual-domain protein tyrosine phosphatase (PTP), increases levels of cellular PtdIns3*P*. The abundant PtdIns3*P*-positive vesicles conferred by loss of PTPs strikingly phenocopied those observed in cells starved of amino acids. Accordingly, we discovered that loss of PTPs hyperactivates both constitutive and induced autophagy. Finally, we found that PTPs localizes to PtdIns3*P*-positive membranes in cells, and this vesicular localization is enhanced during autophagy. We therefore describe a novel role for PTPs and provide insight into the regulation of autophagy. Mechanistic knowledge of this process is crucial for understanding and targeting therapies for several human diseases, including cancer and Alzheimer's disease, in which abnormal autophagy might be pathological.

Key words: FYVE, PTPs, PtdIns3*P*, RNAi, Autophagy, Phosphatase

---

Introduction

In addition to the well-characterized role of phosphatidylinositol-3-phosphate (PtdIns3*P*) in endocytosis, recent evidence has uncovered a crucial requirement for this lipid in macroautophagy (autophagy) (Axe et al., 2008; Obara et al., 2008a; Petiot et al., 2000). Autophagy occurs constitutively in nearly all cells to maintain homeostasis, but is further activated in response to stress as a survival or adaptive mechanism. During autophagy, a double-membrane phagophore forms and elongates around portions of cytosol, matures into an enclosed autophagosome, and delivers its contents to the lysosome for degradation (Klionsky, 2007). Basic biochemical components (i.e. amino acids and fatty acids) are exported from the lysosome and recycled by the cell, representing an energetically favorable alternative to de novo synthesis. In mammalian systems, the lipid kinase Vps34 forms a complex with several proteins, including Vps15, Beclin1, Atg14L, UVRAG and Bif1 to generate PtdIns3*P* on autophagic vesicles (Itakura et al., 2008; Zhong et al., 2009). PtdIns3*P* then recruits and tethers effector proteins, such as WIPI-1 (Atg18), which are required for proper membrane formation (Obara et al., 2008b; Proikas-Cezanne et al., 2004). The crucial requirement for PtdIns3*P* in this process is evidenced by the fact that autophagy is ablated in mutant Vps34 yeast strains and genetic Vps34 knockouts in *Drosophila* (Juhasz et al., 2008; Kihara et al., 2001). Despite knowledge of PtdIns3*P* production, the antagonistic phosphatases that regulate PtdIns3*P* during autophagy have remained elusive. Two myotubularin-related phosphatases, MTMR3 and MTMR14 (hJumpy), have recently been shown to dephosphorylate autophagic PtdIns3*P* in various contexts (Taguchi-Atarashi et al., 2010; Vergne et al., 2009). However, given the complexity of autophagy execution and the number of proteins in the autophagy network, we predict that additional protein phosphatases exist to regulate this process. Accordingly, we performed a high-content cell-based RNAi screen using a fluorescent PtdIns3*P* sensor to identify protein phosphatases that function upstream of PtdIns3*P* during autophagy.

Results

RNAi screening identifies PTPs as a modulator of PtdIns3*P* signaling

FYVE (Fab1, YOTB, Vac1 and EEA1) domains are cysteine-rich zinc-finger binding motifs that specifically recognize and bind PtdIns3*P* (Gaullier et al., 1998). An EGFP molecule fused to two tandem FYVE domains, termed EGFP–2xFYVE, serves as an effective cellular sensor of PtdIns3*P* (Gillooly et al., 2000). We analyzed U2OS cells stably expressing this construct by fluorescent microscopy and found that PtdIns3*P* predominantly localized to punctate, often perinuclear, vesicles when cultured in complete growth medium with full nutrients (Fig. 1A, supplementary material Movie 1). RNAi-mediated knockdown of Vps34 reduced cellular PtdIns3*P* content and resulted in a diffuse cytosolic distribution of EGFP–2xFYVE (Fig. 1B,F, supplementary material Fig. S1A). By contrast, a redistribution of EGFP–2xFYVE to small abundant autophagic vesicles occurred when cells were deprived of amino acids to potently induce autophagy (Fig. 1C, supplementary material Movie 2).

To identify genes that downregulate PtdIns3*P* signaling, we used several siRNAs targeting over 200 known and putative human phosphatases. The siRNAs were introduced into U2OS EGFP–2xFYVE cells, and the cells were subsequently monitored

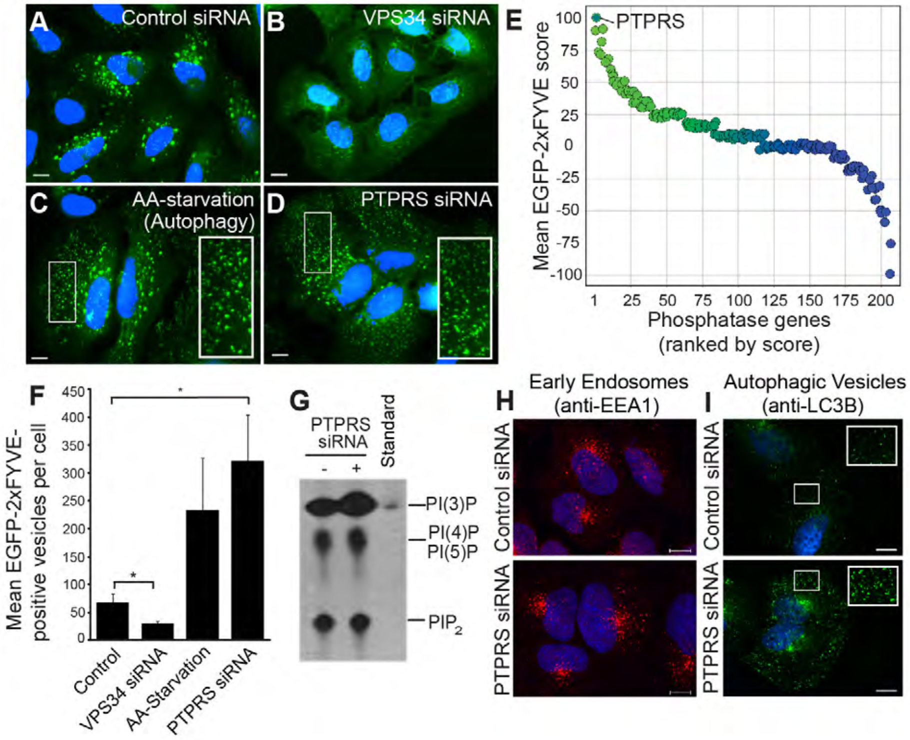

Fig. 1. A cell-based siRNA screen identifies PTPs as a modulator of PtdIns3*P*. (**A–D**) U2OS EGFP–2xFYVE cells transfected with control siRNA (A), *VSP34* siRNA (B), starved of amino acids for 3 hours (C), or transfected with *PTPRS* siRNA (D), were fixed and imaged at 60× magnification by fluorescent microscopy (green, PtdIns3*P*, EGFP–2xFYVE; blue, nuclei). Insets show 2× magnifications of small EGFP–2xFYVE vesicles. Scale bars: 10 µm. (**E**) Following knockdown of phosphatases, EGFP–2xFYVE-positive punctae were scored from –100 (decreased from control cells) to +100 (increased). Phosphatases are ranked and plotted by decreasing score (left to right) with genes whose loss increased EGFP–2xFYVE fluorescence highlighted in green and whose loss caused decreases highlighted in blue. *PTPRS* is identified. (**F**) Mean EGFP–2xFYVE-positive punctate were quantified from cells under the conditions indicated using image analysis software. Bars represent s.e.m.; **P*<0.05. (**G**) Phospholipids were radiolabeled in vivo, extracted, resolved by TLC, and visualized by autoradiography following transfection with control or *PTPRS* siRNA. A radiolabeled PtdIns3*P* standard was resolved adjacent to extracted lipids. (**H**,**I**) Endosomes were labeled by immunostaining with anti-EEA1 antibodies (H) and autophagic vesicles were labeled with anti-LC3B antibodies (I) following transfection with control or *PTPRS* siRNA (red, EEA1; green, LC3B; blue, nuclei). Insets show 2× magnifications of LC3-positive vesicles. Scale bars: 10 µm.

for PtdIns3*P* signaling. We identified several genes whose knockdown significantly increased the abundance of cellular EGFP–2xFYVE punctae (Fig. 1E, supplementary material Table S1). Most notably, PtdIns3*P* was substantially increased following knockdown of the myotubularin family member MTMR6 (supplementary material Fig. S1B,C), as well as the dual-domain protein tyrosine phosphatase PTPRS (PTPs) (Fig. 1D,E). Although reduced expression of MTMR6 was characterized by the appearance of enlarged perinuclear vesicles, the siRNAs targeting PTPs caused a dramatic accumulation of abundant smaller vesicles throughout the cytosol, which phenocopied results observed during amino acid starvation (Fig. 1C,D, supplementary material Movie 3). Quantification of PtdIns3*P*-positive vesicles revealed a 3.5-fold increase in abundance during starvation-induced autophagy and a nearly 5-fold increase caused by knockdown of PTPs alone (Fig. 1F). This phenotype was confirmed using four unique siRNA sequences targeting PTPs (supplementary material Fig. S1D-K).

To validate a physiological increase in PtdIns3*P* following knockdown of PTPs, phospholipids were radiolabeled with [^{32}P]orthophosphate in vivo, extracted, and resolved by thin-layer chromatography. Indeed, PtdIns3*P* levels were specifically elevated in the absence of PTPs, whereas other lipid species remained unchanged (Fig. 1G). To determine the identity of the PtdIns3*P*-positive vesicles formed by knockdown of PTPs, we immunostained cells with well-established markers of early endosomes [anti-EEA1 (early endosomal antigen 1)] and autophagic vesicles (AVs) [anti-LC3 (light chain 3)]. We found that knockdown of PTPs had no substantial effect on the presence of EEA1-positive endosomes (Fig. 1H, supplementary material Fig. S2A), but significantly increased the abundance of LC3-positive vesicles (Fig. 1I). From this, we hypothesized that PTPs functions during autophagy and focused our attention on this enzyme as a candidate autophagic phosphatase.

Loss of PTPs hyperactivates constitutive and induced autophagy

The striking resemblance of PtdIns3*P*-positive vesicles induced by PTPs knockdown to AVs formed during amino acid starvation led us to propose that autophagy is hyperactivated in the absence of PTPs, despite the presence of nutrients. To test this, autophagy was analyzed in U2OS cells by evaluating two ubiquitin-like proteins, Atg12 and LC3 (Atg8), which become conjugated to AVs during autophagy. Following phagophore nucleation, Atg12 covalently binds Atg5 and oligomerizes with Atg16L at the autophagic membrane (Klionsky, 2007). To measure vesicle abundance at this step, we immunostained cells for endogenous Atg12 and quantified Atg12-positive punctae. We found that

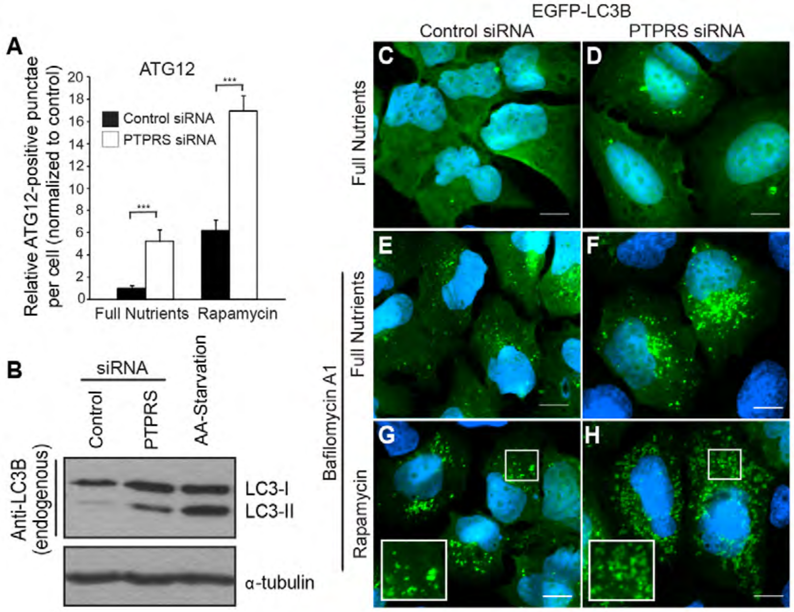

Fig. 2. Loss of PTPσ hyperactivates autophagy. (**A**) ATG12-positive punctae were quantified from 60× magnification images of cells transfected with control (black) or *PTPRS* siRNAs (white) and treated for 1 hour with normal growth medium (full nutrients) or 50 nM rapamycin. Values represent relative ATG12-positive punctae per cell following normalization to control cells cultured with full nutrients. Bars represent s.e.m.; ***$P<0.001$. (**B**) LC3-I and LC3-II were analyzed by western blot using whole cell lysates from cells transfected with control or *PTPRS* siRNA or starved of amino acids. α-tubulin was probed as a loading control. (**C**–**H**) EGFP–LC3-positive punctae were visualized in U2OS cells transfected with control (C,E,G) or *PTPRS* (D,F,H) siRNA following treatment for 2 hours with normal growth medium (full nutrients; C,D), 100 nM bafilomycin A1 (Baf-A1; E,F), or 50 nM rapamycin and 100 nM Baf-A1 (G,H) (green, EGFP-LC3; blue, nuclei). Insets are 2× magnifications of EGFP–LC3-positive AVs. Scale bars: 10 μm.

knockdown of PTPσ increased AV abundance three- or fivefold over the control when cells were cultured with rapamycin, a potent mTOR inhibitor and autophagy inducer, or full nutrients, respectively (Fig. 2A, supplementary material Fig. S2B).

The membrane-bound Atg5–Atg12–Atg16L complex permits lipidation of LC3, which is a classic marker for AVs (Hanada et al., 2007). LC3 is unique among the autophagy proteins in that a portion of it remains membrane bound and is degraded in the lysosome along with vesicle cargo. Therefore, lysosomal function can be inhibited [i.e. with bafilomycin A1 (Baf-A1) or chloroquine treatment] and LC3 accumulation used as a measure of autophagic flux (Tanida et al., 2005). We found that both knockdown of PTPσ and amino acid starvation increased the abundance of LC3-II, the AV-lipidated form of LC3, when lysates were probed with endogenous antibodies (Fig. 2B). Similarly, we observed an increased number of EGFP–LC3-positive punctae when PTPσ expression was reduced under normal growth conditions, and these structures accumulated substantially when cells were cultured with Baf-A1, indicating their functionality (Fig. 2C–F). Knockdown of PTPσ caused an even greater increase in EGFP–LC3 punctae above the control level when cells were treated with both Baf-A1 and rapamycin (Fig. 2G,H). Similar results were obtained when AVs were quantified from cells immunostained for endogenous LC3 (supplementary material Fig. S2C).

To confirm hyperactive autophagy in the absence of PTPσ independently of fluorescent markers, we detected AVs by transmission electron microscopy (TEM). AVs are hallmarked by unique double membranes and by the presence of engulfed cytosolic content: features that allow them to be easily detected by TEM. Although control cells contained very few AVs, chloroquine treatment increased their abundance, most of which appeared to be autolysosomal, as expected (Fig. 3A,B). Similarly, cells deprived of amino acids for 1 hour harbored elevated numbers of double-membrane AVs, as did cells transfected with siRNAs against PTPσ, but cultured in full nutrients (Fig. 3C,D). To establish this phenotype independently of RNAi, we examined autophagy during PTPσ loss using wild-type (*Ptprs*$^{+/+}$) and PTPσ knockout (*Ptprs*$^{-/-}$) murine embryonic fibroblasts (MEFs). We have previously generated *Ptprs*$^{-/-}$ mice by inserting a selectable neomycin resistance gene into the D1 phosphatase (catalytic) domain. From these mice, we generated MEFs that lack both *Ptprs* transcript and protein, as measured by northern blot and western blot, respectively (Elchebly et al., 1999). TEM analysis showed that both *Ptprs*$^{+/+}$ and *Ptprs*$^{-/-}$ primary MEFs contained a basal level of AVs; however, they were twice as abundant in *Ptprs*$^{-/-}$ MEFs (Fig. 3E-G). Collectively, these results demonstrate that loss of PTPσ, by RNAi and genetic deletion, increases both constitutive and induced autophagy.

PTPσ localizes to PtdIns3*P*-positive vesicles and rescues the siRNA phenotype

Given the robust PtdIns3*P* response elicited by knockdown of PTPσ, we hypothesized that PTPσ regulates autophagy by functioning at the level of PtdIns3*P*-positive vesicles. PTPσ is a bulky receptor-like PTP with an extracellular segment and two tandem cytosolic phosphatase domains (termed D1 and D2). Complex processing events have been reported for PTPσ and related enzymes, including ectodomain shedding and internalization from the cell surface (Aicher et al., 1997; Ruhe et al., 2006). To determine the localization of PTPσ phosphatase domains, untagged full-length protein (FL-PTPσ) was transiently expressed in U2OS EGFP–2xFYVE cells and detected by fluorescent microscopy using D1-targeted monoclonal antibodies. We found that in addition to its presence at the plasma membrane, PTPσ localized to the perinuclear region and to numerous intracellular -vesicle-like structures, many of which were positive for PtdIns3*P* (Fig. 4A). Strikingly, autophagy induction by amino acid starvation induced a redistribution of PTPσ to smaller vesicles, which were abundant throughout the cytosol and were almost entirely PtdIns3*P* positive (Fig. 4B,C). In support of the notion that this localization was autophagic, we discovered that PTPσ was also capable of localizing to mRFP–LC3-positive punctae in the context of both basal and induced autophagy (supplementary material Fig. S3B).

We further used exogenous PTPσ expression in an RNAi rescue experiment to demonstrate the specificity of phenotype induced by *PTPRS* siRNA. The naturally occurring isoform of PTPσ used in our studies lacks the fourth through seventh fibronectin domains

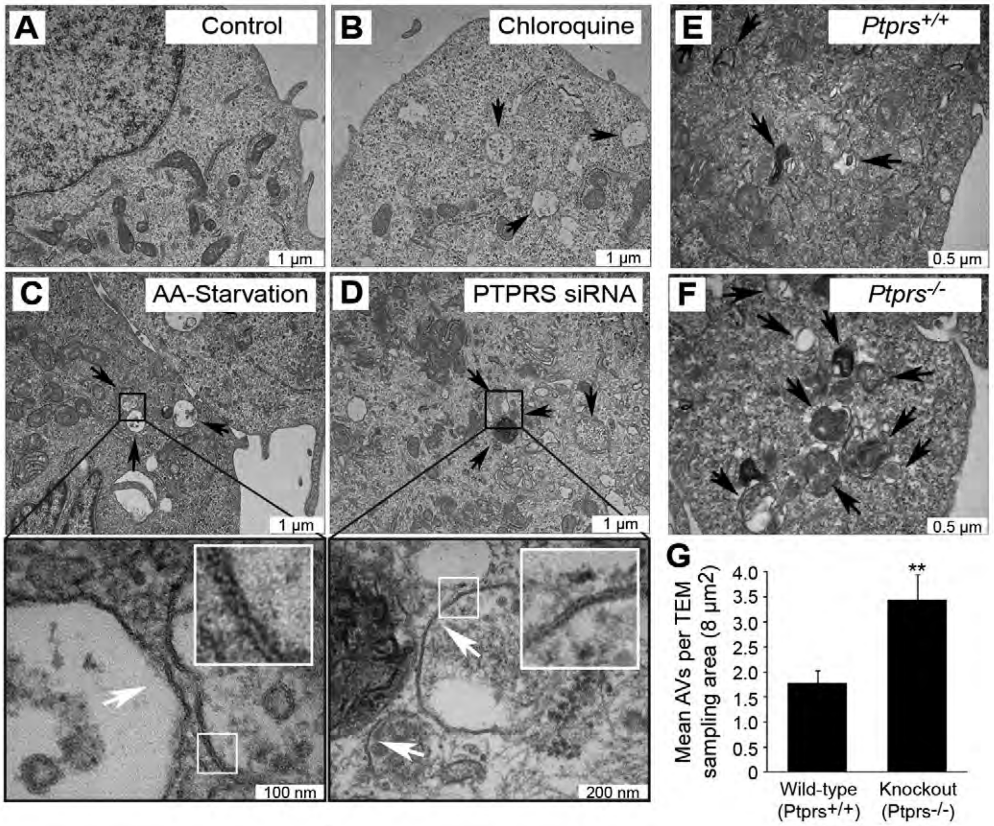

Fig. 3. Loss of PTPs increases autophagic vesicle abundance as measured by electron microscopy. (**A**–**D**) Few autophagic vesicles (AVs) were found by transmission electron microscopy (TEM) within control cells cultured in full nutrients (A), but were abundant in chloroquine-treated cells (B), amino acid (AA)-starved cells (C) and cells transfected with *PTPRS* siRNA (D). Black arrows indicate autophagic vesicles. White box insets are 3× magnifications. White arrows indicate double membranes. (**E**–**G**) Primary wild-type (*Ptprs*$^{+/+}$, E) and knockout (*Ptprs*$^{-/-}$, F) MEFs were analyzed by TEM and AVs quantified (G). AVs, defined as double-membrane structures containing cytosolic components, were counted from 8 μm^2 sampling regions per cell. Values represent mean AVs per sampling area. Bars represent s.e.m.; $^{**}P<0.01$.

(present in the longest isoform): a region encompassing the sequence targeted by a potent siRNA (siRNA-1; see supplementary material Fig. S1E,J,K) (Pulido et al., 1995). The accumulation of small, abundant, non-perinuclear PtdIns3*P*-positive vesicles induced by siRNA transfection was rescued by exogenous expression of PTPs, an effect that was dose dependent (Fig. 4D,E). This result suggests a target-specific effect of siRNA-mediated knockdown of PTPs and a role for this enzyme in PtdIns3*P* signaling.

To verify that the PTPs-positive punctate structures were in fact vesicles functioning in a lysosomal pathway, we monitored the localization of PTPs in Baf-A1-treated cells. Baf-A1 prevents maturing vesicles (e.g. endocytic and autophagic) from fusing with lysosomes and in turn, they accumulate in a perinuclear region. We found that PTPs-positive vesicular structures began to accumulate quickly (within 15 minutes) and densely populated the perinuclear region within several hours (Fig. 4F). This suggests that PTPs normally localizes to vesicles destined for the lysosome.

Finally, to determine whether PTPs functions upstream or downstream of PtdIns3*P* at the starvation-induced punctae, we analyzed its localization in cells depleted of the phospholipid. Autophagy was induced by amino acid starvation in cells treated with wortmannin, a potent and irreversible inhibitor of Vps34 and other phosphoinositide 3-kinase isoforms, or vehicle (DMSO). In vehicle-treated cells, starvation induced the formation of abundant PtdIns3*P*-positive vesicles, which also contained PTPs (Fig. 5A). Conversely, wortmannin treatment essentially ablated the formation of PtdIns3*P* during starvation; however, PTPs was still recruited to the abundant punctate structures (Fig. 5B). This finding suggests that the localization of PTPs to intracellular structures formed during autophagy occurs upstream, or independently, of PtdIns3*P*.

Discussion

Using a high-content cell-based RNAi screen, we have identified phosphatases whose knockdown elevates cellular PtdIns3*P*. Notably, RNAi-mediated knockdown of MTMR6 and several other phosphatases resulted in swollen and often perinuclear PtdIns3*P*-positive vesicles. Previous studies have shown similar phenotypes when endocytic PtdIns3*P* is elevated, for example, by constitutive activation of early endosomal Rab5, or knockdown of the phosphatidylinositol 5-kinase PIKfyve (Murray et al., 2002; Rutherford et al., 2006). Accordingly, the vesicles observed following knockdown of these phosphatases are probably endosomal, and these enzymes, including MTMR6, might function in endocytic signaling. Of note, knockdown of both PTPN11 (SHP2) and PTPN13 (PTPL1) resulted in increased numbers of EGFP–2xFYVE punctae (supplementary material Table S1). PTPN13, a phosphatase that is proposed to have both tumor suppressive and oncogenic functions, has been implicated in several signal transduction pathways. Specifically, PTPN13 was shown to inhibit PI3K/Akt signaling and thus, the PtdIns3*P* phenotype elicited by knockdown could potentially be explained by altered 3′-phosphoinositide metabolism (Abaan and Toretsky, 2008; Dromard et al., 2007). Mutations in SHP2 are associated with several human diseases, most notably Noonan syndrome, LEOPARD syndrome and juvenile myelomonocytic leukemia (Araki et al., 2004; Kontaridis et al., 2006; Mohi and Neel, 2007; Mohi et al., 2005). Its activity has been linked to numerous signaling pathways, often downstream of receptor tyrosine kinases, and the observed phenotype could be a consequence of disruption of any number of substrates (Chan et al., 2008).

Surprisingly, we did not identify MTMR3 or MTMR14 (hJumpy), the PtdIns3*P* phosphatases with reported roles in autophagy. The myotubularin phosphatases comprise a large, highly

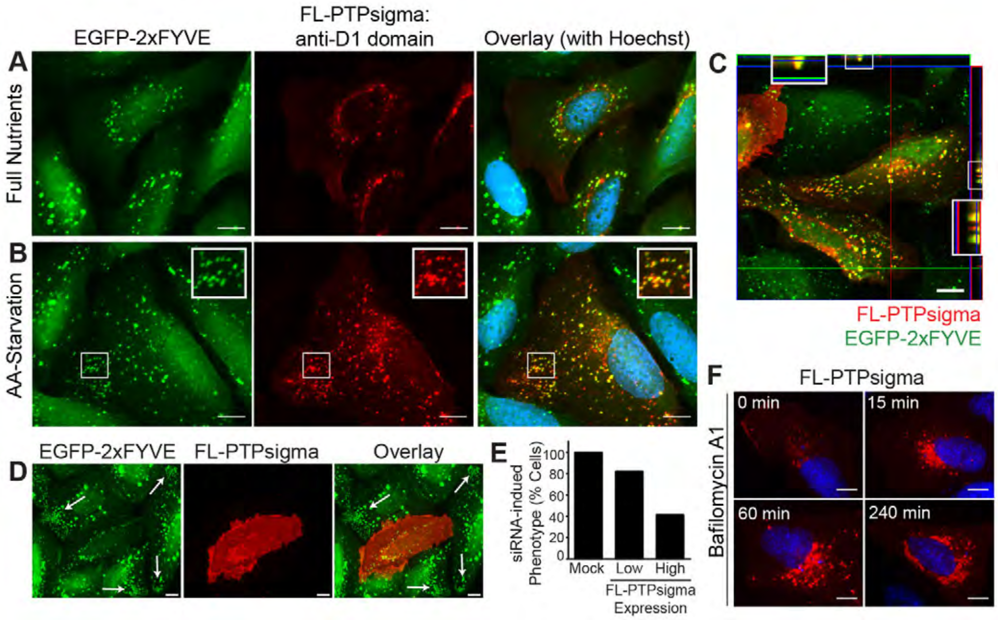

Fig. 4. Exogenous PTPσ localizes to PtdIns3*P* vesicles and rescues the siRNA phenotype. (**A**,**B**) FL-PTPσ was transiently expressed in U2OS EGFP–2xFYVE cells and PtdIns3*P* and PTPσ imaged by fluorescent microscopy following incubation for 2 hours with full nutrient medium (A) or amino acid starvation medium (B) [green, PtdIns3*P*; red, anti-PTPσ (D1-targeted antibodies); blue, nuclei]. Insets are 2× magnifications of boxed regions. Scale bars: 10 µm. (**C**) U2OS EGFP–2xFYVE cells transfected with FL-PTPσ and amino acid starved for 2 hours were imaged using D1-targeted PTPσ antibodies. A *Z*-stack of 0.25 µm increments was captured using sequential channel acquisition and confocal microscopy, with the third slice displayed and *Z*-stacks through the *X* and *Y* planes shown at the border. Insets are 2× magnifications of boxed regions. Scale bar: 10 µm (green, PtdIns3*P*, EGFP–2xFYVE; red, anti-PTPσ; yellow, colocalization). (**D**,**E**) U2OS EGFP–2xFYVE cells were transfected with *PTPRS* siRNA-1 for 48 hours, after which FL-PTPσ (which lacks the sequence targeted by siRNA-1) was introduced for an additional 24 hours. PtdIns3*P* and PTPσ were imaged as previously described. The presence of siRNA-induced phenotype (abundant, non-perinuclear EGFP–2xFYVE-positive vesicles; indicated by white arrows in D) was determined for cells expressing no, low or high levels of FL-PTPσ (E). Scale bars: 10 µm. (**F**) FL-PTPσ-positive vesicular structures accumulate when lysosomal fusion is inhibited. U2OS cells expressing FL-PTPσ for 24 hours were treated with 100 nM Baf-A1 in full nutrient medium for 0, 15, 60 or 240 minutes and FL-PTPσ imaged using D1-targeted PTPσ antibodies (red). Nuclei were stained with Hoechst 33342 (blue). Scale bars: 10 µm.

conserved family of enzymes whose members have been shown to function as heteromeric partners (Lorenzo et al., 2006). As one example, MTMR3 and MTMR4, both FYVE-domain containing phosphatases, have been demonstrated to interact with one another and inhibit PtdIns3*P* (Lorenzo et al., 2006). Accordingly, gene-by-gene loss-of-function analysis of this family might not reveal phenotypes if compensation within the family occurs. Furthermore, these enzymes may serve cell- or context-specific functions that are not revealed in this study.

The most striking result from this study was the presence of abundant PtdIns3*P*-positive vesicles following knockdown of PTPσ, which phenocopied that of an autophagic cell. We confirmed hyperactive autophagy in the absence of PTPσ through the use of several autophagy markers, as well as electron microscopy. Atg12- and LC3-positive autophagic vesicles were substantially more abundant in the absence of PTPσ when cells were cultured in full nutrients (constitutive AVs) or treated with rapamycin (induced AVs). These autophagic vesicles accumulated upon treatment with

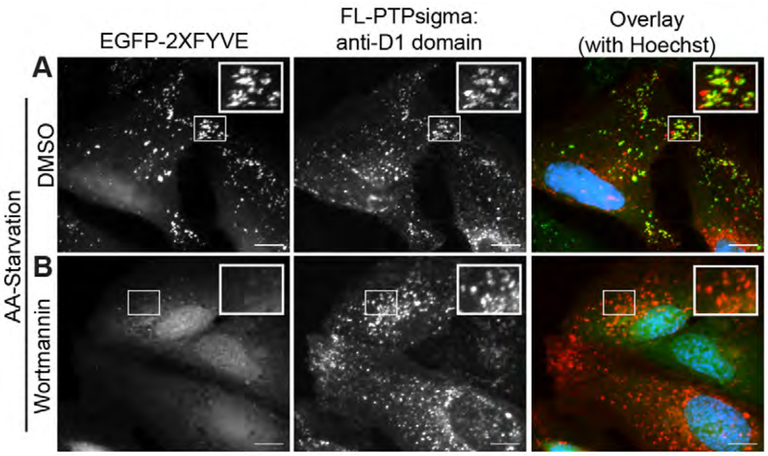

Fig. 5. Localization of PTPσ to vesicular structures does not require PtdIns3*P*. (**A**,**B**) U2OS cells expressing FL-PTPσ were treated with vehicle (DMSO; A) or 100 nM wortmannin (PI3K inhibitor; B) for 2 hours while cultured in amino acid starvation medium and PtdIns3*P* and PTPσ was imaged by fluorescent microscopy [green, PtdIns3*P*, EGFP–2xFYVE; red, anti-PTPσ (D1-targeted antibodies); blue, nuclei]. Insets are 2× magnifications of boxed regions. Scale bars: 10 µm.

the lysosomal inhibitors, Baf-A1 and chloroquine, demonstrating that they were functional and destined for lysosomal degradation. This phenotype suggests that PTPσ regulates an early step in autophagy induction, and its loss results in increased autophagic vesicle generation. This is consistent with the fact that PtdIns3*P* is generated on early phagophores and is required for proper autophagic vesicle formation. A role for PTPσ in autophagy induction and more specifically in PtdIns3*P* regulation, is supported by our findings that PTPσ localizes to PtdIns3*P*-positive vesicles that increase in number during autophagy.

It remains to be addressed how PTPσ is targeted to autophagic vesicles. PTPσ is expressed at the cell surface in a two-subunit complex comprised of a large ectodomain and a membrane-spanning intracellular domain. Accordingly, it is implicated in cell–cell and cell–ECM interactions, and it is a crucial regulator of axon homeostasis and neuronal development (Aicher et al., 1997; Elchebly et al., 1999; Uetani et al., 2006; Wallace et al., 1999). Relevant to our own work, ectodomain shedding and internalization of a membrane-bound C-terminal fragment has been demonstrated previously (Aicher et al., 1997). Through immunofluorescence analysis of PTPσ using D1-domain-specific antibodies, we place intracellular PTPσ on PtdIns3*P*-positive autophagic vesicles. Autophagosomes frequently fuse with endosomes during their maturation, forming hybrid organelles called amphisomes, establishing the possibility that PTPσ is internalized by endocytosis to arrive at autophagic vesicles (Klionsky, 2007). Furthermore, the close relative of PTPσ LAR (PTPRF), undergoes an additional proteolytic event whereby a soluble intracellular domain is formed and targeted inside the cell, similarly to the Notch receptor (Ruhe et al., 2006). PTPσ contains similar cleavage residues to LAR, making it therefore plausible that PTPσ is targeted from the plasma membrane to autophagic vesicles through a series of proteolytic events in response to autophagic stimuli. Thus, this phosphatase might serve several unique functions during various cellular conditions that are governed by its subcellular localization.

An important finding presented here is the recruitment of PTPσ to vesicular structures during amino acid starvation, which occurs even in the absence of PtdIns3*P* generation. This finding, together with the hyperactivation of autophagy elicited by knockdown of PTPσ (as measured by PtdIns3*P*, Atg12 and LC3), suggests that PTPσ regulates autophagy at an early step upstream of this lipid. In further support of this, we found that although almost all PTPσ-positive vesicles are also positive for PtdIns3*P* (EGFP–2xFYVE presence), fewer harbored LC3, a marker that is incorporated into AVs at later stages of maturation.

There are several potential mechanisms by which PTPσ might function to regulate autophagy. First, it is possible that PTPσ directly dephosphorylates PtdIns3*P* following recruitment to AVs. We tested the activity of recombinant PTPσ in vitro, and although we could not detect PtdIns3*P* phosphatase activity, it cannot be entirely excluded that PtdIns3*P* does not serve as a direct substrate in vivo (supplementary material Fig. S4). It is also possible that PTPσ uses its robust protein phosphatase activity to regulate the function of a PtdIns3*P*-modifying enzyme, such as a PtdIns3*P* phosphatase or a phosphoinositide 4- or 5-kinase. Alternatively, PTPσ could control the activity of Vps34, which contains at least one phosphotyrosine site, or another component within the larger Vps34 complex (Imami et al., 2008). Finally, PTPσ might contribute to the regulation of autophagy at the earliest initiation step, which is executed by a complex of autophagy proteins, namely ULK1 (Atg1) and Atg13. The functional formation of this complex, which permits the generation of the PtdIns3*P*-positive phagophore, was recently found to be tightly regulated by phosphorylation events (Chang and Neufeld, 2009; Ganley et al., 2009; Hosokawa et al., 2009; Jung et al., 2009). The aim of future work will be to determine the precise mechanism by which PTPσ functions to regulate autophagy.

Materials and Methods

siRNA screen and validation

U2OS EGFP–2xFYVE cells were seeded on 96-well plates (2000 cells per well) in McCoy's 5A medium (Invitrogen, Carlsbad, CA) supplemented with 10% fetal bovine serum (FBS, Invitrogen) at 37°C for 24 hours. Four siRNA molecules per phosphatase gene (phosphatase siRNA library version 2.0, Qiagen, Valencia, CA) were transfected per well at a final concentration of 25 nM using 0.2 µl HiPerfect transfection reagent (Qiagen) per well. After 48 hours, cells were fixed with 3.7% formaldehyde and nuclei were stained with Hoechst 33342 (Invitrogen). Cells were visualized at 40× magnification on a Zeiss LSM 510 Meta confocal microscope (Oberkochen, Germany) and EGFP–2xFYVE fluorescence was compared with that of control siRNA transfected cells within each plate. Triplicate wells from each gene were qualitatively scored by two independent scorers on a scale from –100 (decreased EGFP–2xFYVE signal and distribution) to +100 (increased) and mean scores were determined. Twenty-seven phosphatase genes whose knockdown increased EGFP–2xFYVE fluorescence in the primary screen were used in a secondary screen, where four siRNAs were individually transfected to eliminate off-target hits. The primary score was multiplied by a binned secondary screen score (score of 1.0 for 3/4 or 4/4 siRNAs yielding a phenotype; 0.75 for 2/4 siRNAs; and 0 for 0/4 or 1/4 siRNAs). Quantitative real-time PCR (qRT-PCR) assays with SYBR green dye (Roche, Basel, Switzerland) and gene-specific primers confirmed that siRNAs effectively reduced mRNA expression of target genes. For imaging, cells were cultured on number 1.5 coverglass, transfections repeated as above, cells fixed, nuclei stained, and coverglass inverted into microslides with mounting gel. A control siRNA transfected well was cultured for 3 hours in amino acid starvation medium [Dulbecco's phosphate-buffered saline (DPBS) with 10% FBS and 1 g/l D-glucose]. Cells were imaged using a 60× oil objective on a Nikon TE300 fluorescent microscope (Tokyo, Japan). EGFP–2xFYVE-positive vesicles were quantified using image analysis software.

Phospholipid labeling, extraction and thin-layer chromatography

U2OS cells were seeded in McCoy's 5A with 10% FBS at 200,000 cells per well of six-well tissue culture plates. After 24 hours, control or *PTPRS* siRNAs were transfected at a final concentration of 25 nM using 2 µl HiPerfect transfection reagent per ml medium. Control siRNA was All-star Negative Control (Qiagen) and *PTPRS* siRNAs were two unique sequences (SI02759288, SI03056284, Qiagen). After 48 hours of transfection, the medium was replaced with phosphate-free DMEM (Invitrogen) supplemented with 10% phosphate-free FBS for 30 minutes. $[^{32}P]O_4$ (0.25 mCi) was added per ml of medium for an additional 2 hours (Perkin Elmer, Waltham, MA). Radiolabeling was quenched with ice-cold TCA (10% final concentration) and cells incubated on ice for 1 hour. Cells were scraped, pelleted and lipids extracted via an acidified Bligh and Dyer method (Bird, 1994). Lipids were lyophilized, resuspended in chloroform:methanol (1:1), spotted on 20 cm × 20 cm silica gel TLC plates (Whatman, Maidstone, UK), and resolved in a chamber using boric acid buffer (Walsh et al., 1991). A PtdIns3*P* standard was generated by incubating synthetic phosphatidylinositol (diC16 PtdIns; Echelon, Salt Lake City, UT) with immunoprecipitated PI3K (using anti-p85, Cell Signaling, Danvers, MA) and $[^{32}P]$ATP (Perkin Elmer). The TLC plate was exposed to film for 20 hours at –80°C and developed.

Fluorescent microscopy and western blot analyses of autophagy markers

U2OS cells were seeded at a density of 35,000 cells per well in McCoy's 5A medium with 10% FBS on number 1.5 coverglasses in 24-well tissue culture plates (for fluorescent imaging) or 150,000 cells per well on six-well dishes (for western blot). After 24 hours, cells were transfected with control or *PTPRS* siRNAs for 48 hours, as described above. Following, cells were treated for 1–2 hours in amino acid starvation medium or with 50 nM rapamycin (Calbiochem, San Diego, CA), 25 µM chloroquine (Sigma, St Louis, MO), 100 nM Baf-A1 (A.G. Scientific, San Diego, CA) or normal growth medium (full nutrients; McCoy's 5A with 10% FBS), as indicated. For western blots, cells were lysed [in 10 mM KPO_4, 1 mM EDTA, 10 mM $MgCl_2$, 5 mM EGTA, 50 mM bis-glycerophosphate, 0.5% NP40, 0.1% Brij35, 0.1% sodium deoxycholate, 1 mM $NaVO_4$, 5 mM NaF, 2 mM DTT, and complete protease inhibitors (Sigma)] and 20 µg of total protein was resolved by SDS-PAGE. Proteins were transferred to PVDF membranes and probed with primary antibodies (LC3B, Cell Signaling Technologies; anti-α-tubulin, Sigma) for 16 hours at 4°C followed by secondary antibodies (HRP-linked rabbit or mouse IgG, GE, Piscataway, NJ) for 1 hour at room temperature. Proteins were detected by enhanced chemiluminescence. For EGFP–LC3 imaging, U2OS cells stably expressing ptfLC3 (Addgene plasmid 21074) (Kimura et al., 2007) were fixed with 3.7% formaldehyde and nuclei stained with Hoechst 33342 (2 µg/ml). Coverglasses were inverted onto microslides using mounting gel and cells imaged using a 100 × oil-immersion objective on a Nikon Eclipse Ti fluorescence microscope. For immunofluorescence, cells were fixed with 3.7% formaldehyde, permeabilized with 0.2% Triton-X 100, and blocked with 3% bovine serum albumin (BSA) in PBS. Antibodies (LC3B, ATG12, EEA1; Cell Signaling Technologies) were added for 16 hours at 4°C followed by Alexa-Fluor-488-conjugated anti-rabbit IgG (Invitrogen) for 1 hour at room temperature. Nuclei were counterstained with Hoechst 33342, cover glasses were inverted onto microslides using mounting gel and cells were imaged using 60× or 100× oil-immersion objectives on a Nikon TE300 fluorescence microscope (LC3, ATG12) or a 63 × water-immersion objective on a Zeiss LSM510 Meta confocal microscope (EEA1). For quantification, punctae were counted using image analysis software after establishing an intensity threshold.

Transmission electron microscopy

U2OS cells in 10 cm dishes were transfected with control or PTPRS siRNAs for 48 hours as described above. Cells were briefly trypsinized, pelleted, rinsed and resuspended in 2% glutaraldehyde fixative (Sigma). Cell pellets were embedded in 2% agarose, postfixed in osmium tetroxide, and dehydrated with an acetone series. Samples were infiltrated and embedded in Poly/Bed 812 resin and polymerized at 60°C for 24 hours. Ultrathin sections (70 nm) were generated with a Power Tome XL (Boeckeler Instruments, Tucson, Arizona) and placed on copper grids. Cells were examined using a JEOL 100C× Transmission Electron Microscope at 100 kV (Tokyo, Japan). Autophagic structures were quantified from images encompassing approximately 8.5 μm^2 of cell area each. Electron microscopy services were performed by the Michigan State University Center for Advanced Microscopy (East Lansing, MI).

Exogenous PTPs expression and immunofluorescence

U2OS EGFP–2xFYVE cells were seeded at a density of 20,000 cells per well in McCoy's 5A medium with 10% FBS on number 1.5 cover glasses in 24-well tissue culture dishes. Full-length *PTPRS* cDNA (BC104812) was inserted into pRK7 by *Eco*RI digestion and ligation to yield FL-PTPs-pRK7 (FL-PTPs). DNA was transfected at 0.15 µg per well using 0.45 µl FuGeneHD transfection reagent (Roche, Mannheim, Germany) in 50 µl Optimem and 450 µl McCoy's 5A with 10% FBS for 24 hours. For 2 hours, cells were cultured with full nutrient medium or starved of amino acids (Fig. 4A-C), or amino acid starved while treated with DMSO or 100 nM wortmannin (Sigma) (Fig. 5, supplementary material Fig. S3). Alternatively, cells were treated with Baf-A1 (100 nM in full nutrient medium) for 0, 15, 60 or 240 minutes (Fig. 4E). Cells were then fixed with 3.7% formaldehyde, permeabilized with 0.2% Triton X-100, blocked in 3% BSA, and stained with antibodies targeting the D1 domain of PTPs for 2 hours at room temperature. AF-546-conjugated anti-mouse-IgG (Invitrogen) were incubated for an additional hour at room temperature and nuclei were stained with Hoechst 33342. Cells were imaged using oil-immersion objectives at 60 × on a Nikon TE3000 or 100 × on an Eclipse Ti fluorescent microscope. For Fig. 4C, cells were treated as above and imaged using a 63× water-immersion objective on a Zeiss LSM510 Meta microscope. Red (AF-546, FL-PTPs) and green (EGFP–2xFYVE, PtdIns3*P*) channels were captured with confocality through the *Z*-plane using 16 increments of 0.25 µm. Stacks through the indicated *X* and *Y* planes are shown at the border of an image of the third *Z*-plane. For supplementary material Fig. S3B, U2OS cells stably expressing mRFP–LC3 (Addgene plasmid 21075) (Kimura et al., 2007) were seeded, transfected, treated (full nutrient or amino acid starvation media for 2 hours), and stained as above. Images were captured at 100 × using an oil-immersion objective on an Eclipse Ti fluorescent microscope.

Rescue of siRNA phenotype

U2OS EGFP–2xFYVE cells were seeded on number 1.5 cover glasses in 24-well dishes at 20,000 cells per well in McCoy's 5A medium with 10% FBS. 24 hours later, *PTPRS* siRNA-1 (CACGGCATCAGGCGTGCACAA; Qiagen) was transfected at a concentration of 25 nM using 1 µl oligofectamine per well per 500 µl McCoy's with 10% FBS (Invitrogen). FL-PTPs-pRK7 plasmid DNA was transfected 24 hours later at a concentration of 0.15 µg DNA per well using 0.45 µl FuGeneHD transfection reagent in 50 µl Optimem and 450 µl McCoy's 5A with 10% FBS for an additional 24 hours. Cells were fixed and immunostained as described above. Cells were imaged using a 60 × oil objective on a Nikon TE300 fluorescent microscope for EGFP–2xFYVE phenotype (green) and FL-PTPs-pRK7 expression (red). FL-PTPs-pRK7 expression levels were categorized as high or low. The presence or absence of a robust PTPRS siRNA-induced EGFP–2xFYVE phenotype was determined (phenotype defined as the presence of small, abundant, non-perinuclear EGFP–2xFYVE-positive vesicles; indicated with white arrows in Fig. 4D) for 30–40 cells each of low and high FL-PTPs-expressing cells, as well as cells transfected with *PTPRS* siRNA-1 but not FL-PTPs-pRK7.

In vitro phosphatase assays

GST-tagged recombinant PTPs containing all residues C-terminal to the transmembrane domain (BC104812 cDNA; aa 883–1501) was generated in pGEXKG (Guan and Dixon, 1991). GST-tagged full-length MTMR6 (NM_004685.2) was generated in pGEXKG and GST-tagged recombinant PTP1B was purchased (Upstate, Billerica, MA). Proteins were purified from BL21 *Escherichia coli* after isopropyl b-D-1-thiogalactopyranoside (IPTG) induction and used in phosphatase assays. For PtdIns3*P* phosphatase reactions, 1 µg protein was suspended in 50 µl assay buffer (50 mM sodium acetate, 25 mM Tris-HCl, 10 mM DTT, pH 6.5) with 0, 25, 50 or 200 µM diC8-PtdIns3*P* and reactions carried out at 37°C for 25 minutes. For Tyr-*P* phosphatase assays, reactions were carried out as above using 0, 10, 25 or 100 µM Tyr-*P* peptide (TSTEPQpYQPGENL; Upstate) at 37°C for 15 minutes. Released phosphates were detected with malachite green (Upstate) and absorbance measured at 650 nm. Background levels from enzyme-only and substrate-only (Tyr-*P* or PtdIns3*P*) reactions were subtracted and absorbance converted to picomoles free phosphate released per minute using a standard curve.

We thank the Van Andel Institute Systems Biology lab for advice, analysis, and reagents. This work was supported by the Department of Defense Prostate Cancer Research Program of the Office of Congressionally Directed Medical Research Programs PC081089 to J.P.M. J.P.M. is also supported by Award Number R01CA138651 from the National Cancer Institute. Deposited in PMC for release after 12 months.

Supplementary material available online at
http://jcs.biologists.org/cgi/content/full/124/5/812/DC1

References

Abaan, O. D. and Toretsky, J. A. (2008). PTPL1: a large phosphatase with a split personality. *Cancer Metastasis Rev.* **27**, 205-214.

Aicher, B., Lerch, M. M., Muller, T., Schilling, J. and Ullrich, A. (1997). Cellular redistribution of protein tyrosine phosphatases LAR and PTPsigma by inducible proteolytic processing. *J. Cell Biol.* **138**, 681-696.

Araki, T., Mohi, M. G., Ismat, F. A., Bronson, R. T., Williams, I. R., Kutok, J. L., Yang, W., Pao, L. I., Gilliland, D. G., Epstein, J. A. et al. (2004). Mouse model of Noonan syndrome reveals cell type- and gene dosage-dependent effects of Ptpn11 mutation. *Nat. Med.* **10**, 849-857.

Axe, E. L., Walker, S. A., Manifava, M., Chandra, P., Roderick, H. L., Habermann, A., Griffiths, G. and Ktistakis, N. T. (2008). Autophagosome formation from membrane compartments enriched in phosphatidylinositol 3-phosphate and dynamically connected to the endoplasmic reticulum. *J. Cell Biol.* **182**, 685-701.

Bird, I. M. (1994). Analysis of cellular phosphoinositides and phosphoinositols by extraction and simple analytical procedures. *Methods Mol. Biol.* **27**, 227-248.

Chan, G., Kalaitzidis, D. and Neel, B. G. (2008). The tyrosine phosphatase Shp2 (PTPN11) in cancer. *Cancer Metastasis Rev.* **27**, 179-192.

Chang, Y. Y. and Neufeld, T. P. (2009). An Atg1/Atg13 complex with multiple roles in TOR-mediated autophagy regulation. *Mol. Biol. Cell* **20**, 2004-2014.

Dromard, M., Bompard, G., Glondu-Lassis, M., Puech, C., Chalbos, D. and Freiss, G. (2007). The putative tumor suppressor gene PTPN13/PTPL1 induces apoptosis through insulin receptor substrate-1 dephosphorylation. *Cancer Res.* **67**, 6806-6813.

Elchebly, M., Wagner, J., Kennedy, T. E., Lanctot, C., Michaliszyn, E., Itie, A., Drouin, J. and Tremblay, M. L. (1999). Neuroendocrine dysplasia in mice lacking protein tyrosine phosphatase sigma. *Nat. Genet.* **21**, 330-333.

Ganley, I. G., Lam du, H., Wang, J., Ding, X., Chen, S. and Jiang, X. (2009). ULK1.ATG13.FIP200 complex mediates mTOR signaling and is essential for autophagy. *J. Biol. Chem.* **284**, 12297-12305.

Gaullier, J. M., Simonsen, A., D'Arrigo, A., Bremnes, B., Stenmark, H. and Aasland, R. (1998). FYVE fingers bind PtdIns(3)P. *Nature* **394**, 432-433.

Gillooly, D. J., Morrow, I. C., Lindsay, M., Gould, R., Bryant, N. J., Gaullier, J. M., Parton, R. G. and Stenmark, H. (2000). Localization of phosphatidylinositol 3-phosphate in yeast and mammalian cells. *EMBO J.* **19**, 4577-4588.

Guan, K. L. and Dixon, J. E. (1991). Eukaryotic proteins expressed in Escherichia coli: an improved thrombin cleavage and purification procedure of fusion proteins with glutathione S-transferase. *Anal. Biochem.* **192**, 262-267.

Hanada, T., Noda, N. N., Satomi, Y., Ichimura, Y., Fujioka, Y., Takao, T., Inagaki, F. and Ohsumi, Y. (2007). The Atg12-Atg5 conjugate has a novel E3-like activity for protein lipidation in autophagy. *J. Biol. Chem.* **282**, 37298-37302.

Hosokawa, N., Hara, T., Kaizuka, T., Kishi, C., Takamura, A., Miura, Y., Iemura, S., Natsume, T., Takehana, K., Yamada, N. et al. (2009). Nutrient-dependent mTORC1 association with the ULK1-Atg13-FIP200 complex required for autophagy. *Mol. Biol. Cell* **20**, 1981-1991.

Imami, K., Sugiyama, N., Kyono, Y., Tomita, M. and Ishihama, Y. (2008). Automated phosphoproteome analysis for cultured cancer cells by two-dimensional nanoLC-MS using a calcined titania/C18 biphasic column. *Anal. Sci.* **24**, 161-166.

Itakura, E., Kishi, C., Inoue, K. and Mizushima, N. (2008). Beclin 1 forms two distinct phosphatidylinositol 3-kinase complexes with mammalian Atg14 and UVRAG. *Mol. Biol. Cell* **19**, 5360-5372.

Juhasz, G., Hill, J. H., Yan, Y., Sass, M., Baehrecke, E. H., Backer, J. M. and Neufeld, T. P. (2008). The class III PI(3)K Vps34 promotes autophagy and endocytosis but not TOR signaling in Drosophila. *J. Cell Biol.* **181**, 655-666.

Jung, C. H., Jun, C. B., Ro, S. H., Kim, Y. M., Otto, N. M., Cao, J., Kundu, M. and Kim, D. H. (2009). ULK-Atg13-FIP200 complexes mediate mTOR signaling to the autophagy machinery. *Mol. Biol. Cell* **20**, 1992-2003.

Kihara, A., Noda, T., Ishihara, N. and Ohsumi, Y. (2001). Two distinct Vps34 phosphatidylinositol 3-kinase complexes function in autophagy and carboxypeptidase Y sorting in Saccharomyces cerevisiae. *J. Cell Biol.* **152**, 519-530.

Kimura, S., Noda, T. and Yoshimori, T. (2007). Dissection of the autophagosome maturation process by a novel reporter protein, tandem fluorescent-tagged LC3. *Autophagy* **3**, 452-460.

Klionsky, D. J. (2007). Autophagy: from phenomenology to molecular understanding in less than a decade. *Nat. Rev. Mol. Cell Biol.* **8**, 931-937.

Kontaridis, M. I., Swanson, K. D., David, F. S., Barford, D. and Neel, B. G. (2006). PTPN11 (Shp2) mutations in LEOP ARD syndrome have dominant negative, not activating, effects. *J. Biol. Chem.* **281**, 6785-6792.

Lorenzo, O., Urbe, S. and Clague, M. J. (2006). Systematic analysis of myotubularins: heteromeric interactions, subcellular localisation and endosome related functions. *J. Cell Sci.* **119**, 2953-2959.

Mohi, M. G. and Neel, B. G. (2007). The role of Shp2 (PTPN1 1) in cancer. *Curr. Opin. Genet. Dev.* **17**, 23-30.

Mohi, M. G., Williams, I. R., Dearolf, C. R., Chan, G., Kutok, J. L., Cohen, S., Morgan, K., Boulton, C., Shigematsu, H., Keilhack, H. et al. (2005). Prognostic, therapeutic, and mechanistic implications of a mouse model of leukemia evoked by Shp2 (PTPN11) mutations. *Cancer Cell* **7**, 179-191.

Murray, J. T., Panaretou, C., Stenmark, H., Miaczynska, M. and Backer, J. M. (2002). Role of Rab5 in the recruitment of hVps34/p150 to the early endosome. *Traffic* **3**, 416-427.

Obara, K., Noda, T., Niimi, K. and Ohsumi, Y. (2008a). Transport of phosphatidylinositol 3-phosphate into the vacuole via autophagic membranes in Saccharomyces cerevisiae. *Genes Cells* **13**, 537-547.

Obara, K., Sekito, T., Niimi, K. and Ohsumi, Y. (2008b). The Atg18-Atg2 complex is recruited to autophagic membranes via phosphatidylinositol 3-phosphate and exerts an essential function. *J. Biol. Chem.* **283**, 23972-23980.

Petiot, A., Ogier-Denis, E., Blommaart, E. F., Meijer, A. J. and Codogno, P. (2000). Distinct classes of phosphatidylinositol 3′-kinases are involved in signaling pathways that control macroautophagy in HT-29 cells. *J. Biol. Chem.* **275**, 992-998.

Proikas-Cezanne, T., Waddell, S., Gaugel, A., Frickey, T., Lupas, A. and Nordheim, A. (2004). WIPI-1alpha (WIPI49), a member of the novel 7-bladed WIPI protein family, is aberrantly expressed in human cancer and is linked to starvation-induced autophagy. *Oncogene* **23**, 9314-9325.

Pulido, R., Serra-Pages, C., Tang, M. and Streuli, M. (1995). The LAR/PTP delta/PTP sigma subfamily of transmembrane protein-tyrosine-phosphatases: multiple human LAR, PTP delta, and PTP sigma isoforms are expressed in a tissue-specific manner and associate with the LAR-interacting protein LIP.1. *Proc. Natl. Acad. Sci. USA* **92**, 11686-11690.

Ruhe, J. E., Streit, S., Hart, S. and Ullrich, A. (2006). EGFR signaling leads to downregulation of PTP-LAR via TACE-mediated proteolytic processing. *Cell. Signal.* **18**, 1515-1527.

Rutherford, A. C., Traer, C., Wassmer, T., Pattni, K., Bujny, M. V., Carlton, J. G., Stenmark, H. and Cullen, P. J. (2006). The mammalian phosphatidylinositol 3-phosphate 5-kinase (PIKfyve) regulates endosome-to-TGN retrograde transport. *J. Cell Sci.* **119**, 3944-3957.

Taguchi-Atarashi, N., Hamasaki, M., Matsunaga, K., Omori, H., Ktistakis, N. T., Yoshimori, T. and Noda, T. (2010). Modulation of local PtdIns3P levels by the PI phosphatase MTMR3 regulates constitutive autophagy. *Traffic* **11**, 468-478.

Tanida, I., Minematsu-Ikeguchi, N., Ueno, T. and Kominami, E. (2005). Lysosomal turnover, but not a cellular level, of endogenous LC3 is a marker for autophagy. *Autophagy* **1**, 84-91.

Uetani, N., Chagnon, M. J., Kennedy, T. E., Iwakura, Y. and Tremblay, M. L. (2006). Mammalian motoneuron axon targeting requires receptor protein tyrosine phosphatases sigma and delta. *J. Neurosci.* **26**, 5872-5880.

Vergne, I., Roberts, E., Elmaoued, R. A., Tosch, V., Delgado, M. A., Proikas-Cezanne, T., Laporte, J. and Deretic, V. (2009). Control of autophagy initiation by phosphoinositide 3-phosphatase jumpy. *EMBO J.* **28**, 2244-2258.

Wallace, M. J., Batt, J., Fladd, C. A., Henderson, J. T., Skarnes, W. and Rotin, D. (1999). Neuronal defects and posterior pituitary hypoplasia in mice lacking the receptor tyrosine phosphatase PTPsigma. *Nat. Genet.* **21**, 334-338.

Walsh, J. P., Caldwell, K. K. and Majerus, P. W. (1991). Formation of phosphatidylinositol 3-phosphate by isomerization from phosphatidylinositol 4-phosphate. *Proc. Natl. Acad. Sci. USA* **88**, 9184-9187.

Zhong, Y., Wang, Q. J., Li, X., Yan, Y., Backer, J. M., Chait, B. T., Heintz, N. and Yue, Z. (2009). Distinct regulation of autophagic activity by Atg14L and Rubicon associated with Beclin 1-phosphatidylinositol-3-kinase complex. *Nat. Cell Biol.* **11**, 468-476.

Supplementary Material, Figure 1 (MacKeigan)

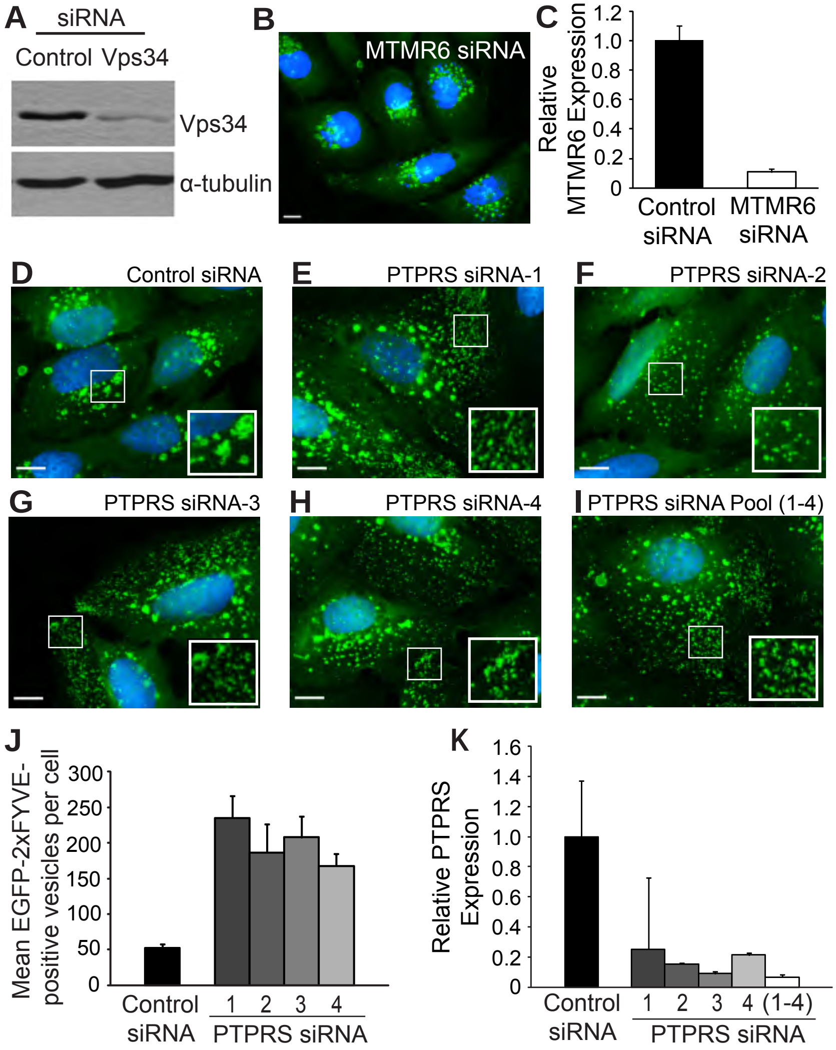

Supplementary Material, Figure 1 Continued (MacKeigan)

Fig. S1. Target genes are effectively knocked down by siRNA. (**A**) Western blot analysis of whole cell extracts following transfection with control or VPS34 siRNA shows depletion of VPS34 protein levels. α-tubulin was probed as a loading control. (**B**) U2OS-EGFP-2xFYVE cells were transfected with MTMR6 siRNA, fixed, and imaged at 60x by fluorescent microscopy as in Fig. 1. A bar, 10 µm. (C) MTMR6 mRNA was depleted by 96% following transfection with MTMR6 siRNA for 48 hours. RNA extracted from control- or MTMR6- siRNA transfected cells was converted to cDNA and MTMR6 levels determined by qRT-PCR using gene-specific primers. Values were normalized to GAPDH. (**D-I**) U2OS-EGFP-2xFYVE cells were transfected with control (D) or PTPRS siRNA [E, siRNA-1, F, siRNA-2, G, siRNA-3, H, siRNA-4, I, siRNA-pool (1-4)] for 48 hours, fixed, and imaged by fluorescent microscopy (green: PI(3)P, EGFP-2xFYVE; blue: nuclei). Insets are 2x magnifications of boxed regions, highlighting the abundant vesicles caused by PTPRS siRNA transfection. Bars, 10 µm. (**J**) EGFP-2xFYVE punctae were quantified from cells following PTPRS knockdown with four unique siRNAs. Values represent means and bars represent s.e.m. (**K**) PTPRS mRNA knockdown following 48 hour transfection with four unique siRNAs (individually or pooled) was determined by qRT-PCR using gene-specific primers and GAPDH normalization, as described above.

Supplementary Material, Figure 2 (MacKeigan)

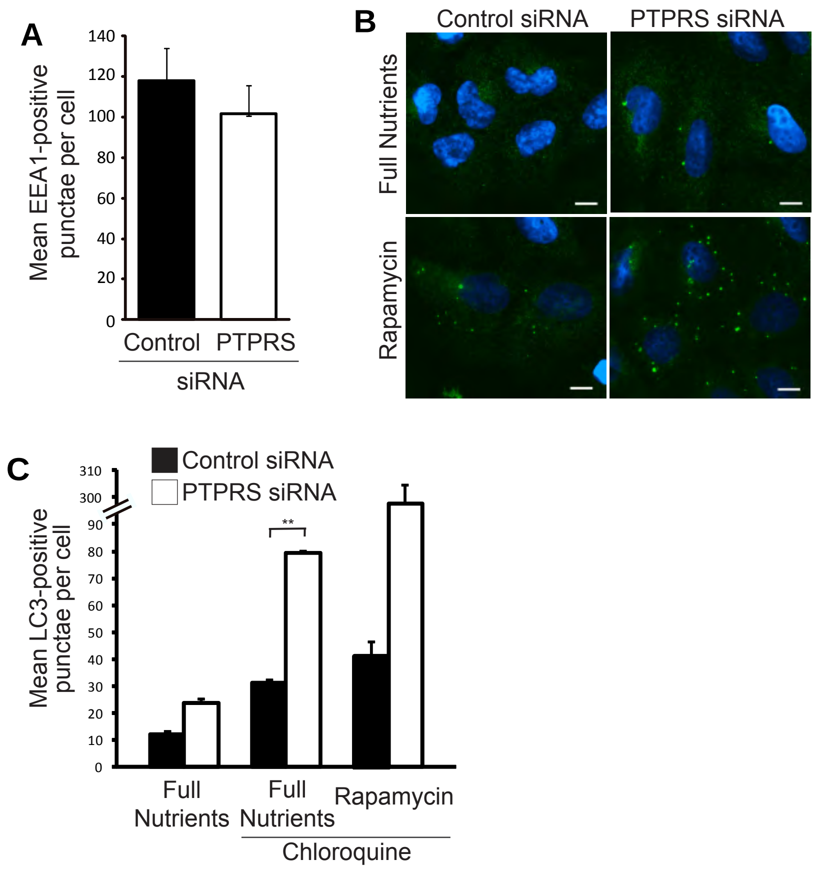

Fig. S2. PTPsigma knockdown increases the abundance of autophagic, but not endocytic, vesicles. (**A**) U2OS cells were transfected with control or PTPRS siRNAs, fixed, and immunostained with anti-EEA1 antibodies (see Fig. 1H). EEA1-positive vesicles were quantified using image analysis software. Bars represent s.e.m. (**B**) U2OS cells transfected with control (left panels) or PTPRS (right panels) siRNAs were cultured for 1 hour with nutrient-rich medium (top panels) or 50 nM rapamycin (bottom panels). Cells were stained with anti-ATG12 antibodies and imaged by fluorescent microscopy at 60x (green: ATG12; blue: nuclei). Bars, 10 µm. (**C**) U2OS cells transfected with control or PTPRS siRNAs were cultured for 1 hour with normal growth media (full nutrients; left), 25 µM chloroquine in normal growth media (middle), or 50 nM rapamycin and 25 µM chloroquine in normal growth media (right). Cells were fixed, immunostained with anti-LC3B antibodies, and imaged by fluorescent microscopy at 60x. LC3-positive punctae were quantified images using image analysis software (black: control siRNA; white: PTPRS siRNAs). Bars represent s.e.m., *$p < 0.05$, **$p < 0.01$.

Supplementary Material, Figure 3 (MacKeigan)

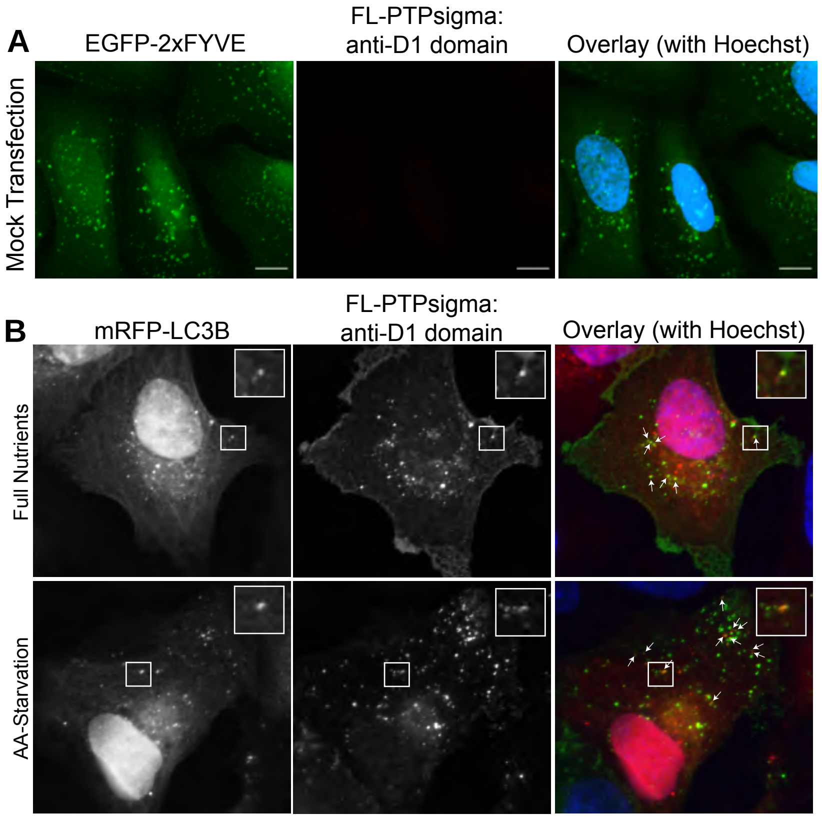

Fig. S3. FL-PTPsigma colocalization with mRFP-LC3 and mock control for FL-PTPsigma immunofluorescence. (**A**) U2OS-EGFP-2xFYVE cells were mock transfected (with transfection reagent but no DNA) for 24 hours, stained with PTPsigma (anti-D1) antibodies, and imaged as in Fig. 4A-C, Fig. 5, and (B). Absence of signal in the red channel demonstrates specificity of FL-PTPsigma expression captured in the above figures [green: PI(3)P; red: anti-PTPsigma (D1-targeted antibodies); blue: nuclei]. Bars, 10 µm. (**B**) FL-PTPsigma was transiently expressed in U2OS-mRFP-LC3 cells and LC3 and PTPsigma imaged by fluorescent microscopy following 2 hour incubation with full nutrient media (top panels) or amino acid-starvation media (lower panels) [red: mRFP-LC3; green: PTPsigma (D1-targeted antibodies); blue: nuclei]. Insets are 2x magnifications of boxed regions. White arrows indicated punctae positive for both PTPsigma and LC3.

Supplementary Material, Figure 4 (MacKeigan)

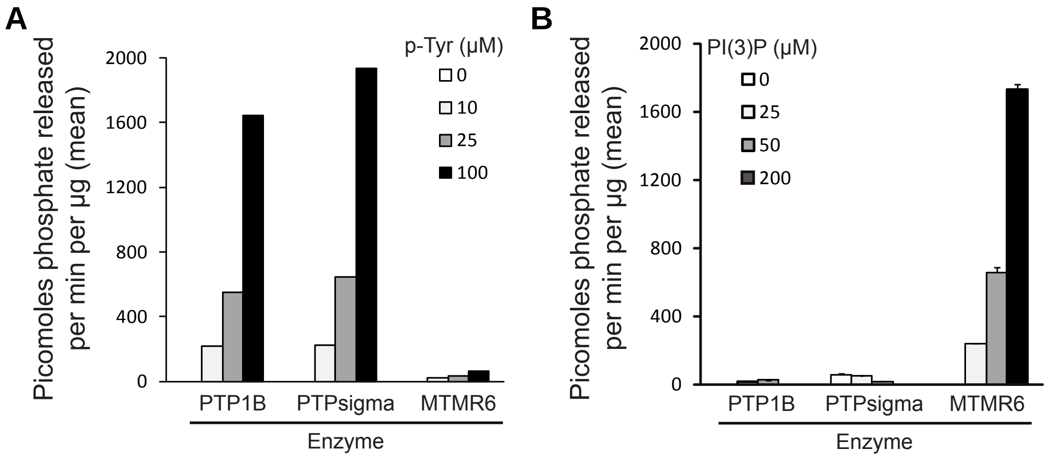

Fig. S4. PTPsigma dephosphorylates phosphotyrosine, but not PI(3)P, in vitro. (**A**) Recombinant GST-fusions of PTP1B (left), PTPsigma (middle) and MTMR6 (right) were incubated with a phosphotyrosine peptide at the indicated concentrations for 15 minutes at 37°C and released phosphates measured by malachite green quenching and 650 nm absorbance. (**B**) Recombinant GST-fusions of PTP1B (left), PTPsigma (middle) and MTMR6 (right) were incubated with water-soluble PI(3)P substrate at the indicated concentrations and released phosphates measured by malachite green quenching and 650 nm absorbance. Bars represent s.d.m.

Gene Symbol	Description	Score	Rank	siRNA sequence 1	siRNA sequence 2	siRNA sequence 3	siRNA sequence 4
ACP1	acid phosphatase 1, soluble	25	40	CCCATAGTGCACACTTGTATA	TCCGTAGGAGCTCACAGTCTA	TCGGTGTGTAATCACGTTCCA	ATGGATGAAAGCAATCTGAGA
ACP2	acid phosphatase 2, lysosomal	-17	176	CAGCCTGAAGTCTTCGGCAAA	CTGGATGTCTACAATGGTGAA	ACCAGTGAAGACATATCCCAA	CAGCGCTATCACGGCTTCCTA
ACP5	acid phosphatase 5, tartrate res	25	41	CTCGGGCAAGTCCCTCTTTAA	CTGGTACGTGCTAGCCGGAAA	ACGGCGCTGCTCATCCTGCAA	CACTGGTGTGCAAGACATCAA
ACP6	acid phosphatase 6, lysophosp	-8	167	CCATGTCAGTTTATACCTTAA	CCCGCTGGACATGTTCTTGAA	GTGCCTTTATACAATGCCAAA	GAGGCCAAACTTGAAATACAA
ACPP	acid phosphatase, prostate	42	20	ACAGATGGCGCTAGATGTTTA	CCGGACTTTGATGAGTGCTAT	CTCTATTACCATTATGGATAA	ATGAACAGGTTTATATTCGAA
ACPT	acid phosphatase, testicular	0	117	CCCGCCAAAGATGGAGGGAAT	CTGGTGTTCGTGGCTCTGGTA	CTGCTGAATGCTATCCTTGCA	CAGGGCATGGAAGGTTCTGGA
ALPI	alkaline phosphatase, intestinal	58	9	CACGTCCATCCTGTACGGCAA	TCCATTCTCCTAGGAGACAAA	CCAGACAATAAAGGGACCAAA	CCGGGCTACGTGTTCAACTCA
ALPL	alkaline phosphatase, liver/bon	25	42	CAGGATTGGAACATCAGTTAA	CCGGGACTGGTACTCAGACAA	CAGACTGCAGACATTCTCAAA	CACCATGATTTCACCATTCTT
ALPPL2	alkaline phosphatase, placental	17	63	CTGGGAAACACAAAGCAATAA	TTGCTTTATCTTGCTCTTGAA	ATCGACCATGGTCATCATGAA	CACGGTCCTCCTATACGGAAA
CDC25A	cell division cycle 25A	17	64	AAGGCGCTATTTGGCGCTTCA	AAGGGTTATCTCTTTCATACA	CAGCTTAGCTAGCATTACTAA	CTGGCCAAATAGCAAAGACAA
CDC25B	cell division cycle 25B	50	13	CAGGAGGCTGAGGAACCTAAA	CCCAGTCTGTTGAGTTAGTTA	CGCCGAGAGCTTCCTACTGAA	TTGGGTTAATACCAGCTTAAA
CDC25C	cell division cycle 25C	17	65	CAGGAAGGGCTTATGTTTAAA	CCAGAGCTATATATCCTTAAA	CCAGGGAGCCTTAAACTTATA	GAGCTGCAATCTAGTTAACTA
CDKN3	cyclin-dependent kinase inhibit	25	43	CACAATCAAGATCTGTATCAA	TCGGGACAAATTAGCTGCACA	CACCAGTGTTATCAACTTGAA	CTAGCATAATTTGTATTGAAA
CTDP1	CTD (carboxy-terminal domain,	0	118	CCGGCTGTACGCACACACCAT	CTCCATGGTTTGCATTATTGA	CCCGACAAACTTCCCGATAGA	CCGAATATTATCAAGGGATGA
CTDSP2	CTD (carboxy-terminal domain,	8	85	CCCGGAAACAGCGGGAAGTAA	TACGATCAGCGTGACAGAGTA	CCACCTAGCCATAGTCTCAAA	CTGCGTATAAGGAGGAAGCAA
CTDSPL	CTD (carboxy-terminal domain,	8	86	CCAGTGCAACGTCAGCTTAAA	TACGCCCAACTCTTTAGCCAA	TAGGAAATGCTACATGCGGAA	TTCGTTTAAGCCTATTAGTAA
DKFZP566K0524	DKFZP566K0524 protein	17	66	CCCACCCTAACACTTAACATA	CTGGTGACAAGCTATACCTAA	TTGAATTGGTTGAATAATTAA	TCACCTCTGTTGAAACATTTA
DOLPP1	dolichyl pyrophosphate phosph	0	119	AAGAATGCACCAAACAAACAA	CAGGGTCTACCTGCTGTACCA	GAGGTGGTTTGATTTAAGAAA	CAGGATGGACAGGATGACAGA
DUSP10	dual specificity phosphatase 10	8	87	ATGAGAATACAGGCTCTCTAA	CAGGTTCATAGACCGAAGATA	CAGGGCAGCTTAAGTGGTCTA	CCGAAGATACTACACACTTTA
DUSP11	dual specificity phosphatase 11	8	88	CAGAAACTGTTCCTTACTTAA	CCCTTATGTATTCAAGCTTAA	CACAATAAGCCTGTTAAACAA	ATGATGCAATTGAATTATTCA
DUSP12	dual specificity phosphatase 12	0	120	ATGCTTTACATGGCAATCAAA	TACCGTTTCACAAGGATTGAA	CTCAATGTACATCTTATTTCA	CAAGCTCAATGTACATCTTAT
DUSP13	dual specificity phosphatase 13	42	21	ACCCTGAGATGTAAACAGCAA	TCAGTCCATCTCTATAATAAA	ACCCAATTCAGAGATTCTTTA	CAGGTGGACACAGGTGCCAAA
DUSP14	dual specificity phosphatase 14	8	89	AAGGGAATGCATACATTGCTA	ACCCTTATTATTTAGCTGTTA	CCCAGGATTATATTAGCATTA	TAGCTGTTAAGTAACTATAAT
DUSP15	dual specificity phosphatase-lik	-42	198	ACGGGCCTGGAGGGTATTAAA	CACCACGATTGTGACAGCGTA	CTGGAGGGTATTAAAGAGACA	CCGAAATAAGATCACACACAT
DUSP16	dual specificity phosphatase 16	0	121	AAGGTTGTAGTTTACGATCAA	CCGGCCATTTGTGGAATACAA	CAGGACAAAGTGTTAATTACA	AACCCAGTTGTTACTCTCTTA
DUSP18	dual specificity phosphatase 18	33	29	ACGGGTCTCTCTCCCGAAGAA	CCAGATCACCATGGTCATCAA	CAGGAATGAATCTGCTACAAT	CAAGCTCATGCTGTCTAGCAA
DUSP19	dual specificity phosphatase 19	-8	168	ATGGTCAGTATCACTGGATAA	CAGAGTTAACCTAATGAGTCA	TACGGTCCTCTTTCTCACATA	AAGGTCATATATACTATACAA
DUSP2	dual specificity phosphatase 2	33	30	CAGCCTGAGAGCTCCAAGGAA	CTGGTCCACCACCATGTTGAA	AAACTTAGCACTTTATATTTA	CGCGGGAAAGACCGAAAGGAA
DUSP21	dual specificity phosphatase 21	0	122	AACGTAGTAAGCCTTACCTTA	TCGGTGGAAGTGGTCAACGTA	ACCGGATGGTGCCTTGTTAAA	ACGTACGATGATATCAATGTA
DUSP22	dual specificity phosphatase 22	0	123	CATGTTTATGTTGAGAACTAA	GGGCAACTTAGCCAAGTTTAA	AAGCAACATAGAGTTTAAGTA	AAGCATGAGGTCCATCAGTAT
DUSP23	dual specificity phosphatase 23	0	124	CAGTTCTACCAGCGAACGAAA	GAAGTGGACTAAAGTATTAAA	TTGGCTGAAGACACTGAAGTA	CAGGAGATGCCATTGCTGAAA
DUSP24	dual specificity phosphatase 24	-33	193	AAGCTTCTGCACATCCGGATA	CAAGATTCAGAAGGACTTGAA	CACCCTGGAGATACTCTTAAA	CTGCCTGAAAGTCTCATGTTA
DUSP3	dual specificity phosphatase 3 (	-33	194	CCCGCGGATCTACGTGGGCAA	CCGTATTTACTTAACAAGATT	AACAGATTCGTTGGAAGCTTA	TACGTTATTGTTATTATGGAA
DUSP6	dual specificity phosphatase 6	25	44	CTGCATTGCGAGACCAATCTA	TACGGACACTATTATCACTAA	TGCGGAATTGGTTAATACTAA	TCAGCTGTGCTAAACAGTATA
DUSP7	dual specificity phosphatase 7	33	31	CAAGGTGGTTTCAACAAGTTT	CGGCGGCGAGTTCACCTACAA	TACGACTTTGTCAAGAGGAAA	GAAGATGAACCTGTCACTCAA
DUSP8	dual specificity phosphatase 8	42	22	CCGCTCCTTCGTGGAGTACAA	TCCATCGAGTTCATCGATAAA	CAGGCCCGTTATAAATGTATA	GCGGGTGGTCCTCGAGCTCTA
DUT	dUTP pyrophosphatase	42	23	AAGCCTTGGATGACACCGAAA	TCCCTTCTCTTCACTAGTCTA	AAGCCTGTATTTAACTCATAT	AAAGCCTGTATTTAACTCATA
ENPP1	ectonucleotide pyrophosphatas	0	125	CACCGGCTCCTAATAACGGAA	CAGATAAATACTATTCATTTA	TGGGCAAACAGTAGACTTATA	AAGCATGAAACTTTACCCTAT
ENPP2	ectonucleotide pyrophosphatas	-33	195	ATGGATCATTATGCTGCGGAA	CGGACTAGATATGATATCTTA	AAGCCTTATAAACCAATCTTA	CAGATATATTTAAGCCTTATA
ENPP3	ectonucleotide pyrophosphatas	0	126	AACCTAATGTGTGATCTTCTA	CTGGCTGTTAGGAGTAAATCA	TAGCAATTTGGTACCTATGTA	ATGGTTATAACAATGAGTTTA
FBP1	fructose-1,6-bisphosphatase 1	0	127	CTCGCTCTGCACAGCAGTCAA	TTCCTAGAGAGCAGAAATAAA	CCTGGTTATGAACATGTTAAA	CTCCAACGACCTGGTTATGAA
FBP2	fructose-1,6-bisphosphatase 2	0	128	AGGACCCTAAATGAACGATAA	CAGGTTATGCGCTGTACGGTA	TCCACTTAATCACATACAGAA	CTCAATGCTGACGGCCATCAA
FLJ32332	likely ortholog of mouse protein	-17	177	CAGAGTGACTTTACAACTTAA	CCCAGAGACTCGGATTATCAA	CAGGATCTTGAACAGCCCAAA	TCGGATTATCAATGCAGAGAA

G6PC	glucose-6-phosphatase, catalyt	0	129	CAGCAGGTGTATACTACGTGA	TGGGATCCAGTCAACACATTA	CTGGCTTATTCCCATGTGTGA	TAGCAGAGCAATCACCACCAA
G6PC2	glucose-6-phosphatase, catalyt	50	14	CAGAGTATTCATAGCAACACA	CTGGTGGGTCCAAGAAACTCA	TGGTTAAATCTTATATTTAAA	TTGGTTAAATCTTATATTTAA
G6PC3	glucose 6 phosphatase, catalyt	0	130	CAGGTGCTGGCTGGCCTAATA	GTGGCTCAACCTCATCTTCAA	CACATGTTCAGTGCCCAGGAA	CTGGGAAATGGCCAGAAGATA
ILKAP	integrin-linked kinase-associate	0	131	ATGGAGGAATTCGAGCCTCAA	CCCGCTAGCAGTGGCGATTCA	TCGGGCAATCTTGTGTCGTTA	TTCGGTGATCTTTGGTCTGAA
IMPA1	inositol(myo)-1(or 4)-monophos	-17	178	ACGAAGAGTAATTGCTGCAAA	CCGGAAGAGACGAGTGCGGTA	TAGAAAGTTAACTGTTTGGAA	CCAGATTTGGTGACTCATCAA
INPP1	inositol polyphosphate-1-phosp	50	15	CCGTAATTAGTACAAGTGAAA	TAGATTCAACTTATCAGTATA	CTGATGGGAGTCATCAATCAA	CACCAGCAGCTGCAACTGAAA
INPP4B	inositol polyphosphate-4-phosp	8	90	AACGATTTGCCGCAAACTGAA	CCCGGAAAGTGTGAGCGGAAA	ATCGATGTCAGTGACACTTGA	CTCCATAGATTTGAAACAGAA
INPP5A	inositol polyphosphate-5-phosp	8	91	CGGAAGGTTATGCTCCAGTTA	TCGAGTGATGCGATGAAAGAA	AACAATAATATCATGGGAGAA	CGAGTGCAAATGGTCAAGAAA
INPP5B	inositol polyphosphate-5-phosp	33	32	TTGCGGGAACATACAATGTAA	AAGAAGAGGATTACACCTATA	GAGGGCAATACAGGCATTTAA	CTGCGAGATACAATTGTGAAA
INPP5D	inositol polyphosphate-5-phosp	0	132	CAGGTGCTATGCCACATTGAA	TCCCATCAACATGGTGTCCAA	CCCGGGACTGTTGACAGCCAA	TCGGAATTGCGTTTACACTTA
INPP5E	inositol polyphosphate-5-phosp	0	133	ACGCATCGTGTCTCAGATCAA	ACGGATTTCGAAGGAGATTCA	CACGTACGACAGCACCTCCAA	CAGAAATGTGCCCGACACCAA
INPP5F	inositol polyphosphate-5-phosp	50	18	AAGACCTTTACGCATATTAAA	CAGATCTTCCATGGTGGCTTA	CTGAAATAATGTGTTTCTGAA	TACCATCTCCTGATGACTCAA
ITPA	inosine triphosphatase (nucleos	8	92	CTGGAGAAGTTAAAGCCTGAA	CTGGATGAGACTTGTTTCCAA	GAGGAGGTCGTTCAGATTCTA	CAGGAGGCAGTTCGCCAGGTA
LHPP	phospholysine phosphohistidine	8	93	CAGGAGGAAACTAACAGTTCA	CCCAGTCACCTTTGCAGACAA	CCCGGTGTGTGCAGGAGGAAA	ACCACTCACCATGGGCCTTTA
LOC387870	similar to protein tyrosine phos	0	134	TAGCAGAAAGAGGAACTTTAA	CACGATATGTTTGTCTTGGAA	CCAGGTGGTATTGTTAAAGTA	CAGGATCGTGTTCACAAGGAT
LOC389772	similar to Osteotesticular phos	0	135	TACATTCTAGTAAGCATCTTA	TAGTTTAAATATATACAATAA	AAAGCAATATGTAAATCTTAA	AACATTATGTTGTATAGTTTA
LOC391025	similar to protein tyrosine phos	56	12	CTCATTAATTATGATTATTGA	CAAAGGATTCCGGAACAGAAA	CAGGAGGGTCCTGTTGGCTCA	CAGATGAGTCTCAGCACAAAT
LOC400927	similar to TPTE and PTEN hom	17	67	TCCAGGTGATCTGAACCTGAA	ATGGATGTTCTTCTTCGAGTA	TCCACAGACAAACGAATTTAA	CTGGTGTCACCTATCAGTAAA
LOC442428	similar to fructose-1,6-bisphosp	25	45	CAACATTGTGACCATAGTTTA	CAAGATTAGTAAGAAAGGAAA	CAGCCTTATGGACTCTCTCAA	CACCTGGATGCTACCAGGCTA
LOC474338	SUMO1 pseudogene 3	-8	169	CAGGCTTGTGGTGATAAATAA	AAGGAAGGTGAATATATTAAA	CTCATTATTCATTATTGTTTA	CAGAGAATTGCTGATAATCAT
LPPR2	lipid phosphate phosphatase-re	0	136	CCCGTGTCTAAGCATGTGCAA	CCGGGACAACTTCAGCCCTTA	CTGCGTTGTGCATAACTTTCA	CCGCGTGGCCGAGTACCGAAA
MINPP1	multiple inositol polyphosphate	-42	199	CACGGTCAAACAGATCCGCAA	CCGAGTGCAGATGTTATTAAA	AAGTCGGAAAGTACAATGAAA	ATGAAATTCTTCCTACTTATA
M-RIP	myosin phosphatase-Rho intera	25	46	AAGCGGGACTTCACCAATGAA	CCGGACCAACAAGCAGAATCA	CGGGAGCTAGAGAAACTTCGA	GCGACGGTTCTTCATCCTTTA
MTM1	myotubularin 1	25	47	CGAATAGGTCATGGTGATAAA	TCGGTATGAGTGGGAAACGAA	GACATTGTTTATCCTAATGTA	CGGTATGAGTGGGAAACGAAA
MTMR2	myotubularin related protein 2	25	48	AACGATATGAACTTTGTGATA	CTGAGGGAGTCTAACAAGTTA	ACCACTGCAATTCACATTATA	TAGGATGAGTTTAGAACTGTA
MTMR3	myotubularin related protein 3	0	137	GACCCTTATTACCGAACCATA	TTGCCTTTAGCCGAATGTAAA	CAGCCTTAAATCAAGAATATT	AGCATGTAACTTCAAGGTTTA
MTMR4	myotubularin related protein 4	17	68	TCGGCACTGGAGAGTACCAAA	TTGCCATAGATGTAACCTAAA	AAGAGTGGCTCTCACGGCTAA	CCGGCTGCATATCAAATTCAA
MTMR6	myotubularin related protein 6	33	33	CCCGGATAGCAAGCAAACCAA	CCCGTAAATGATGCTCTTCGA	TACAAAGTTACTGTTTAACAA	AAGGGAAGTACAGATAGTTTA
MTMR8	myotubularin related protein 8	8	94	CAGCCCAAGCAGAGTATGCTA	CGGGAAGATCTAAGAGTCTAT	GGGAATTACTTTACTGATTAA	TGCCATGAGGTTTATATTTCA
MTMR9	myotubularin related protein 9	8	95	CAGACCTAGTATTCTAAGTTA	CAGGTCTAAGGATTAACTATA	ATGCCTGAACCTGTTATCTAA	TACGTTGGAATAGATCCTCTA
PDP2	pyruvate dehydrogenase phosp	8	96	CAGGACGATCATCATGGAGGA	TAGACAGGACAGGTTAATTTA	CAGGAATTAGACCATATTTAG	CCCATCCTATTGTCAAGGTTA
PDPR	pyruvate dehydrogenase phosp	58	10	ACCACATAGCCCAGTGATTAA	ATCTCTTATCTCCTTGATATA	TAGCTACAAGATTCAGCTTTA	TTGGAGCAAGTATGTACTTAA
PHOSPHO1	phosphatase, orphan 1	-8	170	CGCCAACATGTGCAAGCACAA	TCGGGTCCGGACAGCCAGTAA	TACAACTATAAAGGAGGTGAA	CCGTCCCTATCTATTCAGTTA
PHPT1	phosphohistidine phosphatase	17	69	CACGCCATTTCAACTGAGAAA	TCGGGCGACATGCAGAAGCAA	CCGATTCCACGTTTCCTTTAA	TAGCCTGGCCACAGAATTAAA
PIB5PA	phosphatidylinositol (4,5) bisph	25	49	CAGGTAACATTCAGTGAGGAA	CTGGGACTGGATCGGCTTATA	CTGGAGGTCATCCATTAGGAA	ATGGGAATACCTACCAGGTAA
PIP3AP	phosphatidylinositol-3-phospha	0	138	CAGGGTCATGGCATACCAATA	TGGGATGTGGATTATGCTTAA	CCGGCACTCCGTTAGAATAAA	CCCGGCACTCCGTTAGAATAA
PLIP	PTEN-like phosphatase	17	70	CAGCTGCGGCTCAGCACAGTA	CACCTTGGACAACCTCCAGAA	AACCTCCAGAAGGGAGTCCAA	CAGGAGTGGAAGAGACTAGGA
PME-1	protein phosphatase methylest	33	34	AACATCGAGCTCTGTTGTAAA	AGGCGATACATCTGAGTTCAA	AGGAAGGAAGTGAGTCTATAA	ACGGCAGCGATTATTAGTAGA
PNKP	polynucleotide kinase 3'-phosp	17	71	CACGTGAACAGGGACACGCTA	CACGTGTGAGACAGCCCTGAA	CGGGAAGTCCACCTTTCTCAA	CAAGCTGGTGATCTTCACCAA
PPAP2A	phosphatidic acid phosphatase	8	97	AACCCTGTCTGTTTACTGTAA	CTGACATTGCCAAGTATTCAA	CATGCTGTTTGTGGCACTTTA	CCGGGCAGAGACCATGTTTGA
PPAP2B	phosphatidic acid phosphatase	8	98	AGCGATCGTCCCGGAGAGCAA	CAGCACAATTTCAGAAGAAAT	CCGGATCTATTACCTGAAGAA	CCGGGCACTTGCATACTCTTA
PPAP2C	phosphatidic acid phosphatase	8	99	CCGGGTCAACTGCTCGGTCTA	TCGCTCGGACTTCAACAACTA	ACCCGCGTGTCTGATTACAAA	CATGGTGTTCTTGGCGCTGTA
PPEF1	protein phosphatase, EF hand	17	72	CAGCATTAGTACCTACATATT	CCCAATCGGTACAATCGTTGA	ATCGAATATGCTGATGAACAA	CTGGGAAACCCTCTTCAATAA
PPEF2	protein phosphatase, EF hand	8	100	CACATGAATATCGACATTACA	CTGCAGGAGCATTGCGCTTAA	CCCACAAGCTACAAATGCTAA	CGGAGCATTGATTTCAACAAA
PPFIA1	protein tyrosine phosphatase, r	0	139	AACGGCCTATTTAATATGTTA	CACGAGGTTGGTCATGAAAGA	CTGGTGTTTCCGAGACGGATA	TTCCAAGGTACAAACTCTTAA

PPFIA2	protein tyrosine phosphatase, r	0	140	AACGTTTGGGTGACTCATGAA	TACCAGCTGGATTTAGGTTAA	TCCAATGAACGCCTACAACTA	ACCGATGAAACTAGTCAAATA
PPFIA3	protein tyrosine phosphatase, r	25	50	ACGGCTCAACTATGACCGGAA	CACGGGTAAAGAGAACTGTTT	TCGAATGTTAGATCACCTTAA	CTGGTGGACGCTCGAATGTTA
PPFIA4	protein tyrosine phosphatase, r	25	51	CAGGATAGCTGGGTCCATTCA	TGGGTGTGTACGTACCAATAA	CAGGGACTCAGTCCAGATTAT	TCCCTGGGTAATGGATGGTAA
PPM1A	protein phosphatase 1A (forme	-58	204	AAGCGTGATTTCAAACCATAA	TTCCATGAGTATTGCAGGTAA	CAAACCATAATTCGTGTTGTA	TAAGCGTGATTTCAAACCATA
PPM1B	protein phosphatase 1B (forme	17	73	CACCTAAGCATATCTACTTTA	CGAGATAACATGAGTATTGTA	CAACCAAGTGTTTAGAATGAA	TAGCCTAACTACACACATCAA
PPM1D	protein phosphatase 1D magne	8	101	ACGGGTCTTCCTAGCACATCA	CTCGGCGTCGTCGAAGATAAA	ATGGCCAAGGGTGAATTCTAA	TACATGGAGGACGTTACTCAA
PPM1E	protein phosphatase 1E (PP2C	0	141	CCCATTTAGGTCTGTACTAAA	GAGGCGGTTTATAGTCAGAAA	TTGGTTCTATAAACTAGATAA	CCGCCTAATCATGTGTTTATA
PPM1F	protein phosphatase 1F (PP2C	0	142	ATGGTTGGCCACAAACAATGA	CACCTGGTGGTCTGATTCATA	ACCAAGTATTGCTTGGCTTAA	CAGGTGGTGTTAATAAGCCAT
PPM1G	protein phosphatase 1G (forme	8	102	CAGGACCTGAGGACTCAACTA	CCAGAGGATGAAGTAGAACTA	TACTCTGTGAACTTTATTTAA	GAAGTTGTAGATTTCATTCAA
PPM1L	protein phosphatase 1 (formerl	8	103	CAGGACTACGAGAAAGACAAA	CTGGTGGTCTTAGGTCTATAA	AAGCGTGAACCCATATTGATA	CTGTAGAGTCACATATATGAA
PPM2C	protein phosphatase 2C, magn	8	104	ACCGATTAAGGCCACAGGATA	CAAGATAGTAGTATTATTACA	CAGAATATCATATAATGTTTA	ATCGTACTTCTTATTTAGTAA
PPP1CA	protein phosphatase 1, catalyti	17	74	AAGAGACGCTACAACATCAAA	CCGCAATTCCGCCAAAGCCAA	CTGCCTGCTGCTGGCCTATAA	CAGCGAGAAGCTCAACCTGGA
PPP1CB	protein phosphatase 1, catalyti	-17	179	TACGAGGATGTCGTCCAGGAA	TAGGAATATGGTCGGGCTGAA	AAGTATGTTGGTTAATAGGAA	CACTATTGGATGTGATTCTAA
PPP1CC	protein phosphatase 1, catalyti	17	75	AACATCGACAGCATTATCCAA	CTGGTTATAACAGCAAATGAA	CTGCGGTGAAGTTGAGGCTTA	GAGGAGTAAGTGTACAATTGA
PPP1R10	protein phosphatase 1, regulat	-75	205	CCCAGCCTGCTGAGAAAGATA	CCGAAGGACCGTCACTACATA	CACAGGATCAGCTGCACTTAA	CAGCAACATCTAAGCCCTTGA
PPP1R11	protein phosphatase 1, regulat	0	143	AACATGAGTAGCGAACACTTA	CGCCCTAACTTTGCTTGCTAA	CAGAGATCAGTCAAATCCATA	TGGCTTGAGATTGGTCACTTA
PPP1R12A	protein phosphatase 1, regulat	0	144	ATAGTACTCAACCATAATTAA	CAGAATTAACCCGTGAGTTAA	CAGGCAGGCTATGATGTTAAT	AACGAAGAGCTCTAGAAAGAA
PPP1R12B	protein phosphatase 1, regulat	17	76	CAGGGTGTTGCCTCTAAAGAA	CGGGAGGTAGTAATCCTACAA	CTGGTTGTTGTTATATAGTTT	TAGGAAGATCAGCATATTTAT
PPP1R12C	protein phosphatase 1, regulat	-8	171	CAGCGGGACCTCAACCCAGAA	CAGGAGGACCTTCGGAACCAA	CAGGCGCTTTGGCCTCCTGAA	TTGGAGGAACTGGCCCGGAAA
PPP1R13B	protein phosphatase 1, regulat	50	16	CGCGATGATGCCGATGATATT	CGGGCTGAGAGTCCGGTTTAA	CGCCTTAAATAAGTCAGTTAA	ACCAGCGGCGGTGGAGTTAAA
PPP1R14A	protein phosphatase 1, regulat	-17	180	CCCGATGAGATCAACATTGAT	TTGTATTTAATGGTTCTGTAA	TAATGGTTCTGTAACAATAAA	GCCCAGCTTGCTTGTGTATAA
PPP1R14C	protein phosphatase 1, regulat	0	145	AAGAGCTGCTTTCTCGGATAA	TAAAGTTGTATGAACCCTTAA	AACCCTTAATTTGAAGAACTA	CCGCAGAAGAAGAGTGTATGA
PPP1R14D	protein phosphatase 1, regulat	-25	188	CAGGAGCTCTTCCAGGATCAA	CCGCCTGACAGTGAAGTATGA	CAGGCCTGCCCTGAAACTCCA	GAGCCTGAGATTGACCTGGAA
PPP1R15A	protein phosphatase 1, regulat	0	146	CCAGTTGTTGATCTTATGCAA	TGGGTTTATATAAGGAATAAA	GTGGGTTTATATAAGGAATAA	CAGGATCAGCCGAGGATGAAA
PPP1R15B	protein phosphatase 1, regulat	-25	189	AAGGTGCTAATTTGGAGCCAA	CAGGGTTACTACCTCAGTTTA	AAGGCTTTGTACAGACAGGTA	CAGGTTTATTGTGTCCTACTA
PPP1R16B	protein phosphatase 1, regulat	-100	206	ACGGGCGAGAGTAGCAGTGAA	TCGCAGATCTTTGATATCGTA	CAGGCAATTTCGTTCCTGGAA	ATGGAGCTAGTCTCAGTGCAA
PPP1R1A	protein phosphatase 1, regulat	17	77	AAGGATCACACCCACAATGAA	TTGCCCAGATACATACCTAAA	CAGGGAAGAGTTCTTCCCTTA	GAGGAGGTATCTTGGGATCAA
PPP1R1B	protein phosphatase 1, regulat	33	35	ATAAATCTTTGTAAATAACAA	CAGCTTGTTTGAAGCCCTTGA	CAGGGATTTGCCCTTCACAAT	CTGAGTCTCACCTGCAGTCTA
PPP1R1C	protein phosphatase 1, regulat	67	7	CTCGATCTGGAATTACAGCTA	TTGGAACTGGTTAGTACCTAA	TAGGATTTATGTTATAGATAA	AATGAGTTTAATTGACTTCAA
PPP1R2	protein phosphatase 1, regulat	92	2	CACTACACGTACTGTAATAAA	TACCACTGATTTAGAAACAAA	ATGAGATATATAATCAAAGTA	TTGAATGAGATATATAATCAA
PPP1R2P9	protein phosphatase 1, regulat	17	78	ACGTACAGAGATTACGATTTA	CTGGAGGGCGGTGGACGGCTA	AACGAAGAATTGAACATCAAA	CAAGATGTGAAGAGAAAGAAA
PPP1R3A	protein phosphatase 1, regulat	0	147	CACATCAGTATAGGCCATCAA	TCAGGTGGGATTAATTCTGAA	TAGGCCATCAATATCACAATA	CAGAGGAAACTACTTCAAATA
PPP1R3B	protein phosphatase 1, regulat	17	79	CACCCAAGTTCTTATACGTTA	CCCGCTAGATATGCCATTCAA	CAGACAGTACTTTAAATGTTA	CTAGGATGACATGATGTTATA
PPP1R3C	protein phosphatase 1, regulat	0	148	TACGATGAATTTCAACGACGA	TCCGGAGAATCAAGATCTTAA	TGGCCTCTTATCGATGAATTA	AGCCTTCAACCGATTACTTAA
PPP1R3D	protein phosphatase 1, regulat	-50	200	CAGGTACCCACCAACTTTATA	CTGAGTTAGGCAATCACTTAA	AAGGATAGCTTTCTTCGGTAT	TCAGGTGACTAGAGAATTTCA
PPP1R3F	protein phosphatase 1, regulat	-17	181	CGGGTTGGTACGCGTGCTGAA	AACATGGATGATAACACCTTT	ACCGAAGACCCTGATGATGAA	CACAATAGAGCTCTATGAGAA
PPP1R7	protein phosphatase 1, regulat	-25	190	CACAAACCCAATGGCAATAAA	TCAGATGCCGTTGCAATTAAA	TTCAGATGCCGTTGCAATTAA	CCAGATCAAGAAGATTGAGAA
PPP1R8	protein phosphatase 1, regulat	0	149	CAGGCCCAGGAACTGAAGAAA	TACAAATAAAGATGCCCTAAA	CTGCTGAAGTTTCTTATTTAA	AACCCTGAAGCTGTAAATGAA
PPP1R9A	protein phosphatase 1, regulat	-33	196	CTCCAATGTCAACAGAATTAA	GAGGGTAATATTTATCCTCTA	AAGGATGATTATCTTAAGTTA	CTGCAGTTGGATGGAAATAAA
PPP1R9B	protein phosphatase 1, regulat	0	150	CAACTCGAAGCTGGTCAGCAA	CCCGGGAGGTGCGCAAGATTA	CACTGAGGAATTCCAATTCTA	CCGGGAGGTGCGCAAGATTAA
PPP2CA	protein phosphatase 2 (formerl	0	151	ATGGAACTTGACGATACTCTA	CAAACAATCATTGGAGCTTAA	ACACCTCGTGAATACAATTTA	CAGATACAAATTACTTGTTTA
PPP2CB	protein phosphatase 2 (formerl	0	152	CCGACAAATTACCCAAGTATA	TGGGATCTGTCTTGGCATTAA	ATGGAATTAGATGACACTTTA	CACCGGATACAAACTACTTAT
PPP2R1A	protein phosphatase 2 (formerl	25	52	ACGGCTGAACATCATCTCTAA	CTGGTGTCCGATGCCAACCAA	CAGAGAAATAAAGGTCTAGAA	TCCCATCTTGGGCAAAGACAA
PPP2R1B	protein phosphatase 2 (formerl	92	3	CAGAAGTTAGGTCAAGATGAA	CAGGAAATAACTACTAAGCAA	CTGACGTTCGTTTGAATATCA	TGGACCAATTCTAGATACCAA
PPP2R2A	protein phosphatase 2 (formerl	-8	172	ATGGAAGGTATAGAGATCCTA	CTGCAGATGATTTGCGGATTA	CTCGCCGTGTCTGGCACTGAA	AAGCGAGACATAACCCTAGAA

PPP2R2B	protein phosphatase 2 (formerly	25	53	CAGGAAATGATTGGAATAGAA	CAGGGACTACTTGACCGTCAA	CCGGAAGATCCAAGCAACAGA	CGGCTACAAATAACCTATATA
PPP2R2C	protein phosphatase 2 (formerly	33	36	ACCGCTCATTCTTCTCGGAAA	CCGGGACTACCTTACAGTCAA	TACTGTCACATCATAGATTTA	GAGGTTATTCTCAGTGGATTA
PPP2R2D	protein phosphatase 2, regulato	0	153	CAGAGACTACCTGTCGGTGAA	TAGGTGGTTACCACAACAGAA	TTCATCCATATCCGATGTAAA	CCGCTCCATTAAGAACAGTGA
PPP2R3A	protein phosphatase 2 (formerly	8	105	ACCTGTAGTAATCATGAACAA	CAGGAGGATTTCATCCCTCTA	ACCAAGGTAATCAAACTAATA	TAGCATAACATTACCAAGGTA
PPP2R4	protein phosphatase 2A, regula	33	37	CTCCGGGTGGATGACCAAATA	CTGAGGTGGCTGTTTACCTAA	CCGCTCCCTAAGGGTAACCTA	CGGATTCATCCTTACCCTCAA
PPP2R5A	protein phosphatase 2, regulato	0	154	CAGCGTATTCTGATATAGTAA	CTGTATCATGGCCATAGTATA	CATGGCCATAGTATATTGTAA	CATCAGTATAATATAATTAAA
PPP2R5B	protein phosphatase 2, regulato	-50	201	CCGCATGATCTCAGTGAATAT	CCGGTTCATCTATGAATTCGA	CCGGGAGCGTGAGTACCTCAA	AAGCCAGGGTGGGAACCCTAA
PPP2R5C	protein phosphatase 2, regulato	17	80	AACGAGCTGCTTTAAGTGAAA	CCCATTGGAACAAGTAAGAAA	CTGCTACTTCAGTAAGAATAA	CTGGAAATATTGGGAAGTATA
PPP2R5E	protein phosphatase 2, regulato	-17	182	CACCGGGATTGCAAATCTAAT	CCGGTGATATTGACAATAGGA	CTCGTTCTATATCTCATCACA	AAGGACTTCAATCCAAAGTTT
PPP3CA	protein phosphatase 3 (formerly	-25	191	TAGCGATATAGCATACCCAAA	TCGGCCTGTATGGGACTGTAA	CACGCTTCAGCTACTATCTAA	CTGACATATACTGGAAATGTA
PPP3CB	protein phosphatase 3 (formerly	-17	183	AAGGGTTTGGATAGGATCAAT	TAGGAGATTAGATAGATTCAA	TAGTTTATTGTGAGTACTCAA	CAGCCCGGAAAGAAATCATAA
PPP3CC	protein phosphatase 3 (formerly	25	54	CAGGCTTTCCATCACTTATTA	CCGAGGGTGCTCTTATTTCTA	CTGGACCGAATTAATGAGCGA	CAGGAATAAGATCAGAGCCAT
PPP3R1	protein phosphatase 3 (formerly	-17	184	ATCCTTTAGTACAGCGAGTAA	GCCCATATAATTGGTAATGGA	TCCCTTTATAGTTTCTCTATA	GAGCCTCATGAAGCCAACTAA
PPP4C	protein phosphatase 4 (formerly	-17	185	CGGACAATCGACCGAAAGCAA	TCGCCAGATCACGCAGGTCTA	CTGGACGAGCATCTCCAGAAA	CCAACTGGTGATGGAAGGTTA
PPP4R1	protein phosphatase 4, regulato	0	155	CAGGCGTTGTTAGATCAGTAT	TGGGAGTGCTGCAGTCTTTAA	AACCTGGTAACTACAAATCTA	CAGCTAGTAATGAGAATGATA
PPP5C	protein phosphatase 5, catalytic	42	24	CCCGTTGGCCCAGTGCATCAA	CTCGTGGAAACCACACTCAAA	CAAGGCCTTCTTGGAAGAGAA	CACGGAGGCCTGTTCAGTGAA
PPP6C	protein phosphatase 6, catalytic	-8	173	CACAAATGAGTTTGTTCATAT	CAGCAGCAAAGTTGTTATTCA	CACCCTGGACTCATTTGAGAA	CTGGTTTGGTCAGATCCTGAA
PR48	protein phosphatase 2A 48 kDa	-50	202	CACGTGTCTCTGTCACGTGAA	CTGGGCCTGAGTGAGCAGTAA	TGCGTTTGTACGGAATGATAA	CACCTTCTTCAACATCGAGAA
PSPH	phosphoserine phosphatase	42	25	CCGGCATAAGGGAGCTGGTAA	TGCCAATAGGCTGAAATTCTA	TAGGCTGAAATTCTACTTTAA	CAGAGACTCATAGCAGAGCAA
PSTPIP1	proline-serine-threonine phosph	-8	174	ACCGGGCGCTCTACGATTATA	CCGGCTGACCATTCTCCGCAA	CAGCATAGACGCCGACATCGA	CAAGAAGGCCATGGAGTCCAA
PSTPIP2	proline-serine-threonine phosph	8	106	CCACGTTATGTCAGCAATGAA	CCGGCTAGTGCTTCTGTGATA	CTCAGTGGTGCAAGATTTAAA	ACGAATAAACTTCTTCCGGAA
PTEN	phosphatase and tensin homolo	-17	186	AAGATTTATGATGCACTTATT	CAATTTGAGATTCTACAGTAA	ACGGGAAGACAAGTTCATGTA	TCGGCTTCTCCTGAAAGGGAA
PTP4A1	protein tyrosine phosphatase ty	8	107	ACGCCTTAACACAGCTCTATA	CCCTTTGATCACGTTAATCTA	CCGACCCGTTGCCATGATTAA	CACGTTAATCTAAATCTAGAT
PTP4A2	protein tyrosine phosphatase ty	8	108	AACAGCATACCTGCTAAGCTA	CAGAGAATGCTGGTAGCTTAA	ATGCAACAATAGATTCCATTA	AGGGACTGTGTTGCTTGTGAA
PTP4A3	protein tyrosine phosphatase ty	0	156	CACCCAAGTATTTGCACAATA	CCGCGGAGCCATCAACAGCAA	CACCTTCATTGAGGACCTGAA	CCGGTGGAGGTGAGCTACAAA
PTPDC1	protein tyrosine phosphatase do	17	81	CGGAATGTTGAGTGCCTTCAA	TACGTAGATACCAGAGGCCAA	AGGCTATACATAAGTATTGTA	AACAGAGGGTTTCAAAGCATA
PTPLA	protein tyrosine phosphatase-lik	17	82	ACCACTTGCCATACTTCATTA	CACTGTTTAATTGGAATTGTA	CTGGTGAACTTCTTACAATAT	AAGTGAGTTCAAGAATCTTTA
PTPLB	protein tyrosine phosphatase-lik	8	109	CACGGCGTACCTGGTCATCTA	CAGCCAAGAAATAGTTTGGTA	TACGCTTAACTTTCTATGCAT	TCCTATGTTAATTTCCACCAA
PTPN1	protein tyrosine phosphatase, n	25	55	CACGTGGGTATTTAATAAGAA	CAGGCATGCCGCGGTAGGTAA	CAGGAATAGGCATTTGCCTAA	ACGGACGTTGGTTCTGCACTA
PTPN11	protein tyrosine phosphatase, n	75	5	CAGAAGCACAGTACCGATTTA	CCGCTCATGACTATACGCTAA	GCGGTCCAGCATTATATTGAA	GCCGCTCATGACTATACGCTA
PTPN12	protein tyrosine phosphatase, n	50	17	AAGCTTAATGAGGAAATATCA	TTGCAGGTTATCAGAGATCAA	CTGCTTGTAGACATGTTAATA	GTGGATCATGATAACACTTCA
PTPN13	protein tyrosine phosphatase, n	83	4	CGGTCTATTCTTACTAAGAAA	TCCAGGTACATTAAAGATGAA	TCGATGGATAAGTATCATATA	AACCTTTGGATCAGTGTCTAA
PTPN14	protein tyrosine phosphatase, n	58	11	AAGGGCGATTACGATGTACAT	CGGTGTGGCATTTACAATATA	CTGGCCCAAACTAGGTTCAAA	TCGGTGGAAAGCACAGGGCAA
PTPN18	protein tyrosine phosphatase, n	69	6	CAGGCAGACATCAGTCCACAT	CCCAATGACTGTAGCATTCAA	GTGGGCCTGGATCAAAGTTAA	CCGGGTGTAAGTCTAACGCCA
PTPN2	protein tyrosine phosphatase, n	0	157	AACTGTATTCATACATGTCAA	CCGCTGTACTTGGAAATTCGA	TCGATTGAATTGTACTGGATA	CACAAAGGAGTTACATCTTAA
PTPN21	protein tyrosine phosphatase, n	8	110	GAGGAGACCATTCAATTTCAA	GTGCATAGATTTCTATCTTAA	AAGCACCTCCTTACCGGGCAA	CCCACCGCAGTTGCACTATAA
PTPN22	protein tyrosine phosphatase, n	8	111	CCGGGTAGAACTATCCCTGAT	TGGGATGTACGTTGTTACCAA	CCCAGGGTCCTTTATCTACAA	TACGTAATGCCTCTAATGTAA
PTPN23	protein tyrosine phosphatase, n	-25	192	AACCTTGTACAGTCCATGCAA	CCGCCAGATCCTTACGCTCAA	CTGCGTGAGCTTATCCAGAAA	CCGGCCCGACACTGTCAGGAA
PTPN3	protein tyrosine phosphatase, n	8	112	CAGGTTATTCAGCGATAGTTA	CCGGGTATTATTGCAGGGAAA	CCGAGAAATGCTGGTCACAAA	CCGCTCATTTGCTGACTTCAA
PTPN4	protein tyrosine phosphatase, n	67	8	CTCCGAACAAATAGTAAATAA	TCCGTCATCAACACAAGCTAA	CTCCGTCATCAACACAAGCTA	AGCACGTACCTTAGAACTCTA
PTPN5	protein tyrosine phosphatase, n	0	158	ATCGAGGAGATGAACGAGAAA	CACCAACATCGAGGAGATGAA	CAGCTGAGGGAGAGTTCTCTA	CCCTCTGAGTTCCTACATCAA
PTPN6	protein tyrosine phosphatase, n	25	56	CCGGAACAAATGCGTCCCATA	TAGGCCCTGATGAGAACGCTA	CCGCACCTCGTCCAAACACAA	CCAGTTCATTGAAACCACTAA
PTPN7	protein tyrosine phosphatase, n	-50	203	CAGGTCTACCTCAGGACTGAA	CTGGCATTTATGACAGACAAA	AAGCTCCAGAACAGTAACCAA	CACCCATGTGTCATAAGAGTA
PTPN9	protein tyrosine phosphatase, n	0	159	ACCAAACTAGAGTGAAGCTAA	AGGAACGGAGCGAATAATATA	CCAGTAGCAATGTGTTCTTAA	CAAGTGGACAGTTCAGTACAA
PTPNS1	protein tyrosine phosphatase, n	0	160	CGCCTGTAAATTACTGAGAAA	CTCGCTGTGGACGCCTGTAAA	ACGCCTGTAAATTACTGAGAA	CCCGAGAAGAATGCCAGAGAA

PTPNS1L2	protein tyrosine phosphatase, n	0	161	CAGGGCCAAACCGGAAATTAA	CCGGAAATTAATCTACAATTT	AAGGTAACTTTCCCAGAGTAA	AAGCTCCAGGTTTCACCACAA
PTPRA	protein tyrosine phosphatase, r	42	26	CAGAGTGATCATTCCAGTTAA	CCGGAGAATGGCAGACGACAA	CAGGTGTAGGGCGTACAGGTA	AGGCATTACAATTTCACCAAA
PTPRB	protein tyrosine phosphatase, r	8	113	CCCGGAGATGTGGATAACTAT	CCGGTCGACTTTATCAAGTTA	TCGGGTGTATCAGACTAATTA	CCAGTATTAGTGGAGACTTAA
PTPRC	protein tyrosine phosphatase, r	8	114	AACCGTTATGTTGACATTCTT	AAGAATTGCGATTTCCGTGTA	TCGATTATTCCCTGTACAATA	CAACTTCTTTGTAATCGTTAT
PTPRD	protein tyrosine phosphatase, r	-17	187	ACGGCCAGTCCCGAACAGTAA	CTGGGTGTCATTGAAGCAATA	CGCCTTGTTAATATTATGCCA	ATGGCATTATCACCAAGTATA
PTPRE	protein tyrosine phosphatase, r	25	57	ACCACGGGCAATTAAACTTTA	CCGAGTGATCCTTTCCATGAA	CAGTGAATTCACAACCCTGAA	GACCATCGTCATGTTAACAAA
PTPRF	protein tyrosine phosphatase, r	0	162	CAGCGCTATCTAGATAGGTAA	CATCGTGTTTGCAAAGGTTAA	CCGAGGACTATGAAACCACTA	CAGGAGCGGATCATCATGTAT
PTPRG	protein tyrosine phosphatase, r	25	58	AGGGTGAAGTTAAGACCTTTA	TCGGTGAGCTCTATTCTAATA	TAGGCACTGTTCAATACTGTA	CAGACTCTAGGTTATACAATA
PTPRH	protein tyrosine phosphatase, r	0	163	CCGGGACGTTGTACAATTTCA	CCGGGTCATTGTATACGTGTT	CAGGTACTGACATCACCCTAA	TCGAAGCACAGCACACACTAA
PTPRJ	protein tyrosine phosphatase, r	33	38	TCCGAGTATGTCTACCATTTA	TCGGGTAGAAATAACCACCAA	ACGAGTCGTCATCTAACTATA	ACCCGTATCTTCTACAATCAA
PTPRK	protein tyrosine phosphatase, r	25	59	CCGGGTTAAATGCTATAAATA	CTGGAGATTAGTGTATGATTA	CCGGCGAGTCAAGTTATCAAA	CAGGATTTGTATCGCTGTGTA
PTPRM	protein tyrosine phosphatase, r	8	115	AAGGGTCAAATGCTGCAAATA	CACATCCGTAGTTATGCTAAA	CAGGATATTCCGCATTTACAA	CACCTTTGAATCAAACTGACA
PTPRN	protein tyrosine phosphatase, r	8	116	CACCCTTCACTGAGTTACGAA	CAGGTCTGGCTTGGCACCCAA	CAGGAAGGTGAACAAGTGCTA	CTGGTGAAGTCTGAACTGGAA
PTPRN2	protein tyrosine phosphatase, r	25	60	AAGGTGCTAAAGAGATTGATA	CAGCGCAGTTTAGCAGTTAAA	AGCGGACAGAATGATGCCAAA	ACGGATGTTGTCAGGAATCAT
PTPRR	protein tyrosine phosphatase, r	17	83	CGCCACCAGATTGTCAATTCA	TCGCCTCATTGGAAAGAAGAA	TAGGTTTATCACACAGCCTAA	AACCCTTTGTGTCTATACCAA
PTPRS	protein tyrosine phosphatase, r	100	1	CACGGCATCAGGCGTGCACAA	CGCGTCTACTACACCATGGAA	CAGGACATTCTCTCTGCACAA	AAGAACAAACCCGACAGTAAA
PTPRV	protein tyrosine phosphatase, r	50	19	AACGCTGAAGCAGTATATCTA	AAGGTGGGCAGTCATGTCCAA	ATCCCTTTCCATGGGCATAAA	ATGCCACAGAGTGGACCTATA
PTPRZ1	protein tyrosine phosphatase, r	42	27	ACGCTGGAATTTGGTAGTGAA	TAGCCATATACCAATACCTAA	CCGCCAAATTTATATCATTAA	CAGACTAATTACACTGAGATA
RNGTT	RNA guanylyltransferase and 5	33	39	CAGGGTTGTTAAGTTGTACTA	CGGGATTTCTATATGGACATA	TACCATCTGCAGTATTATAAA	ATGGATTTAAAGGGCGGCTAA
SBF1	SET binding factor 1	0	164	CAGCGCCGAGCTCTTCCGTAA	CCGCGTGGTGTGGCCCTGTTA	TCCGGTCGTTACCGACCACTA	GACGCCTGTGTTCCACAATTA
SGPP1	sphingosine-1-phosphate phos	0	165	AGAGATTAACTTTCCATATAA	ATCGGTATATTACCTATGGAA	CTGCCATTACCTTTCATGTTA	TGCGTAATTACTAGACCAGAA
SKIP	skeletal muscle and kidney enri	-33	197	CAGCCAAGTGTCGTCCACATA	CTGGAATTAGCCGCTTAAATA	CACGTTCGACTTGGAGCTGAA	ACGGTCGGAGTCCGGAAGAAA
SNAP23	synaptosomal-associated prote	0	166	CTGGCAAGGCTTATAAGACAA	CAGGCCTATTAACATCATACA	TACCACATGAATTCAGATTTA	AAGAGGTTGTTACCTCAGTAA
SPAP1	SH2 domain containing phosph	42	28	TCAGAAGATGGCTTACCATAA	TTCAAATATAGTAAAGATAAA	CAGGACCTGATGGCTATAGAA	ATGCCGGCAAATATTACTGTA
TA-PP2C	T-cell activation protein phosph	17	84	AAAGGGATGGTACAAGTCTAA	CACAAATTGTACGTAATGATA	CCCTCAAAGCCTAGAAATTTA	CTCAATTCTCAGGGACTTTAA
TENC1	tensin like C1 domain containin	-8	175	ACAGCACGTGGTCGTACTATA	CAAGGTGGCGACGCACAGAAA	ACGGCCATCCTAGATGACGAA	CTCGGTCTCTGTCGACTACAA
TPTE	transmembrane phosphatase w	25	61	CAGATTGGCAACCAAGACTAA	CTGAAATATGTTCAACTGCAA	TCGGTACTTGATAACATTACA	CAGACTTGTGTTATTCTAGCA
TPTE2	transmembrane phosphoinositi	25	62	ACCTGGAGAACTGATAATAAA	CTGATAATAAATTGTGGTTTA	ACAGGCAAATTTCAGAAACAA	AATGATTGAAATAGAGCTATA

Table S1. siRNA-mediated knockdown of human phosphatase genes alters cellular PI(3)P. U2OS-EGFP-2xFYVE cells were transfected with siRNAs targeting human phosphatase genes for 48 h (4 siRNA sequences per gene per well; all four sequences displayed). Following knockdown, EGFP-2xFYVE signal and distribution was visualized by confocal microscopy and scored from -100 (decreased punctae from control cells) to +100 (increased punctae) and means determined. Select genes were validated using multiple unique siRNA sequences and their efficacy was incorporated into their scores (see *Methods*). Genes were ranked based on their scores from 1 (most increased EGFP-2xFYVE) to 206 (most decreased).

Journal of proteome research
Article
pubs.acs.org/jpr

Characterization of Differential Protein Tethering at the Plasma Membrane in Response to Epidermal Growth Factor Signaling

Brendan D. Looyenga* and Jeffrey P. MacKeigan*

Laboratory of Systems Biology, Van Andel Research Institute, Grand Rapids, Michigan 49503, United States

Supporting Information

ABSTRACT: Physical tethering of membrane proteins to the cortical actin cytoskeleton provides functional organization to the plasma membrane and contributes to diverse cellular processes including cell signaling, vesicular trafficking, endocytosis, and migration. For these processes to occur, membrane protein tethering must be dynamically regulated in response to environmental cues. In this study, we describe a novel biochemical scheme for isolating the complement of plasma membrane proteins that are physically tethered to the actin cytoskeleton. We utilized this method in combination with tandem liquid chromatography/mass spectrometry (LC–MS/MS) to demonstrate that cytoskeletal tethering of membrane proteins is acutely regulated by epidermal growth factor (EGF) in normal human kidney (HK2) cells. Our results indicate that several proteins known to be involved in EGF signaling, as well as other proteins not traditionally associated with this pathway, are tethered to the cytoskeleton in dynamic fashion. Further analysis of one hit from our proteomic survey, the receptor phosphotyrosine phosphatase PTPRS, revealed a correlation between cytoskeletal tethering and endosomal trafficking in response to EGF. This finding parallels previous indications that PTPRS is involved in the desensitization of EGFR and provides a potential mechanism to coordinate localization of these two membrane proteins in the same compartment upon EGFR activation.

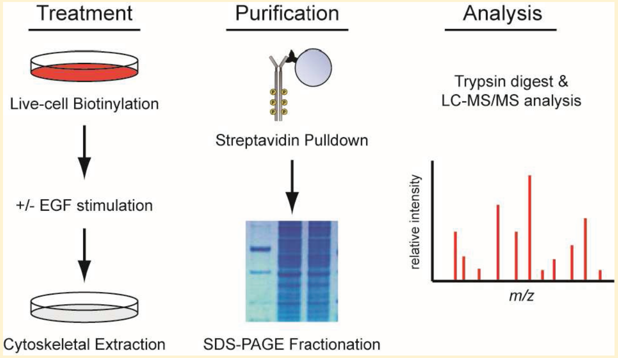

KEYWORDS: *tethering, actin cytoskeleton, EGFR, proteomics, mass spectrometry, PTPRS*

INTRODUCTION

The transmembrane proteome comprises a diverse collection of proteins involved in myriad cellular functions including nutrient transport, adhesion, cellular motility, metabolism, and cell signaling. These functions are regulated by an equally diverse array of mechanisms that include post-translational modification, endocytosis, and oligomerization/aggregation within the membrane. All of these regulatory mechanisms involve interactions of transmembrane proteins with the underlying cortical actin cytoskeleton, which both organizes and stabilizes the membrane proteome into distinct functional domains.[1]

Interactions between transmembrane proteins and the actin cytoskeleton can be classified as passive or active.[2] Passive interactions involve cytoskeleton-mediated organization of the membrane into distinct "corrals", which primarily serve to limit lateral diffusion of proteins within the lipid bilayer.[3] Active interactions, on the other hand, involve physical tethering of transmembrane proteins to cortical actin filaments (F-actin).[4] While active tethering similarly limits the lateral mobility of transmembrane proteins, it is also critical for the maintenance of cell–cell contacts and membrane microdomains, such as lipid rafts and focal adhesions, and for vesicular trafficking at the cell surface.[5]

Active tethering of transmembrane proteins is facilitated either by direct interactions of proteins with F-actin or, more commonly, by adaptor proteins that link the cytoplasmic domains of transmembrane proteins to F-actin. Adaptor proteins involved in cytoskeletal tethering interact with distinct sets of substrates within the membrane proteome, allowing for coordinated tethering of multiple transmembrane proteins in response to signals that govern adaptor protein abundance or activity.[6] Temporal and spatial coordination of transmembrane protein tethering by adaptor proteins clearly plays an important role in complex cellular processes such as signal transduction, though the mechanisms by which the relatively limited set of adaptor proteins, which include proteins of the ezrin–radixin–moesin (ERM) family, are directed to specific membrane complexes is incompletely understood.[6a]

Cytoskeletal tethering plays in important role in both the positive and negative regulation of epidermal growth factor receptor (EGFR), depending on which adaptor protein is involved in the process.[6c] Tethering by ERM proteins mediates efficient internalization and endocytic sorting of activated EGFR, which is required for endosomal signaling to various EGFR effectors and also mediates receptor downregulation.[7] Conversely, interaction of EGFR with merlin, a closely related FERM family protein that cannot interact with F-actin,

Received: October 28, 2011
Published: May 5, 2012

sequesters EGFR into an insoluble membrane compartment from which it cannot signal or become internalized.[8] Loss of EP50, another protein involved in tethering complexes, disturbs both of these processes, leading to accumulation of activated EGFR on the cell surface due to defects in receptor-mediated endocytosis.[7b] Together these studies point out both the complexity and importance of cytoskeletal tethering to growth factor signaling from the cell surface.

While it is clear that ligand-mediated activation of EGFR promotes its tethering to the cytoskeleton, it is less obvious whether signaling through this receptor also promotes the tethering of other proteins associated with endocytosis and signal transduction to downstream effectors. To answer this question, we devised an unbiased proteomic strategy to globally evaluate composition of the tethered membrane proteome before and after stimulation of cells with EGF. In this approach, adherent cells are first surface biotinylated using an amine-reactive cross-linking reagent and then extracted with detergents to remove soluble cytoplasmic and membrane proteins. The remaining insoluble/cytoskeletal fraction is then homogenized, affinity purified with streptavidin beads, and analyzed by mass spectrometry. Though aspects of this approach have been previously utilized to isolate specific protein pools of membrane proteins for proteomic analysis, the combination of membrane biotinylation and cytoskeletal extraction we describe has not been previously applied to differential protein tethering to the cytoskeleton.[9]

Quantitative comparison of the "membrane tetherome" before and after EGF stimulation suggests that EGFR activation leads to the association of several different proteins with the cytoskeleton, including those involved in signal transduction and vesicular trafficking. At the same time, EGFR signaling also promotes the dissociation of another subset of proteins from the cytoskeleton, including those that mediate cytoskeletal dynamics and RNA processing. This experimental approach provides a relatively simple means to identify and quantify components of the tethered membrane proteome and will allow us to decipher how specific plasma membrane complexes are organized by the underlying cortical cytoskeleton in response to different environmental or signaling conditions.

■ EXPERIMENTAL SECTION

Cell Culture

HK2 normal human renal epithelial cells were obtained from ATCC. Cells were grown in normal tissue culture-treated dishes in antibiotic-free RPMI-1640 media (Invitrogen, Carlsbad, CA) containing 10% fetal bovine serum (FBS) under standard growth conditions of 37 °C and 5% CO_2. Cells were passaged at 85–90% confluency every 3–4 days to maintain continuous logarithmic growth. Treatments with recombinant EGF were performed in basal RPMI-1640 media after 16–20 h of serum starvation. Treatment with methyl-beta-cyclodextrin (MβCD) was performed at 5 mM concentration for 30 min to disrupt lipid raft microdomains in the plasma membrane.

Adenoviral Expression of PTPRS

Recombinant adenoviral vectors containing PTPRS were generated by recombining the full-length open reading frame of PTPRS into pAd/CMV/V5-DEST using the GATEWAY cloning system (Invitrogen). Adenoviral particles were produced by transfecting this vector into the 293A packaging line, harvesting a crude viral lysate and amplifying the stock by one additional round of infection in 293A cells. The resulting viral supernatant was titered and frozen prior to further use. HK2 cells plated to 6 cm plates and glass coverslips were infected at a multiplicity of infection (MOI) of 5 for 24 h prior to media change. At 32–48 h after infection, the cells were stimulated with EGF and analyzed by immunoblot or immunofluorescent staining.

Antibodies

Antibodies for EGFR, ERM, CD44, Grb2, clathrin, pEGFR^{Y1068}, pERM^{T567}, and actin were obtained from Cell Signaling Technologies (Danvers, MA). The mouse monoclonal antibody to tubulin was obtained from Sigma-Aldrich (St. Louis, MO), and the rabbit polyclonal antibody to 14-3-3 epsilon was obtained from Epitomics (Burlingame, CA). The mouse monoclonal antibody to EEA1 was purchased from BD Biosciences (San Diego, CA). The mouse monoclonal antibody to PTPRS was kindly provided by Dr. Michel Tremblay (McGill University, Montreal, Quebec, Canada).

Immunofluorescent Staining and Microscopy

HK2 cells were seeded to coverslips and allowed to adhere for 24 h. Cells were then starved overnight in serum-free RPMI-1640 media prior to treatment with recombinant human EGF (100 ng/mL) for the indicated times. For imaging of total protein content, cells were fixed with 3.7% formaldehyde in phosphate-buffered saline (PBS) and permeabilized with 0.2% TritonX-100 in PBS. Imaging of the cytoskeletal fraction only was performed by treating cells with solublization buffer (10 mM PIPES, 50 mM KCl, 20 mM EGTA, 3 mM $MgCl_2$, 2 M glycerol, 2 mM NaF, 2 mM $Na_3(VO)_4$, 1% TritonX-100) supplemented with 1× protease inhibitor cocktail (Sigma) on ice for 5 min, followed by fixation with formaldehyde as above. After blocking with 5% normal goat serum and 3% bovine serum albumin in PBS, the coverslips were incubated at 4 °C overnight with anti-EGFR (1:100), anti-EEA1 (1:200), or anti-PTPRS (1:150) diluted in block buffer. After washing in PBS/0.02% TritonX-100, coverslips were incubated for one hour with AlexaFluor-488 or AlexaFluor-546 coupled secondary antibodies (Invitrogen). After a final round of washing, cells were costained with DAPI to detect nuclei, and coverslips were mounted on glass slides with antifade gel mounting medium. Images were obtained using a Nikon Ti-E inverted fluorescence microscope equipped with DAPI, FITC, and Texas Red filter sets and processed using the NIS Elements software package (Nikon Instruments, Melville, NY).

Cytoskeletal Fractionation

HK2 cells were plated to 6-well dishes (35 mm diameter) at a density of 1.5 × 10^5 cells per well and allowed to adhere overnight in complete media. Cells were then starved overnight in serum-free RPMI-1640 media prior to treatment with recombinant human EGF (100 ng/mL) for the indicated times. Cell lysates were fractionated according to previously described methods.[9c] Briefly, cells were first washed on ice and then incubated with ice-cold solublization buffer (10 mM PIPES, 50 mM KCl, 20 mM EGTA, 3 mM $MgCl_2$, 2 M glycerol, 2 mM NaF, 2 mM $Na_3(VO)_4$, 1% TritonX-100) supplemented with 1× protease inhibitor cocktail (Sigma) on ice for 5 min with gentle rocking. The soluble fraction was removed to a fresh tube on ice, and the remaining insoluble material was washed twice with cold detergent-free solublization buffer to remove any remaining soluble protein. The cytoskeletal fraction was then scraped into extraction buffer (25 mM Tris-HCl, 300 mM

NaCl, 30 mM $MgCl_2$, 2 mM NaF, 2 mM $Na_3(VO)_4$, 1% NP-40, 0.2% Brij35, 0.2% sodium deoxycholate, 2 mM dithiothreitol) supplemented with 1× protease inhibitor cocktail (Sigma) and sheared ten times through a 27 gauge needle to homogenize the cytoskeletal proteins. Equal volumes of protein lysate were diluted with Laemmli buffer and denatured by boiling for immunoblot analysis.

Immunoblotting

Protein samples were separated on Tris-glycine polyacrylamide gels and transferred overnight to nitrocellulose membranes in a wet transfer apparatus (Hoefer, Holliston, MA). Membranes were blocked in 3% nonfat dry milk in Tris-buffered saline/0.1% Tween (TBS-T) and probed with primary antibodies overnight at 4 °C. After washing in TBS-T buffer and incubation with a horseradish peroxidase-coupled secondary antibody, membranes were incubated in enhanced chemiluminescent reagent, exposed to film, and developed for signal using a X-omat film processor (Kodak, Rochester, NY).

Surface Protein Purification

HK2 cells were plated to eight 15 cm dishes at a density of 3.0×10^6 cells per plate and allowed to adhere overnight in complete media. Cells were then starved overnight in serum-free RPMI-1640 media prior to biotinylation on ice for 30 min with 0.25 mg/mL (0.41 mM) sulfo-NHS-SS-biotin (Thermo/Pierce, Rockford, IL). After the surface biotinylation reaction was quenched with 50 mM glycine, cells were washed twice with cold RPMI-1640 media and treated with or without recombinant human EGF (100 ng/mL) in prewarmed RPMI-1640 media for 5 min. Four dishes of cells were used for each condition (± EGF). Fractionation of the cells was performed as above, except that the Extraction Buffer did not contain DTT in order to maintain the biotin cross-links. After removal of insoluble debris by centrifugation for 10 min at 10000g, cytoskeletal fraction lysates were quantified by Bradford assay, and equal amounts of protein (4 mg) were incubated with pre-equilibrated neutravidin beads (Thermo/Pierce) overnight at 4 °C with constant rotation. Beads were pelleted at 200g for 1 min and washed twice with DTT-free extraction buffer and twice with Tris-buffered saline (TBS) containing 5% glycerol. Bound proteins were eluted from the beads by incubating with TBS/5% glycerol buffer containing 50 mM DTT for 2 h at room temperature with constant agitation. The final eluate was stored at −80 °C until analysis by immunoblot and LC−MS/MS.

Mass Spectrometry and Protein Identification

Tether enriched samples were quantified using Qubit fluorometry (Invitrogen). For each sample (purified fractions ± EGF), 20 μg of purified eluate was separated on a 4−12% Bis Tris NuPage gel (Invitrogen) in the MOPS buffer system. The 20 μg gel lane was excised into 20 equally sized segments, and gel pieces were processed using a ProGest robot (DigiLab, Holliston, MA). The trypsin digestion protocol involved washing the gel pieces with 25 mM ammonium bicarbonate followed by acetonitrile, reduction with 10 mM DTT at 60 °C followed by alkylation with 50 mM iodoacetamide (IA) at RT. Reduced and alkylated samples were digested with sequencing grade trypsin (Promega, Madison, WI) at 37 °C for 4 h. The digestion was quenched with formic acid, and the supernatant was analyzed directly by LC−MS/MS without further processing.

LC−MS/MS analysis was performed with a NanoAcquity HPLC system (Waters, Milford, MA) interfaced to a LTQ Orbitrap Velos mass spectrometer (ThermoFisher, Waltham, MA). Peptides were loaded on a trapping column and eluted over a 75 μm analytical column at 350 nL/min; both columns were packed with Jupiter Proteo resin (Phenomenex, Torrance, CA). The mobile phases consisted of HPLC grade H_2O (A) and HPLC grade acetonitrile (B), both containing 0.1% (v/v) formic acid. The gradient started at 2% B, reached 50% B in 18 min, 80% B in the next 0.5 min, and 98% A in the final 1 min (see Supporting Information Table S3 for HPLC gradient details). The mass spectrometer was operated in data-dependent mode, with MS performed in the Orbitrap at 60 000 fwhm resolution and MS/MS performed in the LTQ. The 15 most abundant ions were selected for MS/MS. Charge state deconvolution and deisotoping were not performed.

Peptide fragmentation data were searched using a local copy of Mascot (Matrix, Boston, MA). Mascot was configured to search the SwissProt database (human, 41016 entries) assuming the digestion enzyme trypsin was used. Searches were performed with a fragment ion mass tolerance of 0.80 Da and a parent ion tolerance of 10.0 PPM. Carbamidomethylation of cysteine was specified in Mascot as a fixed modification. Gln → pyro-Glu of the n-terminus, deamidated of asparagine and glutamine, oxidation of methionine, acetyl of the n-terminus, and CAMthiopropanoyl of lysine and the n-terminus were specified in Mascot as variable modifications. CAMthiopropanoyl modifications were included to account for changes to peptide mass that result from biotinylation with NHS-SS-biotin.[10] Data were searched with a maxiumum of 2 missed cleavage events allowed.

The resulting Mascot DAT files were parsed into the Scaffold v3.2 software package (Proteome Software Inc., Portland, OR) to validate MS/MS-based peptide and protein identifications. Peptide identifications were accepted if they could be established at greater than 95.0% probability as specified by the Peptide Prophet algorithm.[11] Protein probabilities were assigned by the Protein Prophet algorithm and were accepted if they could be established at greater than 99.0% probability and contained at least 4 identified peptides.[12] Proteins that contained similar peptides and could not be differentiated on the basis of MS/MS analysis alone were grouped to satisfy the principles of parsimony. Quantification of protein abundance was performed using the label-free spectral counting method as previously described.[13] The quantitative value assigned by Scaffold represents a normalized spectral count. Normalization was performed by calculating the average number of spectral counts for all samples and then multiplying the spectral counts in each individual sample by the average divided by the individual sample's sum.

■ RESULTS

EGF Stimulation Causes Redistribution of EGFR to the Cytoskeleton

To demonstrate that EGF promotes the tethering of its receptor to the cytoskeleton, we treated immortalized human renal epithelial cells (HK2) with recombinant EGF (100 ng/mL) for different times and then stained formaldehyde-fixed cells for EGFR before and after extraction of the membrane and cytosol. In the absence of EGF stimulation, cells fixed with formaldehyde display diffuse EGFR staining across the entire cell surface with a mild concentration in the perinuclear region

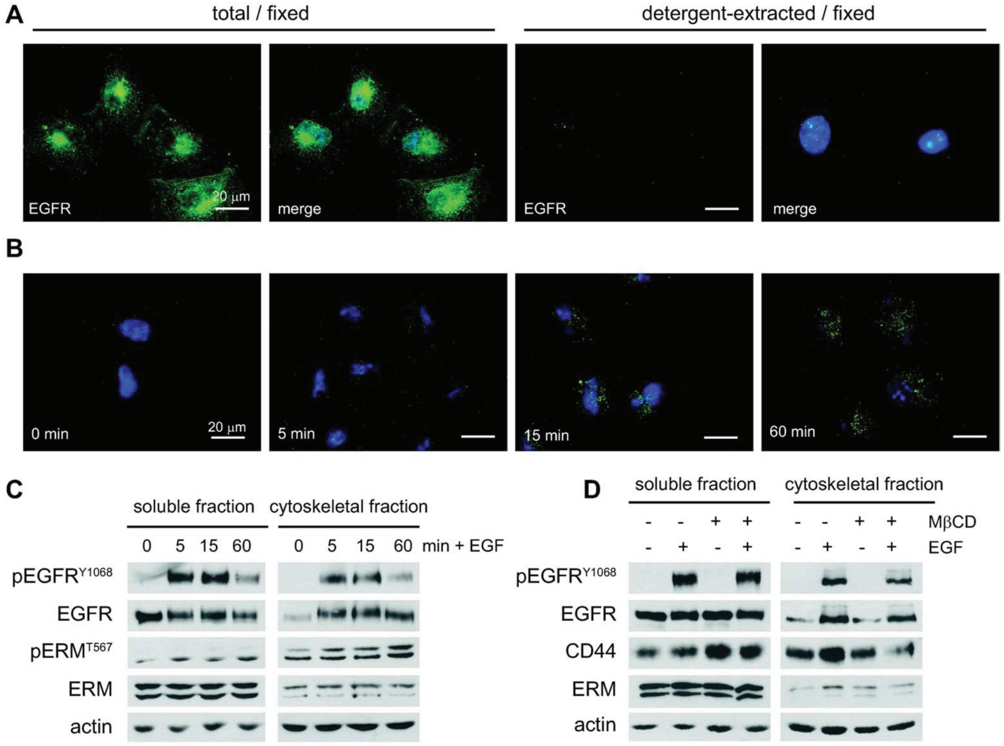

Figure 1. The epidermal growth factor receptor associates with the detergent-insoluble cytoskeletal fraction upon activation by its ligand. (A) HK2 cells were plated to glass coverslips and serum-starved for 24 h. They were then either fixed directly or extracted with buffer containing 1% TritonX-100 prior to fixation. Cells were labeled with antibodies to EGFR and detected with AlexaFluor-488 coupled secondary antibody (green) and also costained with Hoescht stain (blue) to detect nuclei. Images were captured using an epifluorescent inverted microscope at 60× magnification. Scale bars indicate 20 μm. (B) HK2 cells were cultured and serum-starved as before, then treated for the indicated time with 100 ng/mL of recombinant human EGF prior to detergent extraction and fixation. The remaining cytoskeletal fraction was stained for EGFR as before to demonstrate the progressive tethering of activated receptor to the cytoskeleton. Images are shown at 60× magnification with inset bars indicating 20 μm. (C) HK2 cells were plated at fixed density, serum-starved, and then stimulated for the indicated time with 100 ng/mL of recombinant human EGF. Cells were then biochemically fractionated, and lysates were analyzed by immunoblot for the indicated total or phosphorylated proteins. (D) HK2 cells were plated at fixed density, serum-starved, and pretreated with 5 mM MβCD prior to stimulation for 5 min ±100 ng/mL of recombinant human EGF. Cells were fractionated and analyzed by immunoblot as in C.

(Figure 1A). This entire population of receptors is completely removed by detergent extraction prior to fixation, indicating that EGFR is not tethered to the cytoskeleton in the inactive state (Figure 1A).[4a] Treatment of HK2 cells with EGF leads to a rapid (0−5 min) redistribution of EGFR into dense aggregates that progressively concentrate in the perinuclear region, consistent with receptor internalization and trafficking to the endosomal compartment (Figure 1B).[14] At the same time, receptors progressively associate with the cytoskeletal fraction and become visible by immunostaining in detergent-extracted cells (Figure 1B). Costaining of HK2 cells with antibodies for EGFR and the early endosomal marker EEA1 clearly demonstrates that EGFR localizes to endosomes upon activation by EGF, though tethering to the cytoskeleton is not a general property of all endosomal proteins, as EEA1 is not retained in the cytoskeletal fraction after detergent extraction (Supporting Information Figure S1).

Redistribution of activated EGFR to the cytoskeletal fraction can also be demonstrated by biochemical separation of HK2 cells into detergent-soluble and -insoluble fractions.[9c] Prior to EGF stimulation, EGFR is primarily detected in the detergent-soluble fraction of HK2 cells. EGF stimulation causes a rapid (0−5 min) increase in EGFR concentration in the insoluble cytoskeletal fraction, which is sustained with receptor activation (Figure 1C). Concentrations of EGFR in both soluble and cytoskeletal fractions decrease in parallel by 60 min poststimulation because of receptor degradation. The identities of the detergent-soluble and insoluble fractions are indicated by probing HK2 protein lysates for activated ezrin−radixin−moesin (ERM) family proteins, which are directly tethered to the actin cytoskeleton when phosphorylated at the C-terminus (pERM^{T567}). While ERM proteins can be detected in both soluble and insoluble fractions, the activated/phosphorylated form is highly enriched in the insoluble fraction (Figure 1C). Similarly, actin itself is also enriched in the cytoskeletal fraction.

The detergent extraction method we used to fractionate HK2 cells is similar, albeit not identical, to procedures used in lipid raft microdomain isolation.[9a,15] To demonstrate that redistribution of EGFR to a detergent-insoluble fraction after binding to EGF is a result of cytoskeletal tethering and not lipid raft aggregation, we pretreated HK2 cells for 30 min with 5 μM methyl-beta-cyclodextrin (MβCD) prior to stimulation with EGF. Treatment of cells with this reagent depletes cholesterol from the plasma membrane and thereby disrupts lipid raft microdomains.[16] As expected, MβCD had little effect on the activation and redistribution of EGFR to the detergent-insoluble fraction upon EGF stimulation (Figure 1D). Conversely, MβCD treatment increased the detergent solubility of the raft-associated protein CD44 and decreased its association with the cytoskeleton upon EGF stimulation (Figure 1D).[17] Together these data confirm that EGF-mediated activation of EGFR results in its redistribution to the detergent-

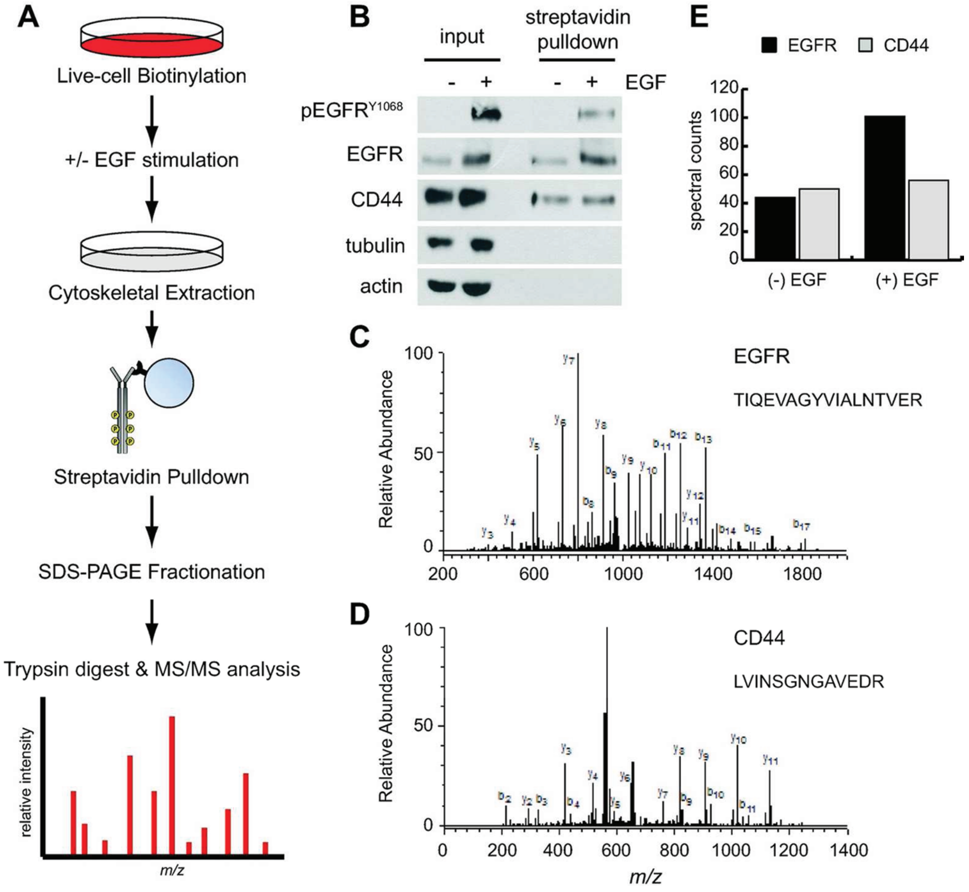

Figure 2. Proteomic workflow and experimental validation. (A) Flow diagram of the methods used to isolate and purify the fraction of membrane proteins associated with the cytoskeleton. See the Experimental Section for detailed procedures. (B) Cytoskeletal protein lysates isolated by the methods shown in A were analyzed be immunoblot before (input) and after purification with streptavidin beads (pulldown). Purification enriches for membrane proteins (EGFR and CD44) over intracellular cytoskeletal elements (tubulin and actin). (C) Annotated mass spectra for EGFR peptide (TIQEVAGYVIALNTVER) representative of the detection metrics for the peptides identified in this study. A minimum of two unique peptides with ≥50% probability (Prophet score) were used to identify each protein. (D) Annotated mass spectra for CD44 peptide (LVINSGNGAVEDR). (E) Quantification of relative EGFR (44/102 peptides) and CD44 (50/56 peptides) abundance in the cytoskeletal fraction of HK2 cells treated without (−) and with (+) EGF stimulation for 5 min using the label-free spectral counting method.

insoluble fraction and are consistent with EGFR being tethered to the actin cytoskeleton upon activation.

Biochemical Isolation and Purification of the Tethered Membrane Proteome

Regulated tethering of EGFR in HK2 cells provided us with a useful framework to validate a novel strategy for isolating and characterizing the tethered membrane proteome (Figure 2A). In this strategy, we combined the biochemical fractionation method described above with cell surface biotinylation, which was performed with sulfo-NHS-SS-biotin, a cell nonpermeable cross-linking reagent that adds a biotin tag to primary amines. This reagent can be applied to live cells in phosphate-buffered saline (PBS) to label the lysine residues of extracellular proteins. When labeling is performed at temperatures lower than 4 °C, vesicular trafficking to the cell surface is inhibited, thus ensuring that a stable population of biotinylated receptors is present when cells are experimentally stimulated. After stimulation and fractionation, the membrane protein component of the detergent-insoluble cytoskeletal fraction can be isolated by affinity purification over streptavidin beads and eluted by reduction of the biotin cross-link with dithiothreitol (DTT).

We validated the experimental scheme presented above by labeling HK2 cells with sulfo-NHS-SS-biotin for 30 min on ice and then allowing a 5 min recovery in prewarmed culture media in the presence or absence of EGF (100 ng/mL). Cells were then extracted with ice-cold detergent (TritonX-100) to remove the soluble/untethered protein fraction. The remaining cytoskeletal fraction was scraped into a second buffer containing a cocktail of detergents (NP40, deoxycholate and Brij-35) and homogenized by shearing the cytoskeletal fraction through a 25 gauge needle. Remaining debris was removed by centrifugation, and the resulting protein lysate was purified over streptavidin beads to isolate all membrane proteins associated with the cytoskeleton. Immunoblot analysis of the input and purified fractions clearly demonstrate enrichment of EGFR in the cytoskeletal fraction after EGF stimulation (Figure 2B). As controls for the reaction, we also probed lysates for CD44. As expected, CD44 was isolated with the purified membrane protein fraction, and was found to be associated with the cytoskeletal fraction independent of EGF stimulation (Figure 2B). Immunblot analysis of the streptavidin-purified fraction also reveals that even highly abundant cytoplasmic proteins from the cytoskeletal fraction, such as tubulin and actin, are largely excluded by purification of biotinylated membrane

Table 1. Proteins with Incresed Cytoskeletal Association upon EGF Stimulation[a]

			unique peptide		coverage (%)		spectral counts		quantitative value			
cell signaling	accession number[b]	gene	(−) EGF	(+) EGF	(−) EGF	(+) EGF	(−) EGF	(+) EGF	(−) EGF	(+) EGF	fold Δ	log Δ
Peptidyl-prolyl cis−trans isomerase B	P23284	PPIB	5	8	22.0	44.0	5	16	4.2	25.9	6.13	2.61
Cysteine and glycine-rich protein 2	Q16527	CSRP2	5	8	32.0	45.0	8	16	6.3	24.8	3.90	1.96
CD70 antigen	P32970	CD70	5	5	28.0	38.0	16	19	3.6	12.5	3.48	1.80
Gremlin-1	O60565	GREM1	7	8	37.0	49.0	29	39	21.6	66.6	3.09	1.63
Peroxiredoxin-1	Q06830	PRDX1	12	15	59.0	56.0	35	56	31.1	80.5	2.59	1.37
Guanine nucleotide-binding protein G(i) subunit alpha-2	P04899	GNAI2	8	13	26.0	43.0	13	22	7.1	17.6	2.48	1.31
14-3-3 protein epsilon	P62258	YWHAE	4	6	16.0	27.0	5	9	5.3	12.5	2.38	1.25
Epidermal growth factor receptor	P00533	EGFR	30	42	31.0	37.0	44	101	26.7	61.4	2.30	1.20
Prohibitin-2	Q99623	PHB2	11	13	33.0	40.0	18	27	12.6	28.7	2.28	1.19
Cytoplasmic FMR1-interacting protein 1	Q7L576	CYFP1	7	13	6.1	12.0	10	14	4.0	8.9	2.20	1.14
Peroxiredoxin-2	P32119	PRDX2	6	6	28.0	30.0	8	9	6.3	13.6	2.14	1.10
Receptor-type tyrosine-protein phosphatase S	Q13332	PTPRS	10	14	6.6	9.6	12	18	5.2	10.8	2.08	1.06
Vesicular Trafficking												
Ras-related protein Rab-10	P61026	RAB10	4	5	22.0	26.0	6	14	4.2	19.1	4.52	2.18
Dynein light chain 1	P63167	DYNLL1	6	5	65.0	64.0	12	20	22.3	54.4	2.44	1.29
Coatomer subunit alpha	P53621	COPA	11	20	9.8	18.0	13	21	6.5	13.3	2.05	1.04
ECM and Cytoskeletal Regulation												
Urokinase-type plasminogen activator	P00749	PLAU	6	10	13.0	19.0	11	16	2.2	6.1	2.76	1.47
Protein S100-A9	P06702	S100A9	4	7	45.0	53.0	12	25	22.3	53.0	2.38	1.25
Prolactin-inducible protein	P12273	PIP	5	6	44.0	44.0	17	30	9.9	23.1	2.33	1.22
Collagen alpha-1(XVIII) chain	P39060	COL18A1	6	9	5.8	7.7	15	23	3.7	8.2	2.21	1.15
Membrane Transport												
Voltage-dependent anion-selective channel protein 3	Q9Y277	VDAC3	4	9	16.0	44.0	8	14	4.5	15.3	3.40	1.77
Voltage-dependent anion-selective channel protein 2	P45880	VDAC2	12	12	52.0	56.0	21	32	15.3	32.3	2.12	1.08

[a] Proteins that were identified with confidence of >99% and were scored with ≥4 spectral counts (SpC) in both unstimulated and stimulated cells were sorted by the SpC ratio in stimulated/unstimulated cells. Refer to Table S1 (Supporting Information) for a complete list of proteins identified in this study. [b] Accession numbers were compiled from the SwissProt database.

proteins away from the rest of the cytoskeletal fraction (Figure 2B).

Quantitative Analysis of Tethered Membrane Proteome Composition

To identify the composition of the tethered membrane proteome, we performed label-free tandem mass spectrometry (MS/MS) on the streptavidin-purified fractions from HK2 cells treated in the presence or absence of EGF for 5 min. Because detection of unique peptides using label-free methods of quantification such as spectral counting can be confounded by large differences in protein abundance, we first separated individual samples by one-dimensional polyacrylamide gel electrophoresis and fractionated them into 20 separate gel slices by protein mass. Individual gel fractions were trypsin digested and separated by liquid chromatography interfaced directly with the mass spectrometer. The 15 most abundant ions for each peptide were selected for MS/MS analysis. Spectra for each peptide were matched to the Swissprot human database using a local copy of Mascot and parsed into the Scaffold software package to filter and simply identified hits into a nonredundant list of proteins for each sample.

Quantitative analysis of the MS/MS data was performed by analyzing spectral counts (SpC) of peptides mapped to unique proteins within the Swissprot database. Previous studies have shown that this method can accurately discriminate differences of abundance as low as 1.4-fold with 95% confidence providing that at least one of the two samples displays ≥4 SpC.[13] In our analysis of the data, we filtered out all proteins that produced a SpC <4 for either sample (± EGF) to ensure maximum confidence in protein identification (Supporting Information Tables S1 and S2). We then determined the SpC ratio of stimulated-to-unstimulated cells to distinguish positively identified proteins whose association with the cytoskeleton changed upon stimulation of cells with EGF. To ensure that these quantitative predictions from the MS/MS data accurately represent protein abundance, we compared the spectral count ratios of EGFR and CD44 in EGF-stimulated versus -unstimulated cells (Figure 2C−E). As previously demonstrated by immunoblot (Figure 2B), the amount of EGFR in the tethered membrane proteome increases upon EGF stimulation (44/101 SpC), whereas the amount of CD44 stays relatively constant under the same treatment conditions (50/56 SpC, Figure 2E).

Activation of EGFR by its ligand promotes its intrinsic tyrosine kinase activity and induces a variety of downstream signaling pathways associated with proliferation, survival, and migration. In addition, EGF signaling also engages the cellular machinery required for internalization and trafficking of activated receptors. Because the cytoskeleton is intimately involved in signaling and receptor-mediated endocytosis, we asked whether stimulation of HK2 cells with EGF altered the association of proteins beside EGFR into the cytoskeletal fraction. Analysis of normalized spectral count ratios between stimulated and unstimulated cells revealed that 12.2% (61/499)

Table 2. Proteins with Decresed Cytoskeletal Association upon EGF Stimulation[a]

			unique peptide		coverage (%)		spectral counts		quantitative value			
cell signaling	accession number[b]	gene	(−) EGF	(+) EGF	(−) EGF	(+) EGF	(−) EGF	(+) EGF	(−) EGF	(+) EGF	fold Δ	log Δ
Protein RRP5 homologue	Q14690	PDCD11	11	5	6.40	2.70	11	5	6.5	3.2	0.49	−1.04
Cyclin-dependent kinase inhibitor 2A, isoform 4	Q8N726	CDKN2A	6	5	43	28	13	7	27.3	9.7	0.35	−1.50
ECM and Cytoskeletal Regulation												
Desmoglein-1	Q02413	DSG1	13	13	16	11	29	18	12.6	6.3	0.50	−1.00
Plectin	Q15149	PLEC	65	21	14	3.50	84	27	48.7	18.0	0.37	−1.44
Filaggrin-2	Q5D862	FLG2	12	9	6.70	5.20	28	29	23.7	7.0	0.30	−1.76
Hornerin	Q86YZ3	HRNR	9	5	5.70	2.60	52	22	22.5	3.0	0.13	−2.92
Transcription and Chromatin Binding												
FACT complex subunit SPT16	Q9Y5B9	SSRP1	25	13	31	16	33	15	18.1	8.9	0.49	−1.02
DNA topoisomerase 2-alpha	P11388	TOP2A	11	7	11	8.40	13	7	14.4	7.0	0.49	−1.03
High mobility group protein HMGI-C	P52926	HMGA2	5	4	50	32	13	7	17.9	7.7	0.43	−1.21
Chromodomain-helicase-DNA-binding protein 4	Q14839	CHD4	37	18	23	11	46	21	27.5	11.5	0.42	−1.26
THO complex subunit 4	Q86V81	ALYREF	7	4	47	27	21	5	23.5	6.9	0.30	−1.76
DNA Replication												
Replication factor C subunit 1	P35251	RFC1	10	5	12	5.50	10	7	6.5	3.2	0.49	−1.03
Replication factor C subunit 2	P35250	RFC2	6	4	23	18	11	4	9.3	3.4	0.36	−1.47
RNA Binding/Processing												
Plasminogen activator inhibitor 1 RNA-binding protein	Q8NC51	SERBP1	12	7	33	21	13	7	7.5	3.8	0.50	−1.00
Nucleolar protein 6	Q9H6R4	UTP6	11	5	11	6.20	11	5	6.3	3.0	0.47	−1.08
Protein C22orf28	Q9Y3I0	C22orf28	8	6	21	13	13	6	6.9	2.7	0.39	−1.37
U4/U6 small nuclear ribonucleoprotein Prp3	O43395	PRPF3	11	4	22	6.10	13	4	6.7	2.3	0.35	−1.51
Nucleolar complex protein 3 homologue	Q8WTT2	NOC3L	13	7	19	5.40	16	9	8.3	2.9	0.35	−1.51
Small nuclear ribonucleoprotein F	P62306	SNRPF	4	4	49	49	38	24	151.2	49.7	0.33	−1.60
U1 small nuclear ribonucleoprotein 70 kDa	P08621	SNRNP70	11	4	28	12	17	6	9.0	2.7	0.30	−1.73

[a] Proteins that were identified with confidence of >99% and were scored with ≥ 4 spectral counts (SpC) in both unstimulated and stimulated cells were sorted by the SpC ratio in stimulated/unstimulated cells. Refer to Table S1 (Supporting Information) for a complete list of proteins identified in this study. [b] Accession numbers were compiled from the SwissProt database.

of proteins detected by MS/MS display a 2-fold or greater change in abundance in the purified cytoskeletal fraction (Tables 1 and 2, Supporting Information Table S1). This list revealed the differential redistribution of several different protein classes expected to function downstream of EGFR including those involved in cell signaling, cytoskeletal regulation, migration, and proteolysis. Interestingly, many of the proteins identified in this analysis are functionally associated with RNA binding/processing and translation (Table 2). While neither of these cellular functions is obviously associated with cytoskeletal regulation or EGFR signaling, they have been connected to cellular spreading and adhesion, which are modulated by EGF in HK2 cells.[18] In addition, one of the RNA processing factors we found to be differentially tethered in response to EGF, small nuclear ribonucleoprotein F (SNRPF), has been previously shown to bind directly to the EGFR effector Grb2, which was also differentially tethered in our study (Figure 3A).[19]

EGF Signaling Promotes Cytoskeletal Association and Processing of PTPRS

To ensure that the findings from our MS/MS analysis accurately represent redistribution of proteins to the cytoskeleton, we performed immunoblot analysis on three of the differentially detected proteins in the soluble and cytoskeletal fractions of EGF-stimulated HK2 cells. Consistent with the MS/MS quantification, we found that the EGFR-associated adaptor proteins Grb2 and 14-3-3 epsilon increase in the cytoskeletal fraction of EGF-stimulated cells along with EGFR (Figure 3A). We also observed that the type-S receptor phosphotyrosine phosphatase (PTPRS) increased in association with the cytoskeleton upon EGFR activation, which is intriguing since a recent study has implicated this protein as a tumor suppressor and negative regulator of EGFR.[20] The temporal increase in association of PTPRS with the cytoskeleton also correlates with its proteolytic processing, as full-length receptor is increased in the cytoskeletal fraction at 5 min after EGF stimulation, whereas the processed intracellular domain is increased at 15 min after EGF stimulation (Figure 3A). By 60 min poststimulation, levels of both isoforms return to basal levels of abundance within the cytoskeletal fraction. Similar results are achieved with overexpression of full-length recombinant PTPRS in HK2 cells (Figure 3B).

Consistent with previous data, we observed that overexpression of PTPRS in HK2 cells using an adenoviral vector dampened basal EGFR phosphorylation and weakly antagonized EGF-induced activation of EGFR (Supporting Information Figure S3A).[20] Together with the coordinate increase in cytoskeletal association, these data suggest that PTPRS may localize to the same detergent-insoluble endocytic compartment that EGFR resides in upon EGF stimulation. To test this hypothesis, we immunofluorescently labeled HK2 cells over-

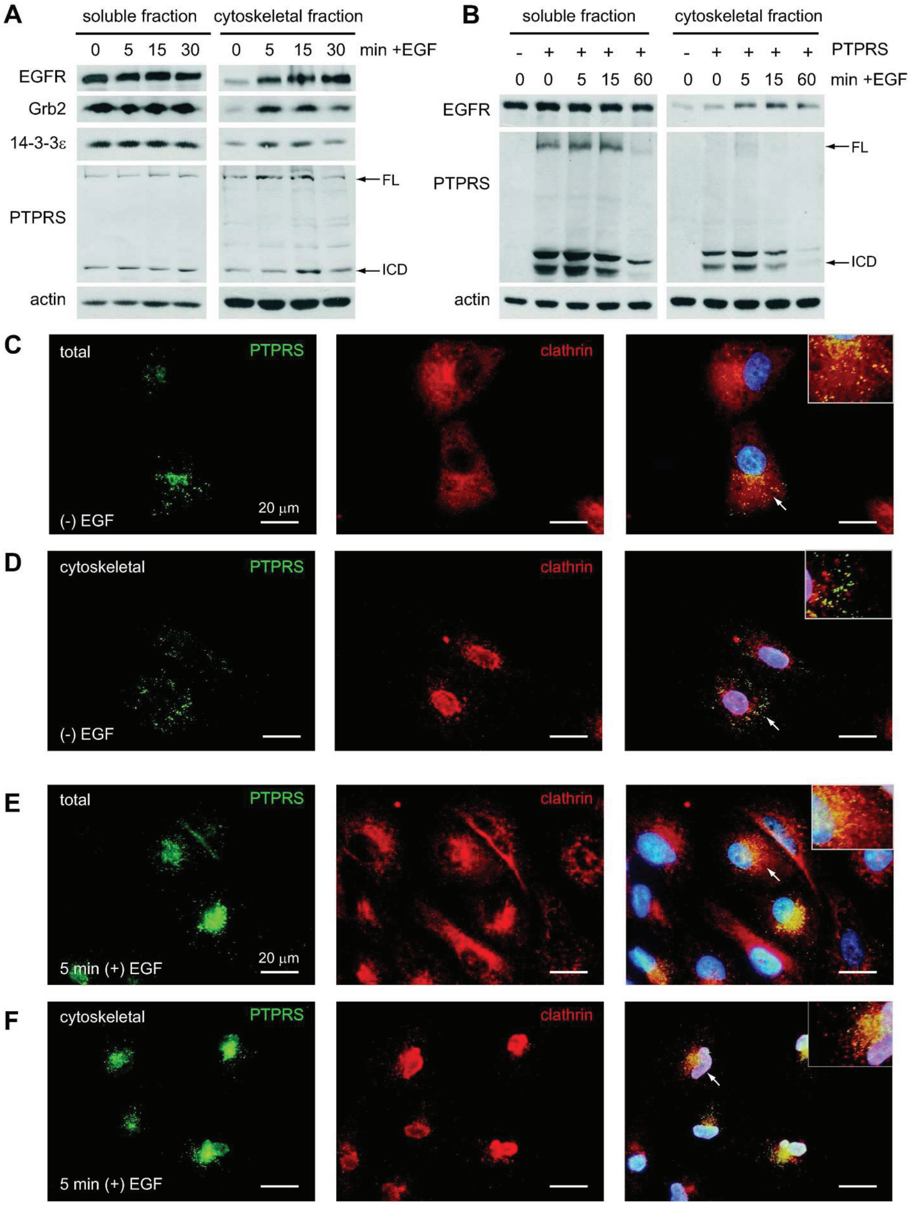

Figure 3. EGF signaling promotes association of Grb2, 14-3-3 epsilon and PTPRS with the cytoskeleton. (A) HK2 cells were plated at fixed density, serum-starved and then stimulated for the indicated time with 100 ng/mL recombinant human EGF. Cells were then biochemically fractionated, and lysates were analyzed by immunoblot for the indicated proteins. The antibody to PTPRS detects endogenous full-length (FL) protein, the processed phosphatase subunit (P-sub), and a further proteolytic C-terminal fragment (CTF). (B) HK2 cells were transfected with pCDNA6.2-PTPRS, which expresses full-length PTPRS under control of the CMV promoter. After 48 hours, the cells were treated with 100 ng/mL EGF for the indicated time and fractionated to isolate the soluble and cytoskeletal fractions of protein lysate. Lysates were separated by SDS-PAGE, transferred to nitrocellulose and probed with primary antibodies to the indicated proteins. (C−F) HK2 cells infected with adenoviruses expressing PTPRS for 24 hours were serum-starved overnight prior to treatment +/− 100 ng/mL EGF for 5 minutes. After stimulation the cells were either fixed directly (C,E) or extracted with buffer containing 1% TritonX-100 prior to fixation (D,F). Cells were then labeled with antibodies for PTPRS (green) and clathrin (red), and co-stained with Hoescht stain (blue) to detect nuclei. Images were captured using an epifluorescent inverted microscope at 60× magnification. Scale bars indicate 20 microns. 2× magnifications of the indicated cells (arrows) are shown in the upper right inset of each merged image to demonstrate separation or colocalization of the PTPRS and clathrin signals.

expressing PTPRS with antibodies to PTPRS and the endosomal marker clathrin, which dynamically associates with the cytoskeleton during vesicular trafficking through the endosomal system via an assortment of different adaptor proteins.[5a] In unstimulated HK2 cells, PTPRS primarily localizes to punctate spots that are evenly distributed throughout the cell and do not colocalize with clathrin (Figure 3C,D). Extraction of unstimulated cells with detergent does not dramatically alter this pattern of staining, suggesting that PTPRS constitutively associates with the cytoskeleton but resides in a nonclathrin coated vesicular compartment in unstimulated HK2 cells (Figure 3D). Upon stimulation of cells with EGF, PTPRS puncta rapidly condense to the perinuclear region and colocalize with clathrin-coated vesicles, consistent with endosomal relocalization (Figure 3E,F). As predicted, both PTPRS and clathrin reside in the detergent-insoluble fraction after EGF stimulation, indicating that both proteins remain associated with the cytoskeleton after EGF stimulation (Figure

3F). We suggest that the relative increase of PTPRS in the cytoskeletal fraction predicted by mass spectrometry and confirmed by immunoblot results from increased flux through the endocytic system induced by EGF. Whether PTPRS is passively or actively recruited into clathrin-coated vesicles in response to EGF awaits further investigation.

CONCLUSIONS

Tethering of membrane proteins to the cortical actin cytoskeleton is a dynamic process that plays an important role in many different cellular functions including endocytosis, vesicular trafficking, migration, and signaling. The regulation of all these processes can be coordinated by extracellular signals, which leads to increased endocytosis and turnover of activated receptors and changes in cellular behavior, such as migration, in response to that signal. The binding of EGF to its receptor is a prototypical example of how a single extracelluar signal can orchestrate rapid changes in cellular behavior concomitant with alterations in endocytosis, vesicular trafficking, and cytoskeletal reorganization.

We used EGF signaling as a tool to demonstrate that tethering of membrane proteins to the actin cytoskeleton rapidly changes in response to a well-defined stimulus. Because activated EGFR has previously been shown to redistribute to a detergent-insoluble compartment in association with the tethering proteins EBP50 and ezrin, we used changes in the biochemical fractionation of EGFR as a positive control for changes in tethering.[7a,21] We then combined biochemical fractionation of the cytoskeletal proteome with membrane protein biotinylation to specifically purify proteins that are physically associated with the cytoskeleton, either by direct tethering or indirect association with biotinylated membrane proteins. Quantitative MS/MS analysis of this purified fraction revealed the composition of the tethered membrane proteome, or “membrane tetherome”, in HK2 cells before and after EGF stimulus.

While the results of our analysis clearly demonstrate that this purification scheme enriches for transmembrane proteins such as EGFR and CD44, the purified fraction also contained proteins that are indirectly associated with the cytoskeletal fraction by binding to the membrane proteins themselves. These interactors can largely be removed by adding SDS to the dissociation buffer used to solubilize the cytoskeletal fraction or by heat denaturation of this fraction prior to streptavidin purification (Supporting Information Figure S2). In this study, we chose not to include this step to allow for detection of important signaling intermediates, such as Grb2 and 14-3-3 epsilon, which redistribute to the cytoskeletal fraction with EGFR. For applications where the presence of indirect interactors is not desired, however, these proteins can easily be removed by chemical or physical means.

Several of the changes in protein tethering we observed are clearly related to changes in signal transduction and cellular behavior elicited by EGF. In HK2 cells, treatment with EGF results in a rapid induction of cellular migration and a more delayed increase in cellular proliferation (data not shown). Since we measured the difference in membrane tetherome composition after only 5 min of EGF stimulation, we anticipated that most of the differentially tethered proteins would be ones that mediate EGFR signaling, membrane trafficking/endocytosis, and cytoskeletal reorganization. Consistent with this hypothesis, we found that many of the proteins that showed a differential abundance of 2-fold or greater in the cytoskeletal fraction after EGF stimulation had been previously associated with these processes.

Interestingly, two large classes of proteins that are not usually associated with EGF-mediated signaling or the cytoskeleton were also highly represented in our analysis. These two classes of proteins are collectively involved in the binding, processing and translation of various types of RNA in the cytoplasm. Importantly, most of these proteins show a loss of cytoskeletal association upon EGF stimulation, suggesting that cellular centers of RNA biosynthesis and protein translation may be stably associated with the actin cytoskeleton under homeostatic growth conditions but are actively released from microfilaments when the cell receives promigratory signals from its environment. One of the RNA processing factors we found to be differentially tethered in response to EGF, small nuclear ribonucleoprotein F (SNRPF), has also been previously shown to bind directly to the EGFR effector Grb2, suggesting a possible mechanistic connection between EGF signaling and RNA processing in the cytoplasm.[19] While further studies are required to further test this hypothesis, our data are strikingly similar to a previous study that identified a large collection of RNA binding and processing proteins physically associated with focal adhesions during the processes of cellular adhesion and spreading.[18] As these cellular processes are directly involved in migration, it is possible that signals that regulate migration also control the association of RNA processing centers with the cytoskeleton.

Under normal homeostatic conditions, it is important for cells to restrict the aberrant activation of signaling receptors by incidental contact with the plasma membrane. In the case of receptor tyrosine kinases (RTKs) such as EGFR, this is achieved by a variety of means including the presence of membrane-associated tyrosine phosphatases that rapidly dephosphorylate low levels of activated receptors. This balance is frequently interrupted in cancer by mutation or loss of these phosphatases.[20,22] Loss of PTPRS, one of the cytoskeletal interactors identified in our study, has recently been associated with head and neck cancers in which EGFR is aberrantly activated. While it has been proposed that PTPRS directly dephosphorylates EGFR in normal epithelial cells, the mechanism by which PTPRS associates with EGFR has not been clearly elucidated. Our findings suggest that PTPRS normally resides in a vesicular compartment that can be rapidly mobilized to the endosome upon EGFR activation.[23] Trafficking of these vesicles is apparently associated with increased cytoskeletal tethering of PTPRS, which explains why this protein was identified in our proteomic analysis. We propose that this phenomenon underlies that ability of PTPRS to localize with and dephosphorylate activated EGFR, though confirmation of this hypothesis awaits further studies.

ASSOCIATED CONTENT

S Supporting Information

Figures S1−S3 and Tables S1−S3. The full list of proteins with 4 or more spectral counts identified by LC−MS/MS, along with quantitative information, can be found in Table S1. CAMthiopropanyol modified peptides indicative of extracellular biotinylation sites are listed in Table S2. Complete HPLC gradient conditions used are listed in Table S3. This material is available free of charge via the Internet at http://pubs.acs.org.

■ AUTHOR INFORMATION

Corresponding Author

*Phone: (616) 234-5503 (B.D.L); (616) 234-5682 (J.P.M.). Fax: (616) 234-5733(B.D.L); (616) 234-5733 (J.P.M.). E-mail: brendan.looyenga@vai.org (B.D.L); jeff.mackeigan@vai.org (J.P.M.).

Notes

The authors declare no competing financial interest.

■ ACKNOWLEDGMENTS

We would like to acknowledge the personnel from MS Bioworks (Ann Arbor, MI) for their exceptional work with the mass spectrometry and data analysis involved in this project. We particularly thank Dr. Michael Ford for his intellectual contributions and help in preparing technical aspects of this manuscript. This work was supported by the Department of Defense Prostate Cancer Research Program of the Office of Congressionally Directed Medical Research Programs PC081089 to JPM. JPM is also supported by Award Number R01CA138651 from the National Cancer Institute.

■ REFERENCES

(1) (a) Morone, N.; Nakada, C.; Umemura, Y.; Usukura, J.; Kusumi, A. Three-dimensional molecular architecture of the plasma-membrane-associated cytoskeleton as reconstructed by freeze-etch electron tomography. *Methods Cell Biol.* **2008**, *88*, 207−36. (b) Golan, D. E.; Veatch, W. Lateral mobility of band 3 in the human erythrocyte membrane studied by fluorescence photobleaching recovery: evidence for control by cytoskeletal interactions. *Proc. Natl. Acad. Sci. U. S. A.* **1980**, *77* (5), 2537−41.

(2) Svetina, S.; Bozic, B.; Derganc, J.; Zeks, B. Mechanical and functional aspects of membrane skeletons. *Cell. Mol. Biol. Lett.* **2001**, *6* (3), 677−90.

(3) (a) Edidin, M.; Zagyansky, Y.; Lardner, T. J. Measurement of membrane protein lateral diffusion in single cells. *Science* **1976**, *191* (4226), 466−8. (b) Leitner, D. M.; Brown, F. L.; Wilson, K. R. Regulation of protein mobility in cell membranes: a dynamic corral model. *Biophys. J.* **2000**, *78* (1), 125−35. (c) Ritchie, K.; Iino, R.; Fujiwara, T.; Murase, K.; Kusumi, A. The fence and picket structure of the plasma membrane of live cells as revealed by single molecule techniques (Review). *Mol. Membr. Biol.* **2003**, *20* (1), 13−8.

(4) (a) Sheetz, M. P. Integral membrane protein interaction with Triton cytoskeletons of erythrocytes. *Biochim. Biophys. Acta* **1979**, *557* (1), 122−34. (b) Mangeat, P.; Burridge, K. Actin-membrane interaction in fibroblasts: what proteins are involved in this association? *J. Cell Biol.* **1984**, *99* (1 Pt 2), 95s−103s.

(5) (a) Schafer, D. A. Coupling actin dynamics and membrane dynamics during endocytosis. *Curr. Opin. Cell Biol.* **2002**, *14* (1), 76−81. (b) Cavey, M.; Lecuit, T. Molecular bases of cell-cell junctions stability and dynamics. *Cold Spring Harbor Perspect. Biol.* **2009**, *1* (5), a002998. (c) Chichili, G. R.; Rodgers, W. Cytoskeleton-membrane interactions in membrane raft structure. *Cell. Mol. Life Sci.* **2009**, *66* (14), 2319−28.

(6) (a) Gautreau, A.; Louvard, D.; Arpin, M. ERM proteins and NF2 tumor suppressor: the Yin and Yang of cortical actin organization and cell growth signaling. *Curr. Opin. Cell Biol.* **2002**, *14* (1), 104−9. (b) Fehon, R. G.; McClatchey, A. I.; Bretscher, A. Organizing the cell cortex: the role of ERM proteins. *Nat. Rev. Mol. Cell Biol.* **2010**, *11* (4), 276−87. (c) Bretscher, A.; Chambers, D.; Nguyen, R.; Reczek, D. ERM-Merlin and EBP50 protein families in plasma membrane organization and function. *Annu. Rev. Cell Dev. Biol.* **2000**, *16*, 113−43.

(7) (a) Chirivino, D.; Del Maestro, L.; Formstecher, E.; Hupe, P.; Raposo, G.; Louvard, D.; Arpin, M. The ERM proteins interact with the HOPS complex to regulate the maturation of endosomes. *Mol. Biol. Cell* **2011**, *22* (3), 375−85. (b) Claperon, A.; Guedj, N.; Mergey, M.; Vignjevic, D.; Desbois-Mouthon, C.; Boissan, M.; Saubamea, B.; Paradis, V.; Housset, C.; Fouassier, L. Loss of EBP50 stimulates EGFR activity to induce EMT phenotypic features in biliary cancer cells. *Oncogene* **2012**, *31* (11), 1376−88.

(8) (a) Cole, B. K.; Curto, M.; Chan, A. W.; McClatchey, A. I. Localization to the cortical cytoskeleton is necessary for Nf2/merlin-dependent epidermal growth factor receptor silencing. *Mol. Cell. Biol.* **2008**, *28* (4), 1274−84. (b) Curto, M.; Cole, B. K.; Lallemand, D.; Liu, C. H.; McClatchey, A. I. Contact-dependent inhibition of EGFR signaling by Nf2/Merlin. *J. Cell Biol.* **2007**, *177* (5), 893−903.

(9) (a) Foster, L. J.; De Hoog, C. L.; Mann, M. Unbiased quantitative proteomics of lipid rafts reveals high specificity for signaling factors. *Proc. Natl. Acad. Sci. U. S. A.* **2003**, *100* (10), 5813−8. (b) Shin, B. K.; Wang, H.; Yim, A. M.; Le Naour, F.; Brichory, F.; Jang, J. H.; Zhao, R.; Puravs, E.; Tra, J.; Michael, C. W.; Misek, D. E.; Hanash, S. M. Global profiling of the cell surface proteome of cancer cells uncovers an abundance of proteins with chaperone function. *J. Biol. Chem.* **2003**, *278* (9), 7607−16. (c) Zhang, M.; Liu, J.; Cheng, A.; Deyoung, S. M.; Saltiel, A. R. Identification of CAP as a costameric protein that interacts with filamin C. *Mol. Biol. Cell* **2007**, *18* (12), 4731−40.

(10) Weekes, M. P.; Antrobus, R.; Lill, J. R.; Duncan, L. M.; Hor, S.; Lehner, P. J. Comparative analysis of techniques to purify plasma membrane proteins. *J. Biomol. Tech.* **2010**, *21* (3), 108−15.

(11) Keller, A.; Nesvizhskii, A. I.; Kolker, E.; Aebersold, R. Empirical statistical model to estimate the accuracy of peptide identifications made by MS/MS and database search. *Anal. Chem.* **2002**, *74* (20), 5383−92.

(12) Nesvizhskii, A. I.; Keller, A.; Kolker, E.; Aebersold, R. A statistical model for identifying proteins by tandem mass spectrometry. *Anal. Chem.* **2003**, *75* (17), 4646−58.

(13) (a) Hoehenwarter, W.; Wienkoop, S. Spectral counting robust on high mass accuracy mass spectrometers. *Rapid Commun. Mass Spectrom.* **2010**, *24* (24), 3609−14. (b) Liu, H.; Sadygov, R. G.; Yates, J. R., 3rd A model for random sampling and estimation of relative protein abundance in shotgun proteomics. *Anal. Chem.* **2004**, *76* (14), 4193−201.

(14) Sorkin, A.; Goh, L. K. Endocytosis and intracellular trafficking of ErbBs. *Exp. Cell Res.* **2009**, *315* (4), 683−96.

(15) London, E.; Brown, D. A. Insolubility of lipids in triton X-100: physical origin and relationship to sphingolipid/cholesterol membrane domains (rafts). *Biochim. Biophys. Acta* **2000**, *1508* (1−2), 182−95.

(16) Oliferenko, S.; Paiha, K.; Harder, T.; Gerke, V.; Schwarzler, C.; Schwarz, H.; Beug, H.; Gunthert, U.; Huber, L. A. Analysis of CD44-containing lipid rafts: Recruitment of annexin II and stabilization by the actin cytoskeleton. *J. Cell Biol.* **1999**, *146* (4), 843−54.

(17) Ponta, H.; Sherman, L.; Herrlich, P. A. CD44: from adhesion molecules to signalling regulators. *Nat. Rev. Mol. Cell Biol.* **2003**, *4* (1), 33−45.

(18) de Hoog, C. L.; Foster, L. J.; Mann, M. RNA and RNA binding proteins participate in early stages of cell spreading through spreading initiation centers. *Cell* **2004**, *117* (5), 649−62.

(19) Hino, N.; Oyama, M.; Sato, A.; Mukai, T.; Iraha, F.; Hayashi, A.; Kozuka-Hata, H.; Yamamoto, T.; Yokoyama, S.; Sakamoto, K. Genetic incorporation of a photo-crosslinkable amino acid reveals novel protein complexes with GRB2 in mammalian cells. *J. Mol. Biol.* **2011**, *406* (2), 343−53.

(20) Morris, L. G.; Taylor, B. S.; Bivona, T. G.; Gong, Y.; Eng, S.; Brennan, C. W.; Kaufman, A.; Kastenhuber, E. R.; Banuchi, V. E.; Singh, B.; Heguy, A.; Viale, A.; Mellinghoff, I. K.; Huse, J.; Ganly, I.; Chan, T. A. Genomic dissection of the epidermal growth factor receptor (EGFR)/PI3K pathway reveals frequent deletion of the EGFR phosphatase PTPRS in head and neck cancers. *Proc. Natl. Acad. Sci. U. S. A.* **2011**, *108* (47), 19024−9.

(21) Balbis, A.; Parmar, A.; Wang, Y.; Baquiran, G.; Posner, B. I. Compartmentalization of signaling-competent epidermal growth factor receptors in endosomes. *Endocrinology* **2007**, *148* (6), 2944−54.

(22) (a) Chan, G.; Kalaitzidis, D.; Neel, B. G. The tyrosine phosphatase Shp2 (PTPN11) in cancer. *Cancer Metastasis Rev.* **2008**,

27 (2), 179−92. (b) Veeriah, S.; Brennan, C.; Meng, S.; Singh, B.; Fagin, J. A.; Solit, D. B.; Paty, P. B.; Rohle, D.; Vivanco, I.; Chmielecki, J.; Pao, W.; Ladanyi, M.; Gerald, W. L.; Liau, L.; Cloughesy, T. C.; Mischel, P. S.; Sander, C.; Taylor, B.; Schultz, N.; Major, J.; Heguy, A.; Fang, F.; Mellinghoff, I. K.; Chan, T. A. The tyrosine phosphatase PTPRD is a tumor suppressor that is frequently inactivated and mutated in glioblastoma and other human cancers. *Proc. Natl. Acad. Sci. U. S. A.* **2009**, *106* (23), 9435−40.

(23) Martin, K. R.; Xu, Y.; Looyenga, B. D.; Davis, R. J.; Wu, C. L.; Tremblay, M. L.; Xu, H. E.; MacKeigan, J. P. Identification of PTPsigma as an autophagic phosphatase. *J. Cell Sci.* **2011**, *124* (Pt 5), 812−9.

Science Signaling
AAAS

` Identification of a Lysosomal Pathway That Modulates Glucocorticoid Signaling and the Inflammatory Response

Yuanzheng He, Yong Xu, Chenghai Zhang, Xiang Gao, Karl J. Dykema, Katie R. Martin, Jiyuan Ke, Eric A. Hudson, Sok Kean Khoo, James H. Resau, Arthur S. Alberts, Jeffrey P. MacKeigan, Kyle A. Furge and H. Eric Xu (5 July 2011)
Science Signaling **4** (180), ra44. [DOI: 10.1126/scisignal.2001450]

The following resources related to this article are available online at http://stke.sciencemag.org.
This information is current as of 31 July 2012.

Article Tools Visit the online version of this article to access the personalization and article tools:
http://stke.sciencemag.org/cgi/content/full/sigtrans;4/180/ra44

Supplemental Materials *"Supplementary Materials"*
http://stke.sciencemag.org/cgi/content/full/sigtrans;4/180/ra44/DC1

Related Content The editors suggest related resources on *Science*'s sites:
http://stke.sciencemag.org/cgi/content/abstract/sigtrans;5/228/ra42
http://stke.sciencemag.org/cgi/content/abstract/sigtrans;4/199/ra75
http://stke.sciencemag.org/cgi/content/abstract/sigtrans;4/180/pc13

References This article has been **cited by** 1 article(s) hosted by HighWire Press; see:
http://stke.sciencemag.org/cgi/content/full/sigtrans;4/180/ra44#BIBL

This article cites 50 articles, 12 of which can be accessed for free:
http://stke.sciencemag.org/cgi/content/full/sigtrans;4/180/ra44#otherarticles

Glossary Look up definitions for abbreviations and terms found in this article:
http://stke.sciencemag.org/glossary/

Permissions Obtain information about reproducing this article:
http://www.sciencemag.org/about/permissions.dtl

Downloaded from stke.sciencemag.org on July 31, 2012

Science Signaling (ISSN 1937-9145) is published weekly, except the last week in December, by the American Association for the Advancement of Science, 1200 New York Avenue, NW, Washington, DC 20005. Copyright 2008 by the American Association for the Advancement of Science; all rights reserved.

PHARMACOLOGY

Identification of a Lysosomal Pathway That Modulates Glucocorticoid Signaling and the Inflammatory Response

Yuanzheng He,[1]*† Yong Xu,[1]* Chenghai Zhang,[1] Xiang Gao,[1] Karl J. Dykema,[2] Katie R. Martin,[3] Jiyuan Ke,[1] Eric A. Hudson,[4] Sok Kean Khoo,[4,5] James H. Resau,[4] Arthur S. Alberts,[6] Jeffrey P. MacKeigan,[3] Kyle A. Furge,[2] H. Eric Xu[1,7]†

The antimalaria drug chloroquine has been used as an anti-inflammatory agent for treating systemic lupus erythematosus and rheumatoid arthritis. We report that chloroquine promoted the transrepression of proinflammatory cytokines by the glucocorticoid receptor (GR). In a mouse collagen-induced arthritis model, chloroquine enhanced the therapeutic effects of glucocorticoid treatment. By inhibiting lysosome function, chloroquine synergistically activated glucocorticoid signaling. Lysosomal inhibition by either bafilomycin A1 (an inhibitor of the vacuolar adenosine triphosphatase) or knockdown of transcription factor EB (TFEB, a master activator of lysosomal biogenesis) mimicked the effects of chloroquine. The abundance of the GR, as well as that of the androgen receptor and estrogen receptor, correlated with changes in lysosomal biogenesis. Thus, we showed that glucocorticoid signaling is regulated by lysosomes, which provides a mechanistic basis for treating inflammation and autoimmune diseases with a combination of glucocorticoids and lysosomal inhibitors.

INTRODUCTION

Glucocorticoids are among the most potent and effective agents for treating inflammation and autoimmune diseases. Synthetic glucocorticoids, including dexamethasone (Dex), fluticasone propionate, and many other steroid analogs, are used clinically for treating asthma, allergy, and rheumatoid arthritis as well as in the treatment of certain cancers, such as leukemia and lymphoma (*1*). However, at therapeutic dosages, glucocorticoids induce a range of debilitating side effects, including diabetes, osteoporosis, skin atrophy, and growth retardation (*2*, *3*). Therefore, the discovery and development of novel synthetic glucocorticoids that retain their beneficial therapeutic effects but reduce adverse side effects remain major medical challenges.

The action of glucocorticoids is mediated through the glucocorticoid receptor (GR), a steroid hormone–regulated transcriptional factor that belongs to the nuclear receptor superfamily. GR regulates gene expression either by transcriptional activation (transactivation) or by transcriptional repression (transrepression). To mediate transactivation, GR binds to a glucocorticoid response element (GRE) and activates downstream gene transcription. To mediate transrepression, GR functionally interacts with other transcriptional factors [such as nuclear factor κB (NF-κB) or activating protein 1 (AP-1)] and represses transcription of their downstream target genes (*4*). The transrepression activity of GR, especially at genes targeted by NF-κB or AP-1, is considered to be the major basis for the anti-inflammatory and immunosuppressive effects of glucocorticoids.

Lysosomes are ubiquitous organelles that are central to cellular homeostasis. They sequester digestive enzymes, such as acidic hydrolases, which are responsible for the degradation and recycling of cellular substrates transferred from exosomes, endosomes, or autophagosomes (*5*). Lysosome biogenesis is coordinated by the transcription factor EB (TFEB), which activates a genetic program that stimulates lysosomal biogenesis and function in response to changing cellular conditions (*6*, *7*). Lysosomal activity is essential to autophagy, a cellular pathway that delivers cytoplasmic components to lysosomes for degradation and is involved in many diseases, including cancer, metabolic syndrome, and viral infections (*8*).

The lumen of lysosomes is acidic (pH ~5.0) relative to the slightly alkaline cytosol (pH 7.2). The acidity of lysosomes is maintained by vacuolar adenosine triphosphatase (V-ATPase) proton pumps, which transport protons from the cytosol into the lysosomal lumen, and chloride ion channels, which transport chloride anion from the lumen to the cytosol (*9*, *10*). The acidic pH of lysosomes is critical for the enzymatic digestion of substrates as well as for vesicle fusion with other vacuolar compartments such as autophagosomes, a key step in autophagy. Neutralization of the internal acidic environment by weak alkaline compounds, such as chloroquine (CQ), or by inhibition of the proton pumps with bafilomycin A1 inhibits lysosomal function (*8*, *11*). CQ is a widely used antimalaria drug that inhibits the growth of parasites by disrupting their lysosome-mediated digestion of heme, which is obtained from feeding on the host's red blood cells (*12*, *13*). CQ and its analog amodiaquine (AQ) have been used as nonsteroidal anti-inflammatory drugs to treat rheumatoid arthritis and lupus erythematosus (*14*, *15*), but the mechanism by which these drugs work remains unclear.

Here, we show that inhibition of lysosomal function, with either CQ or bafilomycin A1 or by knockdown of TFEB, repressed inflammation through potentiation of glucocorticoid signaling, thus providing a mechanistic basis for therapeutic strategies that combine glucocorticoid and lysosomal inhibitors in the treatment of inflammation and autoimmune diseases.

---

[1]Laboratory of Structural Sciences, Van Andel Research Institute, 333 Bostwick Avenue Northeast, Grand Rapids, MI 49503, USA. [2]Laboratory of Computational Biology, Van Andel Research Institute, Grand Rapids, MI 49503, USA. [3]Laboratory of Systems Biology, Van Andel Research Institute, Grand Rapids, MI 49503, USA. [4]Laboratory of Analytical, Cellular, and Molecular Microscopy, Van Andel Research Institute, Grand Rapids, MI 49503, USA. [5]Laboratory of Microarray Technology, Van Andel Research Institute, Grand Rapids, MI 49503, USA. [6]Laboratory of Cell Structure and Signal Integration, Van Andel Research Institute, Grand Rapids, MI 49503, USA. [7]VARI/SIMM Center, Center for Structure and Function of Drug Targets, Shanghai Institute of Materia Medica, Chinese Academy of Sciences, Shanghai 201203, P. R. China.
*These authors contributed equally to this work.
†To whom correspondence should be addressed. E-mail: eric.xu@vai.org (H.E.X.); ajian.he@vai.org (Y.H.)

RESULTS

GR mediated the anti-inflammatory effects of CQ through transrepression of proinflammatory cytokines

CQ suppresses the activity of proinflammatory factors (*16–18*), but it is not clear whether CQ represses the inflammatory signals at the mRNA level or at the protein level. Because macrophages are key cellular mediators of inflammatory responses, we used real-time polymerase chain reaction (PCR) to measure the effects of CQ on the mRNA abundance of interleukin-1β (IL-1β) and IL-6, two proinflammatory cytokines produced by the human THP-1 cells in response to stimulation with lipopolysaccharide (LPS) (Fig. 1A). [THP-1 cells are a monocyte cell line that can be induced to differentiate into macrophages by the phorbol ester PMA (phorbol 12-myristate 13-acetate).] CQ significantly decreased the abundance of transcripts encoding IL-1β and IL-6. Similar results were obtained from mouse macrophage RAW264.7 cells (fig. S1A), suggesting that CQ may inhibit the transcription of these cytokines.

Because the effects of CQ were similar to those of Dex (Fig. 1B), we analyzed the effect of CQ on GR-mediated transactivation and transrepression, using AD293 cells coexpressing the GR with a luciferase reporter gene controlled either by the mouse mammary tumor virus (MMTV) promoter, which is transactivated by GR (*19*), or by an AP-1–controlled promoter, which is transrepressed by GR (*20*, *21*). CQ activated the MMTV reporter and repressed the AP-1 reporter in a dose-dependent manner (Fig. 1, C and D), with a significant effect apparent at 50 μM CQ. Similar results were obtained with the CQ analog AQ (fig. S1B). Knockdown of the endogenous GR in THP-1 cells by small interfering RNA (siRNA) reduced the inhibitory effects of CQ on the expression of the genes encoding IL-1β and IL-6 (Fig. 1, E and F). Together, these data suggest that the anti-inflammatory effects of CQ may be mediated through GR.

CQ potentiates GR signaling in the presence of glucocorticoid

To evaluate the mechanism by which CQ enhanced glucocorticoid signaling, we assayed the effect of CQ on GR distribution, the ability of CQ to compete with GR ligands for binding to the GR, and the ability of CQ to bind heat shock protein 90 (HSP90, a chaperone protein required for GR function). CQ failed to alter the distribution of GR in cells in the presence or absence of the GR ligand Dex (fig. S2). In cell extracts, CQ failed to compete with Dex for binding to GR (Fig. 2A); however, CQ modestly increased the maximal binding ($B_{\max}$; $B_{\max,\mathrm{PBS}} = 3.8$, $B_{\max,\mathrm{CQ}} = 4.9$) of Dex to GR without having much of an effect on the affinity (K_d; $K_{d,\mathrm{PBS}} = 5.2$ nM, $K_{d,\mathrm{CQ}} = 5.8$ nM) (fig. S3A). CQ failed to compete with radiolabeled 17AAG, an inhibitor of HSP90 (*22*), for binding to HSP90 (fig. S3B), suggesting that CQ does not alter GR activity by affecting the activity of its chaperone. The effect of CQ on increasing GR-Dex binding activity is consistent with a previous observation that CQ increased GR activity in rat liver extract (*23*). Therefore, we hypothesized that the anti-inflammatory effect of CQ is mediated by promoting glucocorticoid-mediated GR signaling, which may in part be mediated by increasing the GR-Dex binding activity.

We examined the effect of CQ in the presence of Dex on both GR transactivation and transrepression in AD293 cells. CQ increased Dex-stimulated GR activity, as shown by enhanced activation of the MMTV promoter or repression of the AP-1 promoter (Fig. 2B). This enhancement occurred with all concentrations of Dex, even the highest concentration tested (1 μM in Fig. 2B).

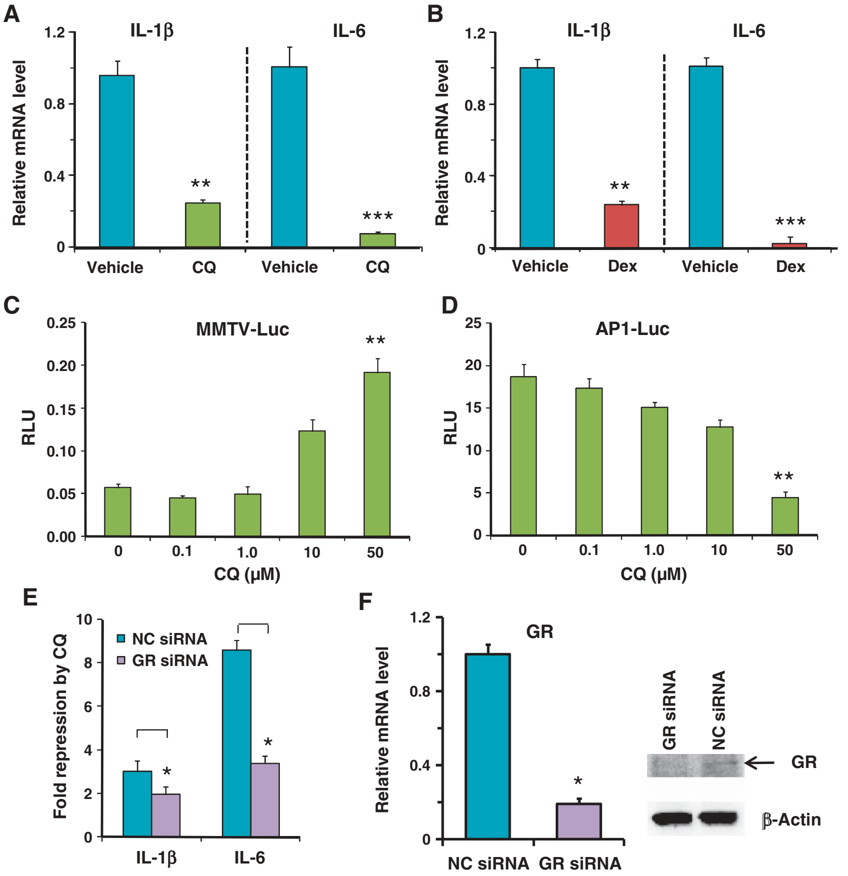

Fig. 1. The anti-inflammatory effect of CQ was partially mediated by GR. (**A**) In THP-1 cells exposed to LPS (1 μg/ml), CQ (50 μM) reduced the mRNA abundance of IL-1β and IL-6 (measured by real-time PCR) compared to PBS (vehicle)–treated cells exposed to LPS (1 μg/ml). Data represent the means and SD ($n \geq 3$ samples). (**B**) Dex (100 nM) repressed IL-1β and IL-6 mRNA transcription in LPS-stimulated THP-1 cells. Data represent the means and SD ($n \geq 3$ samples). (**C**) Dose effect of CQ in activation of the MMTV-luciferase reporter in AD293 cells without added exogenous glucocorticoid. Cells were treated with CQ for 16 hours. RLU, relative luciferase units that were normalized with *Renilla* luciferase. Data represent the means and SD ($n \geq 3$ samples). Statistical significance between the 50 μM and 0 μM CQ samples is indicated. (**D**) Dose effect of CQ in repression of the AP-1 luciferase reporter in AD293 cells exposed to PMA (6.25 ng/ml) in the absence of exogenous glucocorticoid. Data represent the means and SD ($n \geq 3$ samples). Statistical significance between the 50 μM and 0 μM CQ samples is indicated. (**E**) Knockdown of GR by siRNA decreased the repression by CQ of IL-1β and IL-6 mRNA in LPS-stimulated THP-1 cells. Data represent the means and SD ($n \geq 3$ samples). NC siRNA, negative control siRNA. (**F**) GR knockdown efficiency was measured at the mRNA level by real-time PCR and at the protein level by Western blotting with the PA1-511A antibody that recognizes human GR. β-Actin was used as a loading control. mRNA data represent the means and SD of $n \geq 3$ samples and the Western blotting data are representative of three experiments. $^{*}P < 0.05$, $^{**}P < 0.01$, $^{***}P < 0.001$.

CQ also enhanced the gene regulatory responses of other synthetic glucocorticoids, including budesonide, fluticasone propionate, deacylcortivazol, and mometasone furoate, as well as the endogenous hormone cortisol (fig. S3C).

Because CQ stimulated the expression of the MMTV reporter and inhibited that of the AP-1 reporter even in the absence of exogenous Dex (Figs. 1, C and D, and 2C), we reasoned that the activity of CQ on the GR reporters could be due to an effect of CQ on the signaling by endogenous GR ligands (for example, cortisol) in the serum. Indeed, cells exposed to CQ in the presence of serum treated with charcoal, which removes most of endogenous hydrophobic steroids from the serum, exhibited less of an effect on GR-regulated gene expression (Fig. 2C) than did cells exposed to CQ in the presence of untreated serum.

In LPS-stimulated THP-1 cells, CQ significantly enhanced Dex-mediated transrepression of the endogenous GR target genes encoding proinflammatory cytokines IL-1β and IL-6 (Fig. 2D), which was also reflected in reduced secretion of these cytokines (fig. S3D). Similar results were obtained from mouse macrophage RAW264.7 cells exposed to LPS, where we observed a profound enhancement of the reduction in IL-1β mRNA in response to combined treatment with Dex and CQ compared to the response to either CQ or Dex alone (fig. S3E).

The enhancement of Dex-mediated transrepression by CQ in THP-1 cells suggested that this combination might achieve better therapeutic efficacy than either agent alone in treating autoimmune diseases. To test this idea, we measured the therapeutic effects of CQ, Dex, and their combination in a mouse collagen-induced arthritis (CIA) model. We immunized DBA/1 mice with chicken collagen to elicit an inflammatory response. Three weeks later, after the onset of arthritis, mice were given Dex, CQ, or both. Combined treatment with CQ and a low dose of Dex was more effective at ameliorating symptoms than was treatment with either drug alone (Fig. 2, E and F).

CQ enhances glucocorticoid signaling and affects global gene expression in macrophage cells

We performed gene expression profiling on LPS-stimulated THP-1 cells after addition of Dex, CQ, or both (Fig. 3A). We characterized the response to combined treatment as either "enhanced" or "synergistic." Enhanced responses were those that exhibited a greater response in the presence of both Dex and CQ than either drug alone. Synergistic responses were a subset of the enhanced responses and represented those in which in the presence of both Dex and CQ, the response exceeded the sum of the response to either drug individually. The 70 genes with the largest synergistic transactivation effect or transrepression effect upon combined treatment included genes with varying responsiveness to Dex (Fig. 3A). Of the 70 that were synergistically transactivated or transrepressed, these averaged a ~30-fold

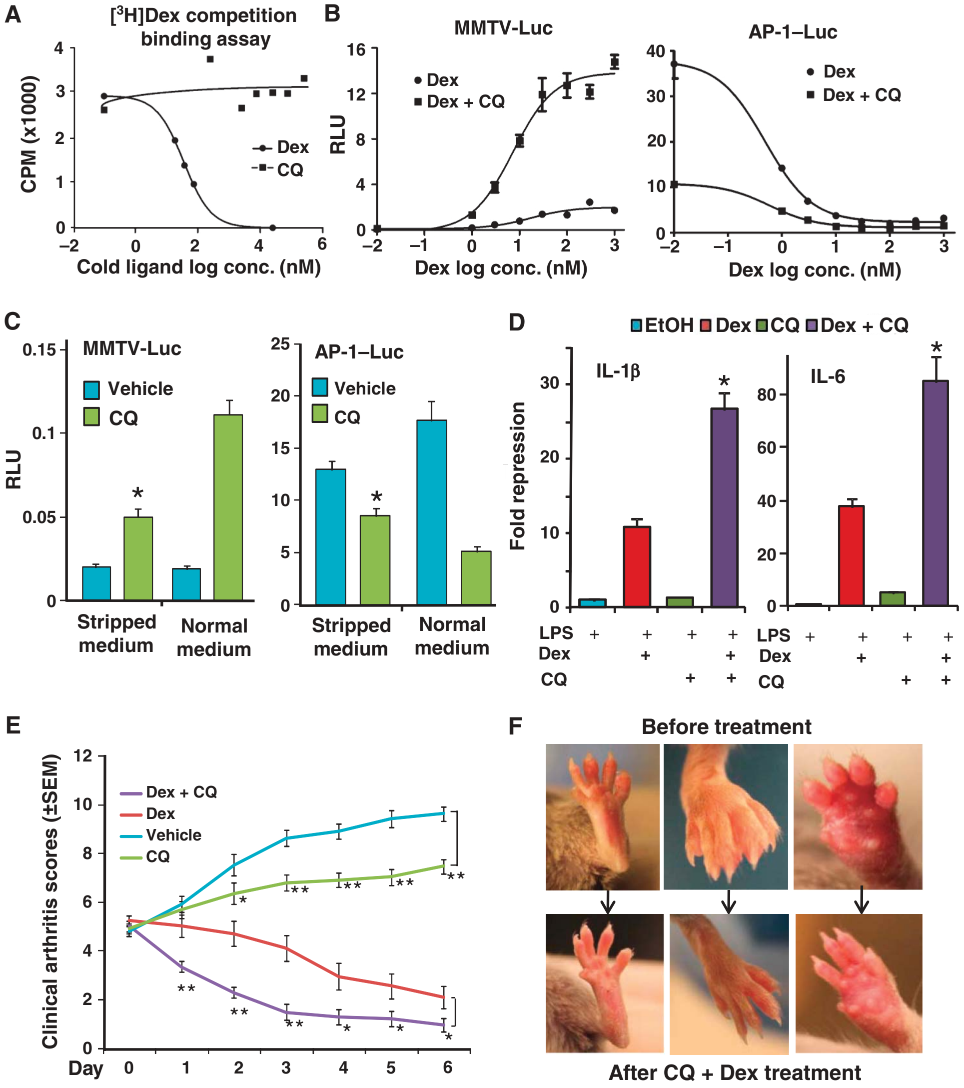

Fig. 2. CQ enhances glucocorticoid-mediated GR signaling. (**A**) CQ and Dex competition assays show that CQ did not bind to GR. Data are representative of three experiments. (**B**) CQ (50 μM) enhanced Dex-stimulated transactivation of the MMTV reporter (MMTV-Luc) or transrepression of the AP-1 reporter (AP-1–Luc) in AD293 cells. For the AP-1 reporter assay, the cells were stimulated with PMA (6.25 ng/ml). Data represent the means and SD ($n \geq 3$ samples). (**C**) Removal of endogenous GR ligands from serum with charcoal (stripped medium) decreased the effectiveness of CQ (50 μM) on enhancing GR-mediated changes in gene expression in AD293 cells. *$P < 0.05$ compared to CQ treatment in the presence of normal medium. Data represent the means and SD ($n \geq 3$ samples). (**D**) CQ (50 μM) enhanced glucocorticoid (Dex, 100 nM)–mediated repression of IL-1β and IL-6 mRNA in THP-1 cells exposed to LPS (1 μg/ml). *$P < 0.05$ compared to Dex-alone treatment. Data represent the means and SD ($n \geq 3$ samples). (**E**) Mean clinical arthritis scores of mice treated with vehicle (PBS, $n = 10$), Dex (4 μg per mouse, $n = 13$), CQ (400 μg per mouse, $n = 10$), or Dex + CQ [(4 μg + 400 μg) per mouse, $n = 15$]. *$P < 0.05$, **$P < 0.01$. (**F**) Representative pictures of the feet of arthritic mice before and after CQ + Dex treatment.

change in gene expression compared with a ~12-fold change in response to Dex alone or ~3-fold (stimulated) or ~5-fold (reduced) change in response to CQ (fig. S4A), with fold change relative to cells exposed to LPS in the absence of any drug treatment. Tables S1 to S5 list the top 70 genes regulated by Dex, CQ, or Dex + CQ, as well as the top 70 genes showing a synergistic effect upon Dex + CQ treatment. There is a modest correlation between Dex + CQ– and CQ-regulated genes with a coefficiency of 0.672 and $P < 2.2 \times 10^{-16}$ (fig. S4B). Consistent with this correlation, the synergistic effect occurred more frequently with genes that exhibited the greatest responsiveness to GR (either induced or repressed), and a larger percentage of repressed genes exhibited the synergistic response (Fig. 3B). For example, the synergy was observed for 70% of genes that were repressed more than 20-fold by Dex treatment alone, whereas synergy was observed only for 15% of genes repressed more than 2-fold by Dex.

We analyzed 14 genes that were synergistically transrepressed and 11 genes that were synergistically transactivated in the microarray experiment with real-time PCR (Fig. 3C and fig. S4C). We chose this subset of genes because they represent a spectrum of Dex-responsive genes for validation of microarray data. Twelve of the 14 repressed genes and 10 of the 11 activated genes exhibited an enhanced response to combined CQ and Dex treatment (Fig. 3C and fig. S4C). Of those that were enhanced, most (10 of 10 activated genes and 9 of 12 repressed genes) also exhibited a synergistic response.

Notables among those synergistically transrepressed were genes encoding phospholipase A2 (PLA2G4A) and several chemokines (Fig. 3C and fig. S4C). PLA2G4A is a key enzyme of prostaglandin-mediated inflammation pathways (*24*), and inhibition of phospholipase A2 is an important mechanism of GR-mediated anti-inflammation (*25*). Many chemokines serve as activators of inflammation and have been linked to many inflammation and autoimmune diseases including rheumatoid arthritis, allergic asthma, and multiple sclerosis (*26*, *27*). All five chemokines transrepressed by Dex more than twofold (CCL1, CCL2, CCL7, CCL8, and CCL19), which are crucial for monocytes and macrophages to induce inflammation (*26*), exhibited a synergistic repression in response to both Dex and CQ. Together, these results suggest that treatment with CQ plus glucocorticoid inhibits the major inflammatory chemokines produced by macrophage cells.

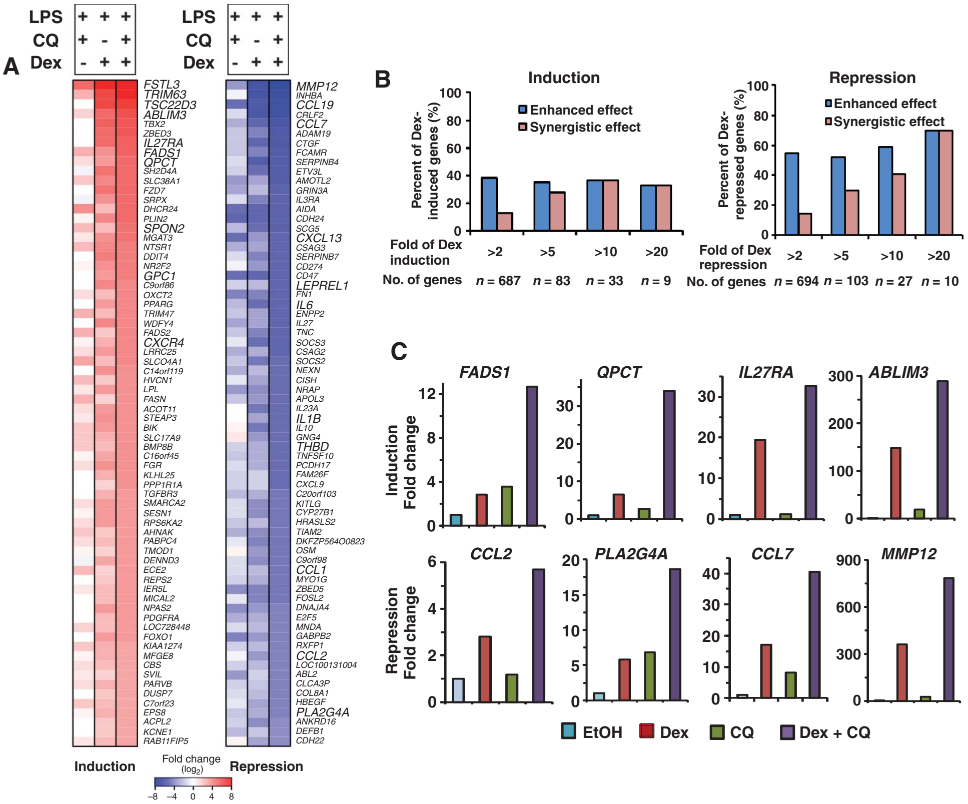

Fig. 3. Gene expression profiling of THP-1 cells exposed to CQ, Dex, or both. (**A**) Top 70 GR-regulated genes that showed a synergistic effect upon treatment with CQ (50 μM) plus Dex (100 nM) in THP-1 cells stimulated with LPS (1 μg/ml). Changes in gene expression of the genes listed in bold capital letters were validated with real-time PCR. (**B**) Percentage of Dex-induced and Dex-repressed genes that have enhanced or synergistic effects with CQ. Enhanced responses were those that in the presence of both Dex and CQ exhibited a greater response than either drug alone (Dex + CQ cotreatment > Dex alone or CQ alone). Synergistic responses represented those in which in the presence of both Dex and CQ, the response more than exceeded the sum of the response to either drug individually (Dex + CQ cotreatment > Dex alone + CQ alone). (**C**) Validation of the synergistic effect on the indicated repressed or activated genes by real-time PCR. Selected genes represent a spectrum of Dex-regulated genes (from low to high); for other validations, see fig. S4. Genes include those particularly relevant for inflammatory responses and represent a range of GR-responsive genes.

Interfering with lysosomal function with V-ATPase inhibitors potentiates glucocorticoid signaling

CQ is a lysosomotropic agent that accumulates in lysosomes and raises the lumenal pH, thereby preventing lysosomal fusion with autophagosomes and inhibiting the clearance of the autolysosomes (*11*, *28*). We used LysoTracker as a pH-sensitive indicator to monitor the effect of CQ on lysosomal pH. When we gradually increased CQ concentration (0 to 250 μM), we observed a gradual reduction in the fluorescence intensity (sharpness) of puncta (Fig. 4A), indicating increased lysosomal pH. Using the lysosomal markers LAMP1 (lysosome-associated membrane protein 1) and LAMP2 and the autophagosomal marker LC3, we also detected the accumulation of autolysosomes and autophagosomes after 24-hour CQ treatment in U2OS cells, which are osteosarcoma cells uniquely fit for performing high-quality imaging of lysosomes (*29*) (fig. S5).

If the effects of CQ on GR signaling are mediated through inhibition of lysosomal functions, other lysosomal inhibitors should have similar effects. Because CQ did not alter GR localization, we verified that inhibition of the V-ATPase proton pump with bafilomycin A1 also did not alter GR localization (fig. S2). Like CQ, bafilomycin A1 and concanamycin A, two inhibitors of the V-ATPase proton pump (*30*), enhanced Dex-mediated transactivation in the MMTV reporter assays in AD293 cells (Fig. 4B) and had a synergistic effect on Dex-mediated transrepression of the genes encoding IL-1β and IL-6 in THP-1 cells (Fig. 4C). Individual knockdown of 12 of the 13 components of the V-ATPase (*9*) with siRNAs in AD293 cells increased GR transactivation (Fig. 4D). Efficiency of knockdown as assessed by real-time PCR was variable, with an average knockdown efficiency of ~70% (fig. S6). These results provide further support that inhibition of lysosomal function enhances glucocorticoid signaling.

TFEB regulates GR transcriptional activity by controlling GR protein degradation

To further establish the relationship between lysosomal function and glucocorticoid signaling, we examined the roles of TFEB, a master transcriptional activator of lysosomal biogenesis (*6*). The transcriptional activity of TFEB correlates closely with the number of lysosomes in response to stimuli, such as starvation, that result in an increased need for lysosomal function (*6*, *7*). In the MMTV reporter assay, knockdown of TFEB increased Dex-induced gene expression (Fig. 5A). In THP-1 cells, knockdown of TFEB mimicked the effect of CQ in repressing the transcription of proinflammatory cytokines (Fig. 5B). Overexpression of TFEB decreased Dex-induced activation of the reporter gene, as well as the reporter gene activity in the absence of Dex, which is an indicator of basal GR activity (Fig. 5C). These results highlight the inverse relationship between lysosomal function and glucocorticoid signaling.

Because one of the key functions of lysosomes is protein degradation, we analyzed whether there was a relationship between lysosomal function and the amount of GR by examining the effect of changing the amount of TFEB on GR abundance and the effect of CQ treatment on GR abundance. In cotransfected AD293 cells, overexpression of TFEB reduced the amount of GR both in the presence and in the absence of Dex (Fig. 5D). Conversely, in U2OS cells stably expressing GR, knockdown of TFEB increased the abundance of GR (Fig. 5E, left) without affecting the amount of GR-encoding mRNA (Fig. 5E, right), indicating that the increased amount of GR was due to decreased lysosomal activity and not to an increase in transcription. Given that CQ is a lysosome inhibitor, CQ may protect GR from degradation by lysosomes. Indeed, CQ increased the amount of GR in U2OS cells stably expressing GR both in the presence and in the absence of Dex (Fig. 5F). A dose-response experiment showed that cells exposed to as little as 10 μM CQ had increased GR (fig. S7), and this was the concentration at which CQ activated the GR-responsive reporter gene (Fig. 1C). Thus, stabilization of GR by CQ through inhibition of lysosomes may contribute to the potentiation of glucocorticoid signaling by CQ.

Degradation of androgen and estrogen receptors is controlled by lysosomal activity

Because androgen receptor (AR) and estrogen receptor (ER) belong to the same nuclear receptor subfamily as GR, we investigated whether AR and ER activities were also regulated by lysosomes. Lysosomal inhibition by CQ enhanced the transcriptional activity of AR and ER in reporter gene assays (Fig. 6, A and B). Increased lysosomal biogenesis resulting from overexpression of TFEB decreased AR and ER activity in reporter gene assays in AD293 cells (Fig. 6, C and D). Correspondingly, overexpression of TFEB reduced the amount of AR and ER (Fig. 6, E and F), without causing any changes in the abundance of p53 or β-catenin, indicating some specificity of lysosome-mediated degradation for steroid hormone receptors. Consistent with this, CQ had no effect on a β-catenin–activated reporter (fig. S8). Thus, lysosomal activity appears to regulate nuclear receptor signaling, which may have implications for developing treatments for diseases associated with aberrant nuclear receptor signaling.

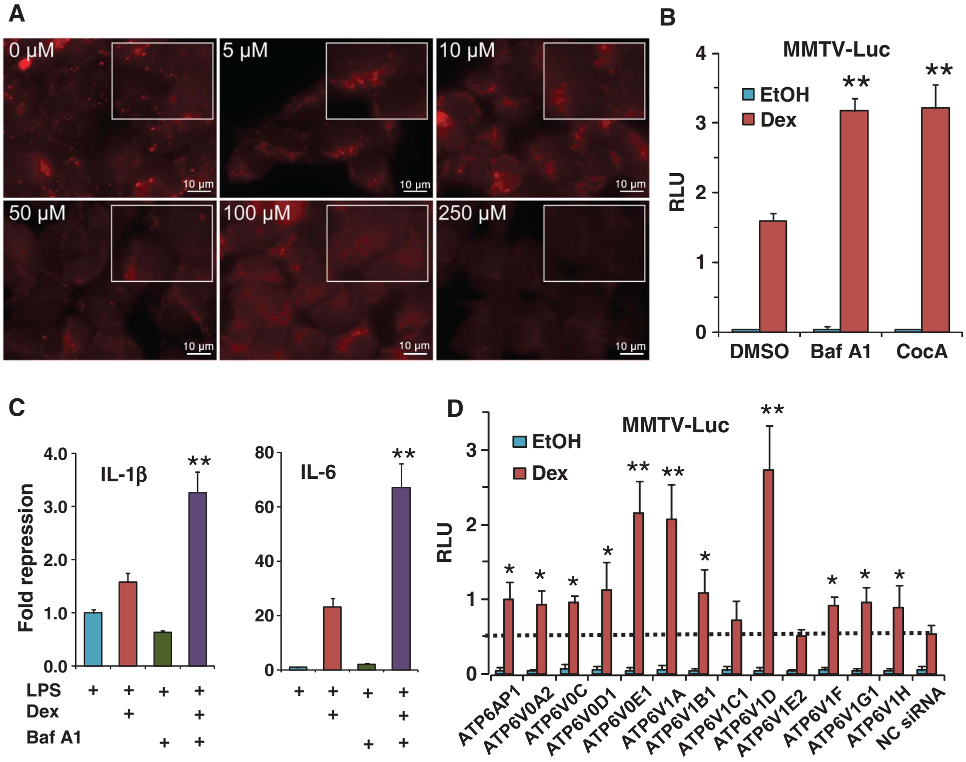

Fig. 4. The V-ATPase inhibitor bafilomycin A1 potentiated glucocorticoid signaling by inhibiting lysosomal function. (**A**) CQ interferes with lysosomal function by increasing lysosomal internal pH. AD293 cells were treated with the indicated concentrations of CQ for 4 hours and then stained with LysoTracker Red, which labels all low-pH compartments. The rectangles represent 1.5× magnifications of regions from within the images; images were obtained by 100×/oil objective lens. Scale bars, 10 μm. (**B**) Bafilomycin A1 (Baf A1, 100 nM) and concanamycin A (CocA, 1 nM) potentiated glucocorticoid (Dex, 10 nM)–stimulated transactivation of the MMTV reporter in AD293 cells. $^{**}P < 0.01$ compared to Dex induction in the presence of dimethyl sulfoxide (DMSO). Data represent the means and SD ($n \geq 3$ samples). (**C**) Baf A1 (100 nM) synergized with glucocorticoid (Dex, 100 nM) in repression of IL-1β and IL-6 mRNA transcription in THP-1 cells in the presence of LPS (1 μg/ml). $^{**}P < 0.01$ compared to Dex induction treatment. Data represent the means and SD ($n \geq 3$ samples). (**D**) Knockdown of V-ATPase components by siRNA potentiated glucocorticoid (Dex, 10 nM)–mediated transactivation of the MMTV reporter in AD293 cells. Dashed line indicates the transactivation level of negative control siRNA (NC siRNA). $^{*}P < 0.05$, $^{**}P < 0.01$, compared to NC siRNA in cells treated with Dex; average siRNA knockdown efficiency was 70 ± 10% as measured by real-time PCR (fig. S6). Data represent the means and SD ($n \geq 3$ samples).

Lysosomes degrade GR to control the stability of cytoplasmic GR

We monitored GR stability in pulse-chase experiments by the HaloTag method (*31*, *32*), which does not require the use of radioactivity. We transiently pulse-labeled Halo-tagged GR (Halo-GR) with the fluorescent TMR (tetramethyl rhodamine) HaloTag ligand, which covalently binds to the HaloTag and then chased with the nonfluorescent succinimidyl ester (O4) HaloTag ligand. In the absence of exogenous GR ligand, the fluorescence signal of TMR-labeled Halo-GR protein [visualized in SDS–polyacrylamide gel electrophoresis (SDS-PAGE) gel] decayed, indicating protein degradation (Fig. 7A). Addition of CQ to inhibit lysosomal function, but not the proteasomal inhibitor MG132, delayed the degradation process, indicating that lysosome is a major pathway for the degradation of cytoplasmic GR in AD293 cells. Analysis of the abundance of GR by Western blotting confirmed that GR accumulated in cells exposed to CQ, but not those exposed to MG132 (Fig. 7A). Because there are no lysosomes in nuclei, it is unlikely that lysosomes contribute to the degradation of nuclear ligand-bound GR. Addition of MG132 to AD293 cells protected GR from degradation in the presence of Dex (Fig. 7B), indicating that nuclear GRs are mainly degraded by the proteasome. CQ appeared to partially stabilize or delay GR degradation in the presence of Dex, which may be due to shuttling from the nucleus to the cytoplasm after ligand binding. Consistent with the importance of the lysosomal pathway in AD293 cells, CQ augmented Dex-mediated reporter gene expression, whereas MG132 had little effect on GR activity (fig. S9A).

However, MG132 increases GR activity in other cell lines, including COS7 cells (*33*, *34*). To determine whether the relative importance of these two degradation pathways was cell line–specific, we evaluated the effect of CQ and MG132 on Dex-mediated reporter gene expression in COS7 cells. Indeed, in COS7 cells, addition of MG132 resulted in a greater enhancement of Dex-mediated reporter gene activity than did addition of CQ (fig. S9B). Thus, cells have at least two pathways that control the abundance of GR, a lysosomal pathway that operates in the cytoplasm and a proteasomal pathway that operates in the nucleus, and the importance of these pathways varies in different cells.

We then used live-cell imaging to track the degradation process of Halo-GR in real time. An advantage of the HaloTag systems is that the protein fate (synthesis, trafficking, and degradation) can be visualized in living cells. Consistent with the biochemical pulse-chase assays, CQ delayed the degradation of GR in living cells (Fig. 7C and videos S1 and S2). Knockdown of TFEB also delayed Halo-GR degradation in pulse-chase experiments (Fig. 7D, top), such that we detected more GR by Western blot (Fig. 7D, bottom). Thus, in both live-cell experiments and biochemical pulse-chase experiments, we showed that lysosomes contribute to the degradation of GR and that inhibition of lysosomal function can stabilize GR.

Because lysosomes rapidly degrade most proteins, with the exception of lysosomal structural proteins or adaptors such as LAMP1 and LAMP2, we could not detect a stable association of GR with lysosomes or LAMP1 or LAMP2. However, by imaging live cells with Halo-GR, we found that the sites positive for lysosome [LAMP1-YFP (LAMP1 fused to yellow fluorescent protein)] had an empty "hole" of Halo-GR (Fig. 7E). We

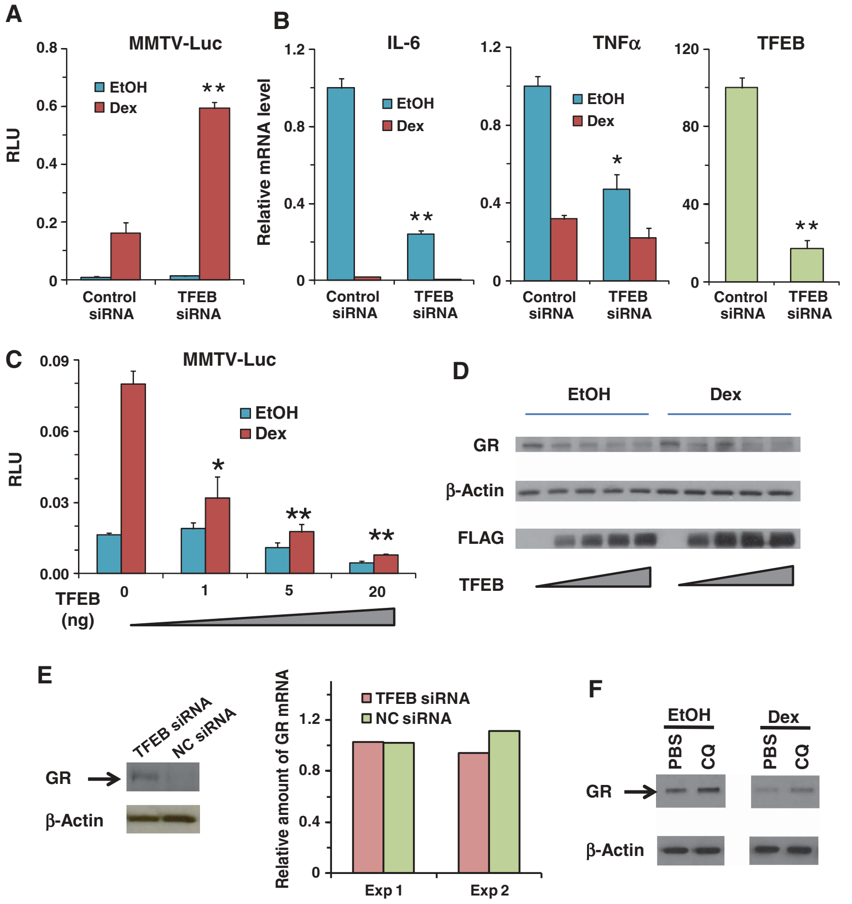

Fig. 5. Lysosomal biogenesis master regulator TFEB regulates GR activity. (A) Knockdown of TFEB by siRNA potentiated glucocorticoid (Dex, 10 nM)–mediated transactivation of the MMTV reporter in AD293 cells. $^{**}P < 0.01$, compared to Dex-treated cells with control siRNA. Data represent the means and SD of $n \geq 3$ samples. (B) Knockdown of TFEB by siRNA decreased proinflammatory cytokines IL-6 and tumor necrosis factor–α (TNFα) mRNA abundances, with or without Dex (100 nM), in THP-1 cells exposed to LPS (1 μg/ml). TFEB knockdown efficiency was measured at the mRNA level. $^{*}P < 0.05$, $^{**}P < 0.01$, compared to control siRNA. Data represent the means and SD ($n \geq 3$ samples). (C) Overexpression of TFEB in AD293 cells inhibited glucocorticoid (Dex, 10 nM)–mediated induction of the MMTV reporter. The TFEB-expressing plasmid (0 to 20 ng) balanced with an equal amount of vehicle plasmid was used in transfection. $^{*}P < 0.05$, $^{**}P < 0.01$, compared to Dex-treated vehicle control samples (TFEB 0 ng). Data represent the means and SD ($n \geq 3$ samples). (D) Cotransfection of TFEB (100 to 1000 ng of 3×FLAG-TFEB per well, six-well plate) with GR (500 ng per well, six-well plate) gradually decreased the amount of GR, with or without GR ligand (Dex, 100 nM) in AD293 cells. GR was detected with the PA1-511A antibody. Data shown are representative of three experiments. (E) Knockdown of TFEB by siRNA increased the abundance of GR in U2OS cells stably expressing GR. Data shown are representative of two experiments. GR mRNA was not affected by TFEB siRNA as measured by real-time PCR. Data from two experiments are shown. (F) CQ (50 μM) increased the amount of GR in U2OS cells stably expressing GR, with or without glucocorticoid (Dex, 100 nM). β-Actin served as the loading control. Data shown are representative of three experiments.

also noted that the Halo-GR holes moved in the same direction as lysosomes (video S3). We interpret the absence of GR staining in those areas occupied by lysosomes as degradation of GR in the lysosomes. Because the association of GR and lysosomes is transient, we performed continuous recording of GR and lysosomes to visualize the interaction. We captured yellow "sparks" at the border of lysosomes, which may represent GR entering the lysosomes (Fig. 7F and video S3). The yellow sparks appeared and disappeared quickly, which is consistent with the rapid association of GR with lysosomes and fast degradation.

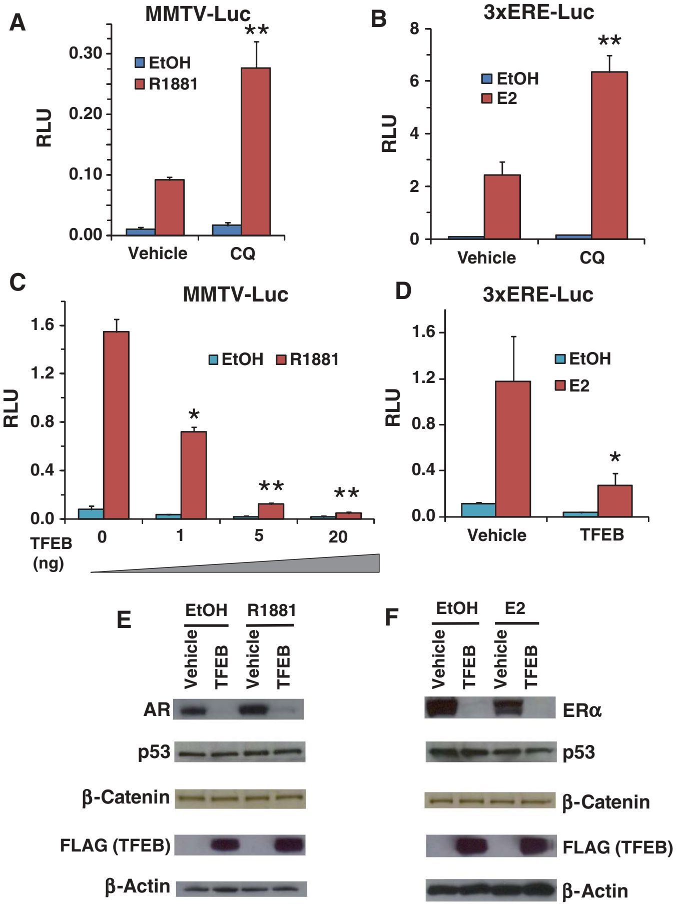

Fig. 6. Lysosomes regulate AR and ER activity. (**A**) CQ enhanced the transactivation activity of the AR ligand R1881 (10 nM) on the MMTV reporter in AD293 cells. $^{**}P < 0.01$ compared to vehicle control R1881–treated cells. Data represent the means and SD ($n \geq 3$ samples). (**B**) CQ enhanced the transactivation activity of the ER ligand E2 (10 nM) on the ERE reporter in AD293 cells. $^{**}P < 0.01$ compared to vehicle control E2–treated cells. Data represent the means and SD ($n \geq 3$ samples). (**C**) Overexpression of TFEB decreased the AR (R1881, 10 nM)–mediated activation of the MMTV reporter in AD293 cells. $^{*}P < 0.05$, $^{**}P < 0.01$ compared to vehicle control (TFEB 0 ng) R1881–treated cells. Data represent the means and SD ($n \geq 3$ samples). (**D**) Overexpression of TFEB decreased the ER (E2, 10 nM)–mediated activation of the MMTV reporter in AD293 cells. $^{*}P < 0.05$ compared to vehicle control E2–treated cells. Data represent the means and SD ($n \geq 3$ samples). (**E**) Cotransfection of TFEB (250 ng of 3×FLAG-TFEB per well in 24-well plate) with AR (100 ng/well, 24-well plate) decreased the abundance of AR, with or without the AR ligand R1881 (10 nM), in AD293 cells. AR was detected with the 441 antibody; endogenous p53 and β-catenin were detected with the DO-1 and 610154 antibodies, respectively. (**F**) Cotransfection of TFEB (250 ng of 3×FLAG-TFEB in 24-well plate) with ER (100 ng/well, 24-well plate) decreased the abundance of ER, with or without the ER ligand E2 (10 nM) in AD293 cells. ER was detected with the F10 antibody.

DISCUSSION

We present three main discoveries. First, we identify a mechanism by which CQ and its analog AQ function as anti-inflammatory drugs by enhancing the activity of glucocorticoids and thereby repressing the transcription of proinflammation cytokines. Second, we demonstrate an inverse relationship between lysosomal function and glucocorticoid signaling, such that conditions that reduce lysosomal functions (CQ or bafilomycin treatment or TFEB knockdown) lead to increased glucocorticoid signaling. Third, we provide evidence that lysosomes are a site of GR degradation and thus control the stability of cytoplasmic GR. These discoveries provide a mechanistic framework for understanding the role of lysosomes and glucocorticoids in the development and homeostasis of the immune system and also provide a rational basis for developing new therapeutics that can be combined with glucocorticoids for treating inflammation and autoimmune diseases.

As major organelles responsible for the degradation and recycling of cellular substrates, lysosomes play critical roles in host cell defense by digesting intracellular and extracellular pathogens (*35*, *36*). The catabolic functions of lysosomes are required for antigen processing and presentation to the major histocompatibility complex (MHC) class II (*37*), which is crucial both for the development of self-tolerance and for the development of autoimmune diseases by immune systems. Endogenous glucocorticoids, like cortisol, through their interaction with GR, also have critical roles in the development and homeostasis of immune systems (*38*). In addition, cortisol and related synthetic glucocorticoids are used to treat inflammation and autoimmune diseases because of their potent inhibitory effects on immune systems. Despite the importance of both the lysosomal and the glucocorticoid pathways in regulating the immune system, the functional relationship between these two pathways had not been identified previously.

The inverse relationship between lysosomal and glucocorticoid pathways provides a new perspective in considering their modulation of the immune system. We reason that lysosomal biogenesis and function would expand in response to attacks of infectious agents on the host cells, which should then repress glucocorticoid signaling so that inflammatory cytokines are produced and attract other components of the immune system. In contrast, the demand for lysosomal functions would be reduced after destruction of the pathogens, and an increased sensitivity to glucocorticoid signaling would repress the expression of genes encoding inflammatory cytokines and chemokines. In this situation of infection and clearance, lysosomes not only serve as clearing houses that help host cells to get rid of pathogens, but also serve as signaling hubs that regulate the activity of the immune system through modulation of glucocorticoid activity.

Having established a relationship between lysosomal function and glucocorticoid signaling, we explored mechanisms by which this occurred and found that lysosomes controlled the stability of cytoplasmic GR without affecting its localization. However, we anticipate that stabilization of the receptor may only be part of the mechanism by which lysosomes regulate cellular responsiveness to glucocorticoids. We speculate that some of the potentiation of glucocorticoid signaling by CQ could result from the cellular consequences of the malfunction of lysosomes. The disruption of lysosomal function affects pathways including protein synthesis, degradation, and trafficking. Homeostasis of lysosomes, as well as of autophagosomes, is critical for many physiological and pathological processes that involve autophagy, including the balance of catabolism and anabolism, antigen

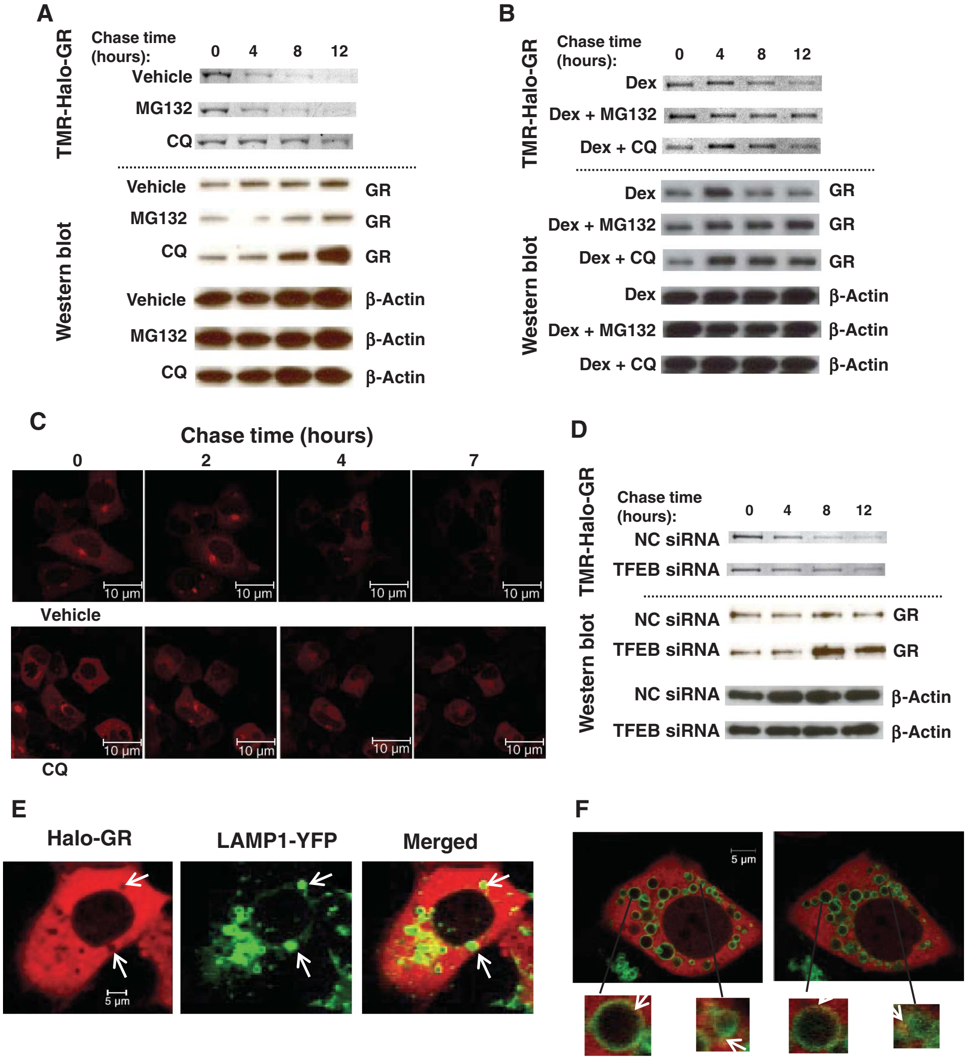

Fig. 7. A lysosomal pathway contributes to degradation of cytoplasmic GR. (**A**) Pulse-chase assay of unliganded GR in AD293 cells. AD293 cells were transfected with 200 ng of Halo-GR per well in 24 wells. Cells were pulse-labeled with 20 nM TMR ligand and then chased with 10 μM succinimidyl ester (O4) ligand. Upper panels, fluorescent TMR-Halo-GR SDS-PAGE scanning images. Lower panels, Western blots. GR was detected by PA1-511A antibody. CQ (50 μM) and MG132 (10 μM) were added at the same time that chase began. Data shown are representative of three experiments. (**B**) Pulse-chase assay of liganded GR in AD293 cells. Cells were transfected, labeled, and chased as described for (A). Upper panel, TMR-Halo-GR bands; lower panel, Western blots. Dex (100 nM), CQ (50 μM), and MG132 (10 μM) were added at the same time that chase began. Data shown are representative of three experiments. (**C**) Live-cell images of Halo-GR in the pulse-chase assay. AD293 cells were passaged into 40-mm glass-bottomed dishes and transfected with 0.5 μg of Halo-GR. Halo-GR was labeled with 2 nM TMR ligand (red fluorescence) and chased with 10 μM O4 ligand. Images were obtained with a 40× confocal microscope. Scale bar, 10 μm. See videos S1 and S2. (**D**) Pulse-chase assay of GR AD293 cells in which TFEB was knocked down. AD293 cells were transfected with 200 ng of Halo-GR together with 20 nM target siRNA in 24-well plates. Cells were labeled and chased as described in (A). Upper panel, TMR-Halo-GR bands; lower panel, Western blots. Data shown are representative of two experiments. (**E**) Live-cell images of Halo-GR and LAMP1-YFP in AD293 cells. Cells were transfected with 500 ng of Halo-GR and 500 ng of LAMP1-YFP in 40-mm glass-bottomed dishes. Cells were pulse-labeled by 20 nM TMR ligand; images were obtained with a 40× confocal microscope. Scale bar, 5 μm. Arrows indicate lysosomal location. (**F**) Dynamic association of Halo-GR and lysosomes in AD293 cells. Cells were transfected and labeled as in (E). Images were obtained with a 60× confocal microscope. Scale bar, 5 μm. Arrows point to the yellow sparks of lysosomes, indicating GR movement. See video S3.

presentation, bone remodeling, body development, and tumorigenesis (*8*). Therefore, it is unlikely that the activation of glucocorticoid signaling due to interference with lysosomal function can be explained by a single signaling event, which may also partially explain the variability in the gene expression response to lysosomal interference. Detailed mechanisms of this dynamic regulation between lysosome function and glucocorticoid signaling, including how GR is targeted to lysosomes, will be a subject of future investigation.

The identification of a lysosomal pathway for the cytoplasmic degradation of receptors of the nuclear receptor family was unexpected because it is generally established that the ubiquitin-proteasome system is responsible for the rapid clearance of active transcriptional factors (*39*, *40*), and the autophagy-lysosome pathway is responsible for the clearance of aged organelles and aggregated damaged proteins (*8*). However, we found that nuclear-localized GR (ligand-bound) was mainly degraded by a proteasome-dependent process, and cytoplasmic GR was mainly controlled by lysosomes, although we did note cell-specific differences in the relative contributions of these two pathways. These pathways may also contribute to regulate GR activity differently under different circumstances, such as during differentiation or development.

Similar to GR activity, we found that AR and ER activities were also controlled by lysosomes (Fig. 6). Because AR and ER contribute to the development and progression of prostate cancers and breast cancers (*41*–*43*), the reduction in AR and ER abundance in response to overexpressed TFEB suggests that increasing lysosomal function could be used as a strategy to reduce AR and ER signaling, which may lead to therapeutic applications for prostate cancer and breast cancer.

Given the widespread clinical use of glucocorticoids for treating inflammatory diseases and cancers, our discovery of the synergism between CQ and glucocorticoids has immediate therapeutic implications. Clinical studies of rheumatoid arthritis have shown that combined treatment of CQ with a low dose of glucocorticoid (for example, prednisolone at <15 mg/day) achieved a better effect, in terms of reducing joint destruction and increasing the remission rate, than either agent alone (*44*–*46*). Our results provide mechanistic insight for this treatment strategy and suggest that combined treatment not only will allow a lower dose of glucocorticoid to be effective but may also achieve therapeutic effects in situations when even a maximal dose of glucocorticoid fails to suppress the inflammation. Our study addresses why the combined treatment has better effects and provides a rational basis for developing new therapeutic applications by leveraging the synergy between glucocorticoids and lysosomal inhibitors.

In summary, we have discovered a mechanism of action for the anti-inflammatory effects of CQ and AQ, in which these lysosomal inhibitors synergize with glucocorticoids to mediate transrepression of proinflammatory signals. Although not all of the anti-inflammatory effects of CQ may be mediated by enhancing the immunosuppressive effect of glucocorticoids, our results suggest that this is a major mechanism responsible for the repression of proinflammatory signals at the transcriptional level. Second, we have discovered an inverse relationship between lysosomal biogenesis and function and glucocorticoid signaling, which has both theoretical importance and therapeutic implication. Combined with the established roles of lysosomes in antigen presentation and pathogen clearance, the present work pushes these ubiquitous organelles further to the center of cellular processing of inflammatory responses. Our work opens a new field of opportunity to explore proteins associated with lysosomal pathways as drug targets for treating inflammation, autoimmune diseases, and cancer.

MATERIALS AND METHODS

Antibodies and Western blotting

The antibody recognizing GR was purchased from Thermo Scientific (PA1-511A), the antibody recognizing AR (441) was from Santa Cruz (sc7305), the antibody recognizing ERα (F10) was from Santa Cruz (sc8002), the antibody recognizing p53 (DO-1) was from Santa Cruz (sc-126), the antibody recognizing β-catenin was from BD Biosciences (#610154), the antibody recognizing FLAG (M2) was from Sigma (F-1804), the antibody recognizing LAMP1 (LY1C6) was from Abcam (#ab13523), and the antibody recognizing LAMP2 (ABL-93) was from Santa Cruz (sc-20004). For Western blotting, protein lysates separated by 4 to 20% gradient SDS-PAGE were transferred to nitrocellulose membrane. Membranes were blocked with 10% milk and then incubated with appropriate first and second antibodies with extensive washes (three times) between each step. Chemiluminescent signals were detected by SuperSignal West Pico (Pierce).

Cell transfection and reporter gene assays

For testing of GR-mediated transactivation, AD293 cells were transfected with 100 ng of pHHLuc (MMTV-Luc) plasmid, 0.1 ng of pRShGR (encoding human full-length GR) by FuGENE 6 (Roche), and 5 ng of *Renilla* luciferase control plasmid per well in 24-well plates. For GR-mediated repression, AD293 cells were transfected with 10 ng of AP-1–Luc, 10 to 100 ng of pRShGR, and 5 ng of *Renilla* luciferase control plasmid per well (24-well plate). At 24 hours after transfection, cells were subjected to various treatments (Dex, CQ, AQ, or different combinations) overnight in the presence of PMA (6.25 ng/ml), which increases AP-1 transcriptional activity to allow detection of repression of its activity by Dex in the AD293 cells. Luciferase activity was assayed with the Dual-Glo Luciferase system (Promega).

For the Wnt TCF (T cell factor) reporter assay, 293STF cells (with an integrated “Super-Top-Flash” TCF luciferase reporter) were transfected with 20 ng of *Renilla* control plasmid. Cells were induced with the indicated reagents 24 hours after transfection. Cells were harvested 17 hours after induction.

Total RNA extraction and real-time PCR

THP-1 cells were induced with PMA (25 ng/ml) for 48 hours to differentiate into macrophage cells (for RAW264.7 cells, differentiation did not require PMA). The differentiated cells were exposed to the indicated reagents (Dex or other synthetic hormones, CQ, or a combination thereof) in the presence of LPS (1 μg/ml) for 12 hours. Total RNA was extracted with either Trizol (Invitrogen) or a Qiagen RNA extraction kit. Complementary DNA (cDNA) was synthesized from total RNA with an Invitrogen Superscript cDNA synthesis kit. Target genes were quantified with a Power SYBR Green real-time PCR kit (ABI) in a StepOnePlus Real-Time PCR instrument. In every case, GAPDH (glyceraldehyde-3-phosphate dehydrogenase) was used as an internal control and data were analyzed by the $\Delta\Delta C_t$ method. The specificity of target primers was tested both in a dissociation curve and against a water control. See table S6 for the sequences of all target gene primers. Fold changes in induction or repression were calculated as compared to the appropriate vehicle control group [for example, DMSO, EtOH, or a mixture thereof, or phosphate-buffered saline (PBS)].

siRNA and transfection

THP-1 cells were induced with PMA (100 ng/ml) for 24 hours to differentiate into macrophages, and then they were transfected with 20 to 50 nM siRNA using siLentFect (Bio-Rad). At 24 to 48 hours after transfection, cells were exposed to the indicated reagents in the presence of LPS (1 μg/ml) for 6 to 12 hours, and then RNA was isolated and subjected to real-time PCR analysis. AD293 cells were transfected with 10 nM siRNA by HiPerFect (Qiagen) in 24-well plates; for DNA and siRNA mixture transfection, 100 ng of DNA plasmid and 20 nM siRNA were transfected with Lipofectamine 2000 (Invitrogen) in 24-well plates. See table S7 for all siRNA target sequences.

In vitro GR ligand binding assay and Dex and HSP90 competition assays

We grew U2OS cells stably expressing GR to 100% confluence and then isolated cytosolic fractions as previously described (*47*). Cytosol (5 to 10%) supplemented with 20 mM sodium molybdate was added to varying concentrations of [^{3}H]Dex (0 to 25 nM) ± 100-fold excess of non-radioactive Dex and incubated at 4°C for 16 hours. To test the effect of CQ on GR-Dex binding, we added 50 μM CQ (or PBS control) to the [^{3}H]Dex cytosol mixtures. Unbound [^{3}H]Dex was removed by dextran-coated charcoal. Standard binding curve was plotted by [bound steroid] versus [free steroid]. The binding capacity and affinity were also determined by Scatchard plot analysis by plotting [bound steroid]/[free steroid] versus [bound steroid]. For the competition binding assay performed with CQ and [^{3}H]Dex, [^{3}H]Dex was fixed at 25 nM, and then varying concentrations of CQ (0.25 to 2.5 mM) were added; the data were plotted as a standard competition curve. For the competition assay with CQ and 17AAG for HSP90 binding, [^{3}H]17AAG was fixed at 25 nM and then varying CQ concentrations (2.5 nM to 500 μM) were added; the data were plotted as a standard competition curve. Experiments were repeated at least three times with duplicate at each point.

Mouse CIA model

DBA/1 male mice (7 to 10 weeks old; Taconic) were intradermally immunized at the base of the tail with 100 μl of chicken collagen/FCA (Freund’s complete adjuvant) emulsion (EK-0210, Hooke Laboratories). Twenty-one days later, they were given a 100-μl booster dose of chicken collagen/FIA (Freund’s incomplete adjuvant) emulsion (EK-0211, Hooke Laboratories). From day 20 after the first immunization, mice were monitored daily for clinical symptoms of arthritis. The clinical score of arthritis per paw was graded according to the Hooke Laboratories manual as follows: 0, normal paw; 1, one toe inflamed and swollen; 2, more than one toe, but not the entire paw, inflamed and swollen, or mild swelling of entire paw; 3, entire paw inflamed and swollen; and 4, very inflamed and swollen paw or ankylosed paw. If the paw was ankylosed, the mouse could not grip the wire top of the cage. Thus, each mouse could be scored from 0 to 16.

Upon arthritis onset (score of 3 to 4), mice were randomized and given the following treatments by intraperitoneal injection: vehicle, Dex (4 μg per mouse), CQ (400 μg), or Dex/CQ (4 μg + 400 μg) in 200 μl of PBS. Blood was withdrawn by intracardiac puncture or from the orbital sinus at the seventh day after treatment, and then the mice were euthanized. All animal procedures were approved by the institutional animal care and ethics committee.

Microarray analysis gene expression of THP-1 cells

THP-1 cells were differentiated into macrophages by treating with PMA (25 ng/ml) for 48 hours, and then the cells were exposed to vehicle (EtOH), Dex (100 nM), CQ (50 μM), or Dex + CQ (100 nM and 50 μM, respectively), in the presence of LPS (1 μg/ml) for 12 hours. Total RNA was isolated with a Qiagen RNeasy kit. Expression measurements were generated with the Agilent Whole Human Genome 44K platform. All subsequent analyses were performed with the Bioconductor software environment (*48*). Expression data were processed and normalized as described (*49*) with assistance from the Bioconductor limma package (*50*). To identify genes associated with CQ treatment, we compared CQ + LPS cells with LPS cells, and CQ + Dex + LPS cells with Dex + LPS cells. Genes in tables S1 to S5 and Fig. 3 were identified using the following criteria: expression after Dex + LPS treatment was at least twofold increased versus LPS alone, and expression in Dex + CQ was greater than expression in either Dex or CQ alone. Similarly, expression after Dex + LPS treatment was at least twofold decreased versus LPS alone, and expression in Dex + CQ was lower than in either Dex or CQ alone.

Pulse-chase experiments with HaloTag

We monitored GR stability in pulse-chase experiments by means of the HaloTag method, a recombinant protein tag method that enables specific labeling of target proteins (*31*, *32*). AD293 cells were passaged and transfected with 200 ng of Halo-GR by Lipofectamine 2000 in 24-well plates. One day after transfection, cells were pulse-labeled with 20 nM TMR ligand for 15 min at 37°C according to the Promega manual, and then cells were washed with fresh phenol-free medium [plus 10% charcoal-stripped fetal bovine serum (FBS)] four times. Cells were chased with 10 μM preblocked succinimidyl ester (O4) ligand in phenol-free (10% charcoal-stripped FBS) medium for various time periods. The succinimidyl ester (O4) ligand was preblocked by incubation in 100 mM tris-Cl (pH 8.0) for 60 min at room temperature to mask the functional group. Cells were lysed by 1× Passive Lysis Buffer (Promega); the lysis solution was mixed with 2× SDS loading buffer, incubated at 95°C for 2 min, and separated by SDS-PAGE. Gels were visualized by the Bio-Rad ChemiDoc XRS Plus system. Experiments were repeated at least three times.

Live-cell imaging

AD293 cells were passaged into 40-mm glass-bottomed culture dishes (MatTek). One day after growth, cells were transfected with Halo-GR with or without LAMP1-YFP (*51*). Twenty-four hours later, Halo-GR was labeled with 2 nM TMR ligand for 15 min at 37°C. Live-cell images were obtained with a Zeiss LSM 510 Meta confocal system. For pulse-chase experiments to monitor Halo-GR protein stability, cells were chased with 10 μM O4 ligand as described above; pictures were taken every 5 min for up to 7 hours. For colocalization experiments, pictures were taken every 20 s for 1 to 2 hours. Images were analyzed by Zeiss LSM Browser (v4.2). Movies of living cell images were produced with Zeiss 510 Laser Scanning Microscope software V3.2 SP1 (Carl Zeiss Microimaging).

To determine the effect of CQ and bafilomycin A1 on GR localization, we passaged AD293 cells into 24-well plates. One day after growth, cells were transfected with 20 ng of pEYFP-GR by FuGENE 6. Twenty-four hours later, cells were treated with the indicated reagents (CQ and bafilomycin A1) with or without Dex. Fluorescent images were taken 3 hours after treatment with a Nikon Eclipse TE300 system.

Statistical analysis

All mouse data (clinical arthritis scores) were expressed as the means ± SEM ($n \geq 5$ samples). Reporter assays and real-time PCR data were expressed as the means ± SD of at least triplicate samples. Data were analyzed by two-tailed, unpaired *t* tests with GraphPad Prism 5 or Excel software.

SUPPLEMENTARY MATERIALS

www.sciencesignaling.org/cgi/content/full/4/180/ra44/DC1
Fig. S1. Activity of CQ and amodiaquine (AQ).
Fig. S2. Effect of CQ and bafilomycin A1 on GR localization in AD293 cells.
Fig. S3. CQ enhances glucocorticoid-mediated GR signaling.
Fig. S4. Microarray analysis of the effect of CQ/Dex on gene expression in THP-1 cells.
Fig. S5. CQ inhibition of lysosomes leads to accumulation of autophagosomes and autolysosomes.
Fig. S6. Knockdown efficiency of the siRNAs targeting components of the V-ATPase.
Fig. S7. CQ stabilizes GR in AD293 cells.
Fig. S8. The effect of CQ on a β-catenin–activated reporter gene.
Fig. S9. Effect of the proteasome inhibitor MG132 and the lysosomal inhibitor CQ on GR activation in AD293 cells and COS7 cells.
Table S1. Top 70 genes regulated by Dex in LPS-stimulated THP-1 cells.
Table S2. Top 70 genes regulated by CQ in LPS-stimulated THP-1 cells.
Table S3. Top 70 genes regulated by Dex + CQ in LPS-stimulated THP-1 cells.
Table S4. Top 70 genes showing a synergistic transactivation effect upon Dex + CQ treatment in LPS-stimulated THP-1 cells.
Table S5. Top 70 genes showing a synergistic transrepression effect upon Dex + CQ treatment in LPS-stimulated THP-1 cells.
Table S6. Real-time PCR primers for target genes.
Table S7. siRNA target sequences.
Descriptions for Videos S1 to S3
Video S1. Pulse chase of Halo-GR in AD293 cells with PBS vehicle.
Video S2. Pulse chase of Halo-GR in AD293 cells exposed to CQ.
Video S3. Dynamic association of GR and lysosomes in AD293 cells.

REFERENCES AND NOTES

1. P. J. Barnes, Anti-inflammatory actions of glucocorticoids: Molecular mechanisms. *Clin. Sci.* **94**, 557–572 (1998).
2. H. Schäcke, W. D. Döcke, K. Asadullah, Mechanisms involved in the side effects of glucocorticoids. *Pharmacol. Ther.* **96**, 23–43 (2002).
3. R. M. Stanbury, E. M. Graham, Systemic corticosteroid therapy—Side effects and their management. *Br. J. Ophthalmol.* **82**, 704–708 (1998).
4. K. R. Yamamoto, Steroid receptor regulated transcription of specific genes and gene networks. *Annu. Rev. Genet.* **19**, 209–252 (1985).
5. P. Saftig, *Lysosomes* (Springer Science+Business Media Inc., New York, 2005).
6. M. Sardiello, M. Palmieri, A. di Ronza, D. L. Medina, M. Valenza, V. A. Gennarino, C. Di Malta, F. Donaudy, V. Embrione, R. S. Polishchuk, S. Banfi, G. Parenti, E. Cattaneo, A. Ballabio, A gene network regulating lysosomal biogenesis and function. *Science* **325**, 473–477 (2009).
7. C. Settembre, C. Di Malta, V. A. Polito, M. G. Arencibia, F. Vetrini, S. Erdin, S. U. Erdin, T. Huynh, D. Medina, P. Colella, M. Sardiello, D. C. Rubinsztein, A. Ballabio, TFEB links autophagy to lysosomal biogenesis. *Science* **332**, 1429–1433 (2011).
8. B. Levine, G. Kroemer, Autophagy in the pathogenesis of disease. *Cell* **132**, 27–42 (2008).
9. M. Forgac, Vacuolar ATPases: Rotary proton pumps in physiology and pathophysiology. *Nat. Rev. Mol. Cell Biol.* **8**, 917–929 (2007).
10. T. J. Jentsch, T. Friedrich, A. Schriever, H. Yamada, The CLC chloride channel family. *Pflugers Arch.* **437**, 783–795 (1999).
11. D. C. Rubinsztein, J. E. Gestwicki, L. O. Murphy, D. J. Klionsky, Potential therapeutic applications of autophagy. *Nat. Rev. Drug Discov.* **6**, 304–312 (2007).

12. A. Dorn, R. Stoffel, H. Matile, A. Bubendorf, R. G. Ridley, Malarial haemozoin/β-haematin supports haem polymerization in the absence of protein. *Nature* **374**, 269–271 (1995).
13. D. J. Sullivan Jr., I. Y. Gluzman, D. G. Russell, D. E. Goldberg, On the molecular mechanism of chloroquine's antimalarial action. *Proc. Natl. Acad. Sci. U.S.A.* **93**, 11865–11870 (1996).
14. P. Augustijns, P. Geusens, N. Verbeke, Chloroquine levels in blood during chronic treatment of patients with rheumatoid arthritis. *Eur. J. Clin. Pharmacol.* **42**, 429–433 (1992).
15. I. M. Meinão, E. I. Sato, L. E. Andrade, M. B. Ferraz, E. Atra, Controlled trial with chloroquine diphosphate in systemic lupus erythematosus. *Lupus* **5**, 237–241 (1996).
16. B. E. van den Borne, B. A. Dijkmans, H. H. de Rooij, S. le Cessie, C. L. Verweij, Chloroquine and hydroxychloroquine equally affect tumor necrosis factor-α, interleukin 6, and interferon-γ production by peripheral blood mononuclear cells. *J. Rheumatol.* **24**, 55–60 (1997).
17. I. Karres, J. P. Kremer, I. Dietl, U. Steckholzer, M. Jochum, W. Ertel, Chloroquine inhibits proinflammatory cytokine release into human whole blood. *Am. J. Physiol.* **274**, R1058–R1064 (1998).
18. C. H. Jang, J. H. Choi, M. S. Byun, D. M. Jue, Chloroquine inhibits production of TNF-α, IL-1β and IL-6 from lipopolysaccharide-stimulated human monocytes/macrophages by different modes. *Rheumatology* **45**, 703–710 (2006).
19. G. M. Ringold, K. R. Yamamoto, G. M. Tomkins, M. Bishop, H. E. Varmus, Dexamethasone-mediated induction of mouse mammary tumor virus RNA: A system for studying glucocorticoid action. *Cell* **6**, 299–305 (1975).
20. C. Jonat, H. J. Rahmsdorf, K. K. Park, A. C. Cato, S. Gebel, H. Ponta, P. Herrlich, Antitumor promotion and antiinflammation: Down-modulation of AP-1 (Fos/Jun) activity by glucocorticoid hormone. *Cell* **62**, 1189–1204 (1990).
21. I. Rogatsky, K. A. Zarember, K. R. Yamamoto, Factor recruitment and TIF2/GRIP1 corepressor activity at a collagenase-3 response element that mediates regulation by phorbol esters and hormones. *EMBO J.* **20**, 6071–6083 (2001).
22. Q. Xie, R. Wondergem, Y. Shen, G. Cavey, J. Ke, R. Thompson, R. Bradley, J. Daughtery-Holtrop, Y. Xu, E. Chen, H. Omar, N. Rosen, D. Wenkert, H. E. Xu, G. F. Vande Woude, Benzoquinone ansamycin 17AAG binds to mitochondrial voltage-dependent anion channel and inhibits cell invasion. *Proc. Natl. Acad. Sci. U.S.A.* **108**, 4105–4110 (2011).
23. M. Kalimi, Role of lysosomotrophic reagents in glucocorticoid hormone action. *Biochim. Biophys. Acta* **883**, 593–597 (1986).
24. E. A. Dennis, Diversity of group types, regulation, and function of phospholipase A2. *J. Biol. Chem.* **269**, 13057–13060 (1994).
25. T. Rhen, J. A. Cidlowski, Antiinflammatory action of glucocorticoids—New mechanisms for old drugs. *N. Engl. J. Med.* **353**, 1711–1723 (2005).
26. I. F. Charo, R. M. Ransohoff, The many roles of chemokines and chemokine receptors in inflammation. *N. Engl. J. Med.* **354**, 610–621 (2006).
27. T. Iwamoto, H. Okamoto, Y. Toyama, S. Momohara, Molecular aspects of rheumatoid arthritis: Chemokines in the joints of patients. *FEBS J.* **275**, 4448–4455 (2008).
28. N. Mizushima, T. Yoshimori, B. Levine, Methods in mammalian autophagy research. *Cell* **140**, 313–326 (2010).
29. K. R. Martin, Y. Xu, B. D. Looyenga, R. J. Davis, C. L. Wu, M. L. Tremblay, H. E. Xu, J. P. MacKeigan, Identification of PTPσ as an autophagic phosphatase. *J. Cell Sci.* **124**, 812–819 (2011).
30. M. Huss, H. Wieczorek, Inhibitors of V-ATPases: Old and new players. *J. Exp. Biol.* **212**, 341–346 (2009).
31. K. Yamaguchi, S. Inoue, O. Ohara, T. Nagase, Pulse-chase experiment for the analysis of protein stability in cultured mammalian cells by covalent fluorescent labeling of fusion proteins. *Methods Mol. Biol.* **577**, 121–131 (2009).
32. G. V. Los, L. P. Encell, M. G. McDougall, D. D. Hartzell, N. Karassina, C. Zimprich, M. G. Wood, R. Learish, R. F. Ohana, M. Urh, D. Simpson, J. Mendez, K. Zimmerman, P. Otto, G. Vidugiris, J. Zhu, A. Darzins, D. H. Klaubert, R. F. Bulleit, K. V. Wood, HaloTag: A novel protein labeling technology for cell imaging and protein analysis. *ACS Chem. Biol.* **3**, 373–382 (2008).
33. B. J. Deroo, C. Rentsch, S. Sampath, J. Young, D. B. DeFranco, T. K. Archer, Proteasomal inhibition enhances glucocorticoid receptor transactivation and alters its subnuclear trafficking. *Mol. Cell. Biol.* **22**, 4113–4123 (2002).
34. A. D. Wallace, J. A. Cidlowski, Proteasome-mediated glucocorticoid receptor degradation restricts transcriptional signaling by glucocorticoids. *J. Biol. Chem.* **276**, 42714–42721 (2001).
35. V. Deretic, B. Levine, Autophagy, immunity, and microbial adaptations. *Cell Host Microbe* **5**, 527–549 (2009).
36. C. Munz, Enhancing immunity through autophagy. *Annu. Rev. Immunol.* **27**, 423–449 (2009).
37. B. Levine, V. Deretic, Unveiling the roles of autophagy in innate and adaptive immunity. *Nat. Rev. Immunol.* **7**, 767–777 (2007).
38. A. Winoto, D. R. Littman, Nuclear hormone receptors in T lymphocytes. *Cell* **109** (suppl.), S57–S66 (2002).
39. A. Ciechanover, D. Finley, A. Varshavsky, Ubiquitin dependence of selective protein degradation demonstrated in the mammalian cell cycle mutant ts85. *Cell* **37**, 57–66 (1984).
40. C. M. Pickart, Back to the future with ubiquitin. *Cell* **116**, 181–190 (2004).
41. C. D. Chen, D. S. Welsbie, C. Tran, S. H. Baek, R. Chen, R. Vessella, M. G. Rosenfeld, C. L. Sawyers, Molecular determinants of resistance to antiandrogen therapy. *Nat. Med.* **10**, 33–39 (2004).
42. Z. Bai, R. Gust, Breast cancer, estrogen receptor and ligands. *Arch. Pharm.* **342**, 133–149 (2009).
43. J. T. Isaacs, W. B. Isaacs, Androgen receptor outwits prostate cancer drugs. *Nat. Med.* **10**, 26–27 (2004).
44. T. Möttönen, P. Hannonen, M. Leirisalo-Repo, M. Nissilä, H. Kautiainen, M. Korpela, L. Laasonen, H. Julkunen, R. Luukkainen, K. Vuori, L. Paimela, H. Blåfield, M. Hakala, K. Ilva, U. Yli-Kerttula, K. Puolakka, P. Järvinen, M. Hakola, H. Piirainen, J. Ahonen, I. Pälvimäki, S. Forsberg, K. Koota, C. Friman, Comparison of combination therapy with single-drug therapy in early rheumatoid arthritis: A randomised trial. FIN-RACo trial group. *Lancet* **353**, 1568–1573 (1999).
45. R. F. van Vollenhoven, Treatment of rheumatoid arthritis: State of the art 2009. *Nat. Rev. Rheumatol.* **5**, 531–541 (2009).
46. B. Svensson, A. Boonen, K. Albertsson, D. van der Heijde, C. Keller, I. Hafström, Low-dose prednisolone in addition to the initial disease-modifying antirheumatic drug in patients with early active rheumatoid arthritis reduces joint destruction and increases the remission rate: A two-year randomized trial. *Arthritis Rheum.* **52**, 3360–3370 (2005).
47. S. Cho, B. L. Kagan, J. A. Blackford Jr., D. Szapary, S. S. Simons Jr., Glucocorticoid receptor ligand binding domain is sufficient for the modulation of glucocorticoid induction properties by homologous receptors, coactivator transcription intermediary factor 2, and Ubc9. *Mol. Endocrinol.* **19**, 290–311 (2005).
48. R. C. Gentleman, V. J. Carey, D. M. Bates, B. Bolstad, M. Dettling, S. Dudoit, B. Ellis, L. Gautier, Y. Ge, J. Gentry, K. Hornik, T. Hothorn, W. Huber, S. Iacus, R. Irizarry, F. Leisch, C. Li, M. Maechler, A. J. Rossini, G. Sawitzki, C. Smith, G. Smyth, L. Tierney, J. Y. Yang, J. Zhang, Bioconductor: Open software development for computational biology and bioinformatics. *Genome Biol.* **5**, R80 (2004).
49. T. A. Patterson, E. K. Lobenhofer, S. B. Fulmer-Smentek, P. J. Collins, T. M. Chu, W. Bao, H. Fang, E. S. Kawasaki, J. Hager, I. R. Tikhonova, S. J. Walker, L. Zhang, P. Hurban, F. de Longueville, J. C. Fuscoe, W. Tong, L. Shi, R. D. Wolfinger, Performance comparison of one-color and two-color platforms within the MicroArray Quality Control (MAQC) project. *Nat. Biotechnol.* **24**, 1140–1150 (2006).
50. G. K. Smyth, Linear models and empirical Bayes methods for assessing differential expression in microarray experiments. *Stat. Appl. Genet. Mol. Biol.* **3**, Article3 (2004).
51. N. M. Sherer, M. J. Lehmann, L. F. Jimenez-Soto, A. Ingmundson, S. M. Horner, G. Cicchetti, P. G. Allen, M. Pypaert, J. M. Cunningham, W. Mothes, Visualization of retroviral replication in living cells reveals budding into multivesicular bodies. *Traffic* **4**, 785–801 (2003).

52. **Acknowledgments:** We would like to thank the Van Andel Research Institute animal facility (D. Dylewski, L. DeCamp, and E. Boguslawski) for helping in animal study and the microarray facility (M. Vadlapatla) for microarray data collection, Q. Xie for some reagents, S. Stoney Simons Jr. [National Institute of Diabetes and Digestive and Kidney Diseases (NIDDK)] for reagents and advice on steroid binding assay, and W. Mothes (Yale School of Medicine) for LAMP1-YFP plasmid. **Funding:** This study was supported by an NIDDK/NIH fund (DK066202 and DK071662), an American Asthma Foundation fund (2010) to H.E.X., Department of Defense Prostate Cancer Research Program of the Office of Congressionally Directed Medical Research Programs PC081089 to J.P.M., and the Jay and Betty Van Andel Foundation. **Author contributions:** Y.H., Y.X., and H.E.X. conceived the project. H.E.X., Y.H., Y.X., J.H.R., A.S.A., J.P.M., and K.A.F. designed the experiments. Y.H. performed the bulk of the experiments with additional contributions from Y.X., C.Z., X.G., K.J.D., K.R.M., E.A.H., A.S.A., and S.K.K. at the different stages of the project. H.E.X. and Y.H. wrote the paper with comments from all authors. **Competing interests:** Compositions of CQ or an analog of CQ in combination with a GR ligand and methods of use (U.S. Patent Application No. 61/236,681). **Accession numbers:** The microarray data have been submitted into the National Center for Biotechnology Information Gene Expression Omnibus database (accession no. GSE24579).

Submitted 20 August 2010
Accepted 16 June 2011
Final Publication 5 July 2011
10.1126/scisignal.2001450
Citation: Y. He, Y. Xu, C. Zhang, X. Gao, K. J. Dykema, K. R. Martin, J. Ke, E. A. Hudson, S. K. Khoo, J. H. Resau, A. S. Alberts, J. P. MacKeigan, K. A. Furge, H. E. Xu, Identification of a lysosomal pathway that modulates glucocorticoid signaling and the inflammatory response. *Sci. Signal.* **4**, ra44 (2011).

Identification of Small Molecule Inhibitors of PTPσ through an Integrative Virtual and Biochemical Approach

Katie R. Martin[1], Pooja Narang[2]ᵍ, Yong Xu[3]ᵍ, Audra L. Kauffman[1], Joachim Petit[2], H. Eric Xu[3], Nathalie Meurice[2], Jeffrey P. MacKeigan[1]*

1 Laboratory of Systems Biology, Van Andel Research Institute, Grand Rapids, Michigan, United States of America, **2** Mayo Clinic, Scottsdale, Arizona, United States of America, **3** Laboratory of Structural Sciences, Van Andel Research Institute, Grand Rapids, Michigan, United States of America

Abstract

PTPσ is a dual-domain receptor type protein tyrosine phosphatase (PTP) with physiologically important functions which render this enzyme an attractive biological target. Specifically, loss of PTPσ has been shown to elicit a number of cellular phenotypes including enhanced nerve regeneration following spinal cord injury (SCI), chemoresistance in cultured cancer cells, and hyperactive autophagy, a process critical to cell survival and the clearance of pathological aggregates in neurodegenerative diseases. Owing to these functions, modulation of PTPσ may provide therapeutic value in a variety of contexts. Furthermore, a small molecule inhibitor would provide utility in discerning the cellular functions and substrates of PTPσ. To develop such molecules, we combined *in silico* modeling with *in vitro* phosphatase assays to identify compounds which effectively inhibit the enzymatic activity of PTPσ. Importantly, we observed that PTPσ inhibition was frequently mediated by oxidative species generated by compounds in solution, and we further optimized screening conditions to eliminate this effect. We identified a compound that inhibits PTPσ with an IC_{50} of 10 μM in a manner that is primarily oxidation-independent. This compound favorably binds the D1 active site of PTPσ *in silico,* suggesting it functions as a competitive inhibitor. This compound will serve as a scaffold structure for future studies designed to build selectivity for PTPσ over related PTPs.

Citation: Martin KR, Narang P, Xu Y, Kauffman AL, Petit J, et al. (2012) Identification of Small Molecule Inhibitors of PTPσ through an Integrative Virtual and Biochemical Approach. PLoS ONE 7(11): e50217. doi:10.1371/journal.pone.0050217

Editor: Andreas Hofmann, Griffith University, Australia

Received January 12, 2012; **Accepted** October 22, 2012; **Published** November 20, 2012

Funding: This work was supported by the Department of Defense Prostate Cancer Research Program of the Office of Congressionally Directed Medical Research Programs PC081089 to JPM. JPM is also supported by Award Number R01CA138651 from the National Cancer Institute. Award Number RC2MH090878 from the National Institute of Mental Health awarded to NM provided partial support for the work described in this paper. The content is solely the responsibility of the authors and does not necessarily represent the official views of the National Institutes of Health. The funders had no role in study design, data collection and analysis, decision to publish, or preparation of the manuscript.

Competing Interests: The authors have declared that no competing interests exist.

* E-mail: jeff.mackeigan@vai.org

ᵍ These authors contributed equally to this work.

Introduction

Tyrosine phosphorylation is a critical mechanism by which cells exert control over signaling processes. Protein tyrosine kinases (PTKs) and phosphatases (PTPs) work in concert to control these signaling cascades, and alterations in the expression or activity of these enzymes hallmark many human diseases [1,2]. While PTKs have long been the focus of extensive research and drug development efforts, the role of PTPs as critical mediators of signal transduction was initially underappreciated [3]. Consequently, the molecular characterization of these phosphatases has trailed that of PTKs, and only recently has the PTP field reached the forefront of disease based-research. As validation for phosphastases in human disease, half of PTP genes are now implicated in at least one human disease [3].

The critical role of PTPs in cell function and their role in disease etiology highlight the importance of developing phosphatase agonists and inhibitors. Unfortunately, phosphatases have historically been perceived as "undruggable" for several important reasons [4]. First, phosphatases often control multiple signaling pathways and thus, inhibition of a single enzyme may not yield a specific cellular effect. Second, signaling cascades are generally controlled by multiple phosphatases and accordingly, blocking the activity of one may not sufficiently induce the desired modulation to a signaling pathway. Finally, and most importantly, phosphatase active sites display high conservation which hinders the ability to develop catalysis-directed inhibitors with any degree of selectivity [4]. Despite these pitfalls, the emerging role of PTPs in human disease etiology has necessitated a solution. Largely through use of structure-based drug design, several PTPs now represent promising targets for disease treatment. Most notably, bidentate inhibitors of PTP1B, implicated in type II diabetes and obesity, have been developed which span both the catalytic pocket and a second substrate binding pocket discovered adjacent to the active site [5,6,7].

Drug development around PTP1B has provided a proof-of-concept for investigations focused on additional PTP targets. Several studies have uncovered physiologically important and disease relevant functions for the classic receptor type PTP, PTPσ (encoded by the *PTPRS* gene), which underscore its potential as a biological target. PTPσ is highly expressed in neuronal tissue where it regulates axon guidance and neurite outgrowth [8,9,10,11,12]. Furthermore, it was recently reported that loss of PTPσ facilitates nerve regeneration following spinal cord injury (SCI), owing to the interaction of its ectodomain with chondroitin sulfate proteoglycans (CSPGs) [13,14]. In addition to its neural function, PTPσ has been implicated in chemoresistance of cancer cells. First, we discovered that RNAi-mediated knockdown of PTPσ in cultured cancer cells confers resistance to several chemotherapeutics [15]. Additionally, we have discovered that loss of PTPσ hyperactivates autophagy, a cellular recycling program that may contribute to chemoresistance of cancer cells [16]. Taken together, it is apparent that modulation of PTPσ may have therapeutic potential in a range of contexts. Notably, inhibition of PTPσ could potentially provide benefit following SCI through enhanced neural regeneration. In addition, it is possible that PTPσ inhibition may yield therapeutic value in diseases in which increasing autophagy represents a promising treatment strategy (i.e., neurodegenerative diseases). Furthermore, a small molecule would provide value as a molecular probe or tool compound to interrogate the cellular functions and disease implications of PTPσ.

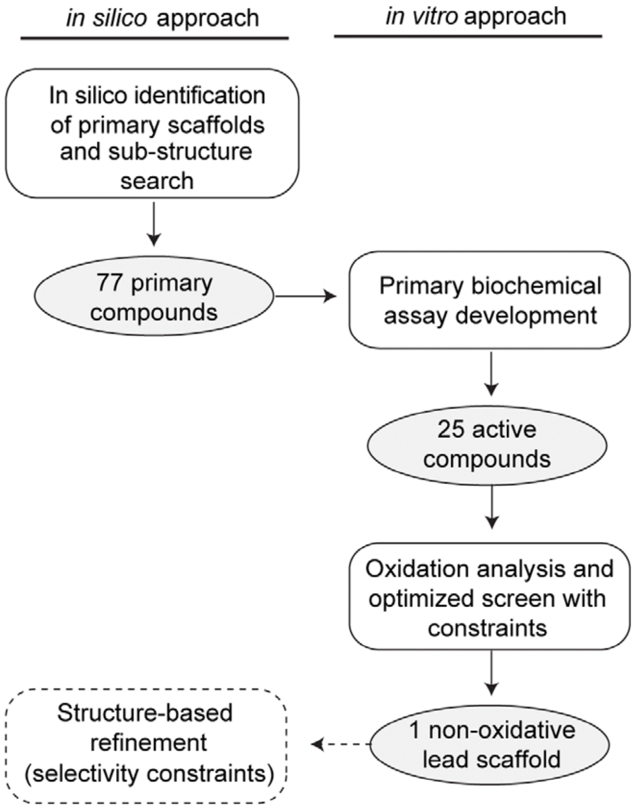

Figure 1. Workflow overview for PTPσ inhibitor development. *In silico* docking was performed using the crystal structure of the D1 active site of PTPσ as a target (PDB ID: 2fh7). Three structurally distinct scaffolds were chosen, along with 74 additional compounds identified by a sub-structure search of compounds in the ChemBridge, were tested *in vitro* to for the ability to inhibit PTPσ phosphatase activity. To eliminate oxidation-mediated inhibition, we optimized the biochemical assay and discovered one lead compound whose inhibition was not mediated by oxidation. Future efforts (dashed boxes and lines) will introduce selectivity into this lead compound through a detailed structural analysis of PTPσ and related PTPs.
doi:10.1371/journal.pone.0050217.g001

Several approaches exist for the identification of small molecule inhibitors of phosphatases. While high-throughput screening (HTS) of compounds *in vitro* has been successfully utilized to discover inhibitors of LAR (PTPRF), PTP1B, SHP2, CD45, and others [17], the technical and physical investment is considerable as is the potential for experimental artifacts leading to false negatives and positives [17]. Alternatively, a primary screen for inhibitor scaffolds can be guided by *in silico* virtual screening. This method involves high-throughput computational docking of small molecules into the crystal structure of a phosphatase active site and selecting the molecules which bind favorably, akin to a natural substrate [18]. Following the selection of the best-scoring scaffolds, each scaffold can then be tested and validated for phosphatase inhibition *in vitro*. This approach has gained popularity as the number of enzymes with solved crystal structures has increased and it is advantageous in many ways. First, utilization of the phosphatase structure allows for the exclusion of molecules which have little chance of interacting with the active site, greatly reducing the number of scaffolds to be biochemically screened and improving the screen results. Second, an understanding of the unique structural features and residues comprising the active site as well as proximal folds or binding pockets can guide the selection and refinement of an inhibitor. Furthermore, an *in silico* approach is incredibly efficient in that it allows tens of thousands to millions of compounds to be screened virtually in a matter of weeks.

The increasing number of PTP experimental structures resolved by X-ray crystallography has stimulated structure-guided efforts to identify small molecule PTP inhibitors. Drug discovery efforts focusing on PTPs are outlined in a comprehensive review written by Blaskovich, including detailed descriptions of the biological roles, target validation, screening tools and artifacts, and medicinal chemistry efforts, surrounding PTPs [19]. As outlined in this review, molecular modeling, structure-based design, and virtual screening efforts have primarily focused on hit generation and structure-guided optimization of hits for PTP1B [20,21,22,23,24,25,26,27,28,29]. A more recent study by Park and coworkers used structure-based virtual screening to identify nine PTP1B inhibitors with significant potency [30]. Utilizing the growing knowledge base from known PTP1B inhibitors, Suresh *et al.* reported the generation of a chemical feature-based pharmacophore hypothesis and its use for the identification of new lead compounds [31]. Additional PTPs were also approached using *in silico* methodologies. Of particular interest was the study by Hu et al., which targeted the identification of small molecule inhibitors for bacterial *Yersinia* YopH and *Salmonella* SptP through differentiation with PTP1B [32]. Virtual screening also identified small molecule inhibitors of LMWPTP, SHP-2, and Cdc25 [33,34,35]. A review by He and coworkers underscores the progress made to date in identifying small molecule tools for the functional interrogation of various PTPs, assisted by the computational tools [36]. In addition to the classes listed above, *in silico* screening also supported the identification of Lyp inhibitors, as described in three studies by Yu, Wu, and Stanford [37,38,39]. Importantly, the review by He articulates both the challenges and opportunities for developing PTP specific inhibitors, serving as chemical probes to augment the knowledge of PTP biology, and to establish the basis needed to approach other PTPs currently underexplored.

In this study, we identified small molecule inhibitors targeting the active site of PTPσ. We screened compounds *in silico* to identify structurally distinct scaffolds predicted to have the most desirable binding energies. These PTPσ virtual hits, as well as additional compounds identified by a substructure and similarity search (77 in total), were iteratively tested for inhibition of PTPσ

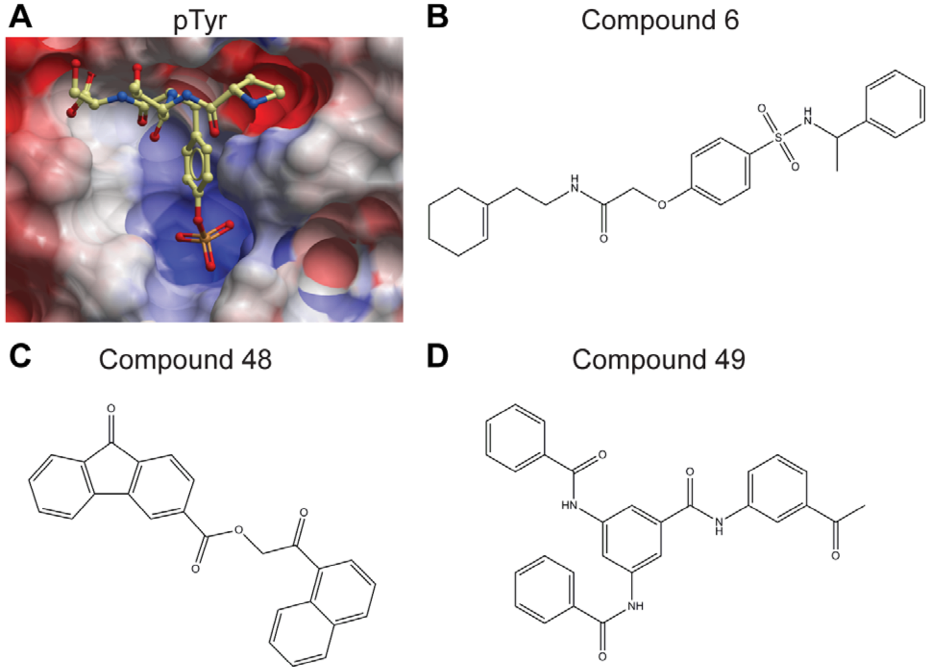

Figure 2. ***In silico*** **docking identifies compounds which dock into the D1 active site of PTPσ. (A)** The D1 domain of PTPσ docked a phosphotyrosine (p-Tyr) substrate into the active site. Surface resonance of the active site is displayed with negatively (red) and positively (blue) charged residues shown and substrate drawn in ball-and-stick form. Structures were generated with ICM software (MolSoft). **(B-D)** *In* silico screening identified structurally distinct scaffolds (compounds 6, 48, and 49), which molecularly dock into the active site, similar to the pTyr peptide. These compounds were chosen as a platform for subsequent studies based on their structural diversity and ability to inhibit PTPσ activity by at least 70% in a pilot phosphatase assay (at 10 μM), comparable to the pan PTP inhibitor, sodium orthovanadate (data not shown). Chemical structures created in ChemDraw. Compound 6: N-[2-(1-cyclohexen-1-yl)ethyl]-2-(4-{[(1-phenylethyl)amino]sulfonyl}phenoxy)acetamide. Compound 48: 2-(1-naphthyl)-2-oxoethyl 9-oxo-9H-fluorene-3-carboxylate. Compound 49: N-(3-acetylphenyl)-3,5-bis(benzoylamino)benzamide.
doi:10.1371/journal.pone.0050217.g002

in vitro (**Figure 1**). While we discovered 25 active compounds with micromolar potency against PTPσ, we discovered compounds frequently catalyzed the production of oxidative species in the assay buffer, a common culprit for non-selective PTP inhibition. By optimizing the biochemical screen to include oxidation constraints, we identified one lead compound which inhibited PTPσ by a mechanism that was oxidation-independent. This lead hit was capable of docking into the active site, suggesting it functions as a competitive inhibitor. The results of this study will be used as the foundation of future structure-based refinement of PTPσ inhibitors.

Results

In silico Docking Identifies Small Molecules Targeting the PTPσ D1 Active Site

The tandem phosphatase domains of PTPσ have been crystallized in their apo form [40]. We retrieved this structure from the protein data bank (PDB ID: 2fh7) and verified its utility by molecularly docking a phosphotyrosine peptide (NPTpYS) into the catalytically active D1 domain (**Figure 2A**). We hypothesized that the active site could be exploited in the development of competitive inhibitors targeted to PTPσ. To this end, we used the ZINC database to virtually screen a library of compounds for their ability to dock into the D1 domain of PTPσ [41]. From the top scoring compounds which were most favorably bound by the active site, we identified three compounds (Compounds 6, 48, and 49) which represented structurally distinct scaffolds and demonstrated an ability to inhibit PTPσ activity in preliminary *in vitro* assays (**Figure 2B–D**). To expand these into a set of compounds for biochemical investigation, we performed a substructure search and retrieved 74 additional molecules similar to these three scaffolds from the ChemBridge compound library. This entire collection of molecules, along with the established pan-PTP inhibitor sodium orthovanadate, were analyzed for their ability to inhibit PTPσ phosphatase activity *in vitro*.

To measure the catalytic activity of PTPσ *in vitro*, we utilized the chromogenic phosphatase substrate, *para*-nitrophenyl phosphate (pNPP). The dephosphorylated product para-nitrophenol (pNP), yields an intense yellow color under alkaline conditions measurable at 405 nm absorbance on a spectrophotometer (**Figure 3A**). We generated recombinant PTPσ and determined an amount (2 μg) that yielded linear pNP formation during the course of the phosphatase reaction while producing a maximal signal at least five-fold above background (**Figure 3B–C**). We then used initial velocities (in pNP absorbance per minute) measured across a series of pNPP substrate concentrations to calculate the K_m of PTPσ. The K_m of PTPσ was determined to be 250 μM (**Figure 3D–E**). When analyzing competitive inhibition, the mode of inhibition predicted for molecules binding the D1 active site, it is critical to use a substrate concentration at or below the K_m [42]. Accordingly, we used a pNPP substrate concentration less than 250 μM for inhibitor studies.

To profile the inhibition of PTPσ conferred by compounds, we pre-incubated recombinant PTPσ with each compound (100 μM) for 30 minutes, then initiated phosphatase reactions with the addition of pNPP for an additional 30 minutes. We identified 25 active compounds which inhibited PTPσ activity by 90% or more, a potency similar to that of sodium orthovanadate (Na_3VO_4) (**Figure 4A–C**). One of the scaffolds chosen *in silico*, compound 6,

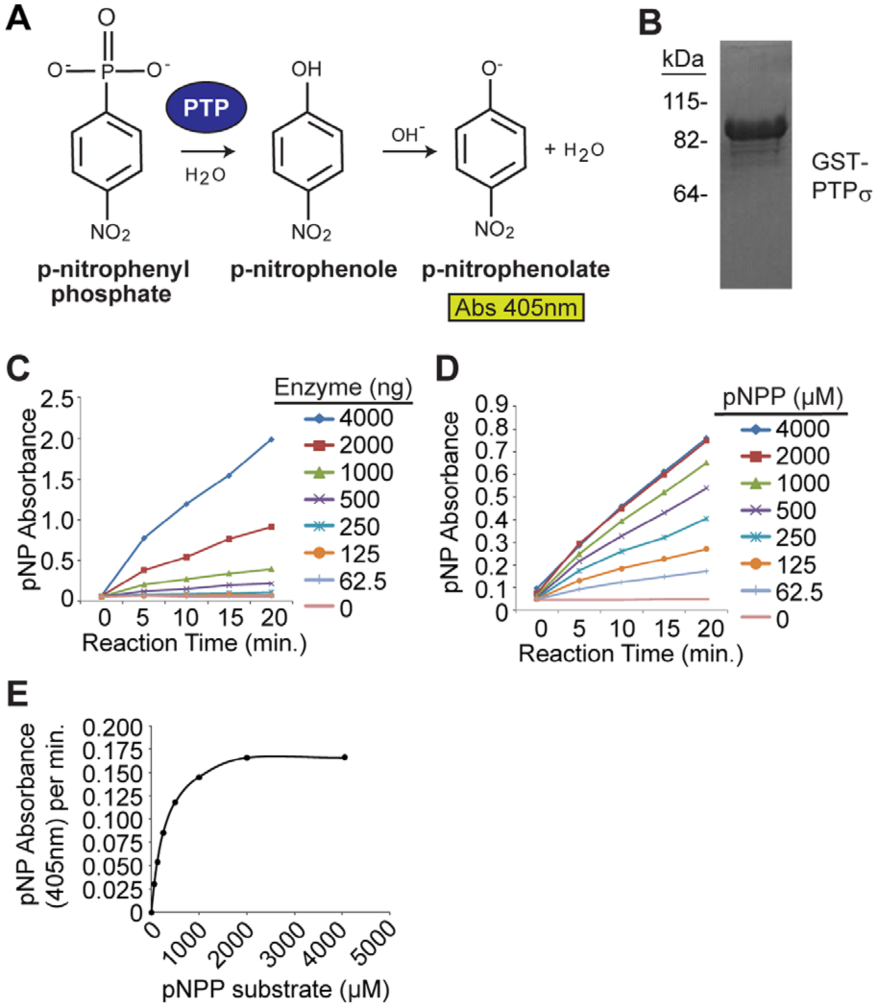

Figure 3. Optimization of biochemical screening conditions for PTPσ inhibition. (**A**) *Para*-nitrophenyl phosphate (pNPP) is a generic phosphatase substrate whose dephosphorylated product, para-nitrophenol (pNP), yields an intense yellow color under alkaline conditions measurable at 405 nm absorbance on a spectrophotometer. (**B**) 20 μg purified recombinant GST-PTPσ-CTF (C-terminal fragment containing the active sites) protein was resolved by SDS-PAGE and stained with coomassie blue to demonstrate purity. (**C**) The linear formation of product by various quantities of recombinant GST- PTPσ was observed through time-course reactions. pNPP-phosphatase assays were completed with a saturating dose of 1 mM pNPP. Background-corrected absorbance of dephosphorylated product are plotted by time of reaction. Each plot stems from the quantities of PTPσ indicated in the legend. (**D**) 2 μg enzyme was chosen from (A) for analysis of activity with varying doses of pNPP substrate. Each plot represents a unique dose of pNPP (indicated in the legend). Background-corrected absorbance of dephosphorylated product are plotted by time of reaction. (**E**) Initial velocities of PTPσ phosphatase activity (Y-axis; in pNP product formed per minute) were derived from the slopes of the plots in (D) at each of the indicated pNPP substrate concentrations (X-axis). From this, a Km of 250 μM is observed (denoted by dashed line).
doi:10.1371/journal.pone.0050217.g003

inhibited PTPσ to a lesser extent than the remaining *in silico* scaffolds, compounds 48 and 49. In fact, compounds chosen for structural similarities to compound 6 represented less than 15% of the active compounds. Therefore, we proceeded to follow up on compounds 48, 49, and similar structures.

Compounds inhibit PTPσ by non-selective oxidation. After identifying the most active compounds capable of inhibiting PTPσ *in vitro*, we explored the mechanism by which these molecules were reducing phosphatase activity. In particular, because PTP active sites are maintained in a reduced state for preservation of the nucleophilic cysteine which primes them for optimal activity, these enzymes are extremely sensitive to oxidation [43]. Oxidative species, such as hydrogen peroxide (H_2O_2), generated in the assay is a common culprit for decreased phosphatase activity [4]. To determine whether the reaction conditions were favoring H_2O_2-mediated inhibition of PTPσ, we repeated phosphatase assays in the presence or absence of catalase, an enzyme which converts H_2O_2 into water and oxygen (**Figure 5A**). We found that catalase negated all inhibition conferred by compounds 48 and 49 (**Figure 5B**).

Refined screen identifies hit with minimal oxidative effect. To identify compounds with minimal oxidative effects that may better represent true competitive inhibitors, we revisited small molecules predicted to bind the PTPσ active site *in silico*. We retrieved 63 additional molecules, representing diverse structures among the top 200 scoring compounds, and tested them under screening conditions optimized to significantly diminish the potential for H_2O_2 generation. To achieve these conditions, we used a low dose of compound (10 μM) and reduced the pre-incubation period to only 10 minutes, as H_2O_2 generation and inhibition is time-dependent [4]. Under these conditions, we discovered that two compounds, 36 and 38, inhibited PTPσ by

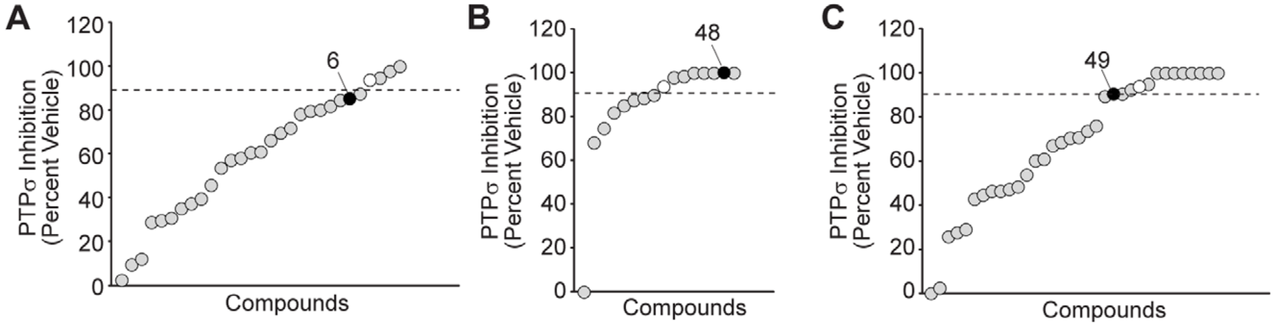

Figure 4. *In vitro* screen identifies active compounds which inhibit PTPσ. (**A–C**) The three *in silico*-identified scaffolds and 74 additional compounds identified by a sub-structure search of ChemBridge compounds for structural features relating to these scaffolds actives (A- similar to 6; B- similar to 48; C- similar to 49) were tested *in vitro* for potency of PTPσ. Compounds (at a final concentration of 100 μM) were pre-incubated with PTPσ for 30 minutes, then pNPP substrate added to a concentration of 200 μM and reactions continued for 30 minutes at 37°C. Dephosphorylated product was measured by its specific absorbance at 405 nm as a readout for PTPσ activity. Inhibition of PTPσ, expressed as a percent (normalized to vehicle, DMSO) is plotted for each compound. Sodium orthovanadate (Na_3VO_4) is a pan inhibitor of PTPs and was included as a positive control (white circles). Original scaffolds are indicated with black circles. Dashed lines denote a 90% inhibition threshold.

doi:10.1371/journal.pone.0050217.g004

40%, slightly more so than the equivalent dose of Na_3VO_4 (**Figure 5C**). We next assessed whether the inhibition mediated by these compounds involved H_2O_2 by determining dose-dependent inhibition in the presence and absence of catalase. Compound 38 conferred less than 50% inhibition of PTPσ at the maximal dose tested when incubated with catalase, suggesting a substantial oxidative effect (**Figure 5D**). Conversely, catalase had a less substantial effect on compound 36-mediated inhibition of PTPσ and in fact, could not prevent the inhibition conferred by relatively high doses of compounds (**Figure 5E**). This suggests that while H_2O_2 was partially contributing to PTPσ inhibition by compound 36, its effect was largely independent of oxidation. We used a dose-response of PTPσ inhibition to calculate the IC_{50} of compound 36 to be 10 μM (**Figure 6A**). To confirm that this molecule is capable of binding the active site of PTPσ, we molecularly docked compound 36 into the open conformation of the PTPσ D1 active site (**Figure 6B–C**). Importantly, the tyrosine-like moiety of compound 36 binds in the domain of PTPσ anticipated to bind the phosphotyrosine side chain of the known substrate.

Discussion

Taken together, this integrative approach of computational and biochemical methods led to the identification of several small molecule inhibitors of PTPσ. *In silico* docking demonstrated that these compounds were molecularly accommodated by the D1 active site of PTPσ, similar to a natural phosphotyrosine substrate, suggesting they function as competitive inhibitors. We confirmed that one potential active site lead molecule, compound 36 [1-(3,4-dichlorophenyl)-3-[(2-hydroxy-5-nitrophenyl)amino]-2-propen-1-one], inhibits PTPσ in a dose-dependent manner with an IC_{50} of 10 μM.

Oxidation and inhibition of PTP active sites by H_2O_2 has been well established as a physiological mode of regulation [44]. A number of compounds, in particular those containing quinones, have been documented to inhibit phosphatases through the generation of H_2O_2 species [4,45,46]. Although the precise mechanism was not characterized, the reversal of phosphatase inhibition by compounds 48 and 49 achieved by treatment with catalase provides evidence that for at least these compounds, inhibition is partially mediated through H_2O_2 generation. Oxidation does not discriminate selectively for the PTPσ active site and thus, is not an ideal mechanism of inhibition for a PTPσ inhibitor. To address this, we optimized assay conditions to eliminate oxidative effects and found that compound 36 was able to inhibit PTPσ by a mechanism largely independent of oxidation. This suggests that compound 36 functions as a competitive inhibitor of PTPσ and in agreement with this, it docked favorably into the D1 active site of PTPσ *in silico*.

Although compound 36 proved potent and non-oxidative, we do not anticipate that it will be a selective inhibitor of PTPσ in its current form, owing to the high degree of sequence conservation among phosphatase catalytic domains. In particular, the residues forming the active site predominantly lie within highly conserved motifs showing little sequence variability across the entire PTP family [47]. In fact, preliminary studies suggest compound 36 displays activity towards PTP1B, in addition to PTPσ (unpublished data). This underscores the importance of our future efforts to identify and create modifications to the compound 36 scaffold which will favor selective inhibition of PTPσ.

We believe a combination of *in silico* methods and carefully optimized biochemical screening (i.e., an assay that minimizes inhibition by oxidative species) represents an useful approach to develop effective PTP inhibitors. Through the *in silico* approach described here, we were able to identify active phosphatase scaffolds while bypassing a primary assay that would entail a high-throughput biochemical screening of compounds *in vitro*. Coupling this effort with biochemical assays, we prioritized compound 36 as a lead molecule. Our future studies will include structure-based refinement of this scaffold in order to develop selective inhibitors of PTPσ. In this approach, we will characterize the activity of compound 36 against related PTPs and following, use molecular docking and structural analyses of these counter-targets to identify chemical modifications that promote selectivity for PTPσ.

Methods

Structural Modeling and Phosphotyrosine Substrate Docking

The crystal structure of PTPσ (PDB ID: 2FH7) was retrieved from the Protein Data Bank. The initial conformations of p-Tyr peptide (NPTpYS) were extracted from the CD45-p-Tyr peptide complex structure (PDB ID: 1YGU). The ICM program was used for protein and substrate preparation (MolSoft, La Jolla, CA). Phosphotyrosine peptide was docked into the active site of PTPσ with default parameters implemented in the ICM program.

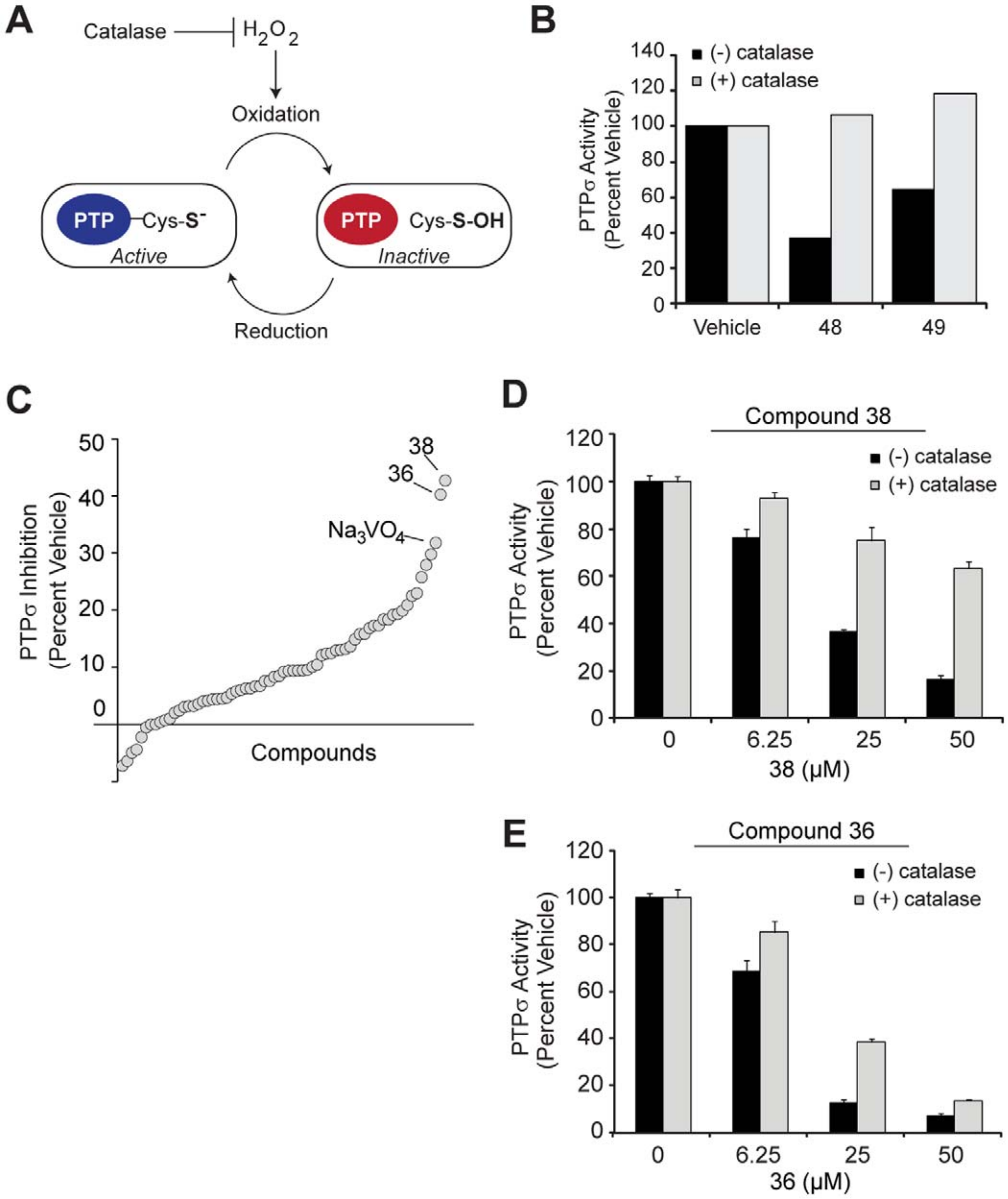

Figure 5. Refined biochemical screen with oxidation constraints identifies a non-oxidative molecule. (**A**) Catalase quenches hydrogen peroxide (H_2O_2), an oxidative species which inhibits PTP active sites through oxidation of the active site cysteine. (**B**) PTPσ activity towards pNPP was measured in the presence of DMSO vehicle, compound 48, or compound 49 as described previously. Bovine liver catalase (50 units per reaction) was included (+, gray bars) to degrade hydrogen peroxide, or excluded (−, black bars). Relative PTPσ activity was plotted (percent of activity in DMSO with or without catalase). (**C**) Sixty-six scaffolds identified *in silico* were evaluated using conditions optimized to minimize the effects of oxidation (H_2O_2). Compounds (10 μM) were pre-incubated with PTPσ for 10 min at 37°C then 225 μM substrate added for 15 minutes. PTPσ inhibition is plotted (normalized to vehicle, DMSO) and compounds are displayed by rank (increasing inhibition left to right). Most potent inhibitors, 36 and 38, are highlighted, as is the PTP inhibitor, Na_3VO_4, for reference. (**D–E**) PTPσ inhibition was measured as in (C) with compounds 38 (B) and 36 (C) with (+, gray bars) or without (−, black bars) the addition of catalase to quench hydrogen peroxide. Error bars represent standard deviation.
doi:10.1371/journal.pone.0050217.g005

Virtual Screening (VS)

We used the ZINC library (version 8; University of California San Francisco) of ChemBridge compounds for virtual screening with the D1 active site of PTPσ (PDB ID: 2FH7). GOLD (Version 3.2) program was used for virtual screening and ChemScore scoring function was used to rank the top 200 hits with favorable binding energies (Cambridge Crystallographic Data Centre, Cambridge). Hydrogen bond restraints were used during molecular docking process. Molecules which formed at least one potential hydrogen bond with any of the residues, S1590, A1591, V1593, G1594 or R1595, were given higher weight during the score calculation. We used ICM clustering analysis (MolSoft) to identify 66 representative compounds from unique clustering groups. A substructure and similarity search based on compounds 6, 48, and 49 was performed using the Canvas module in Schrodinger (Schrödinger, LLC, New York, NY, 2011) and the ChemBridge compound online search engine (ChemBridge, San Diego, CA) to identify 74 additional leads.

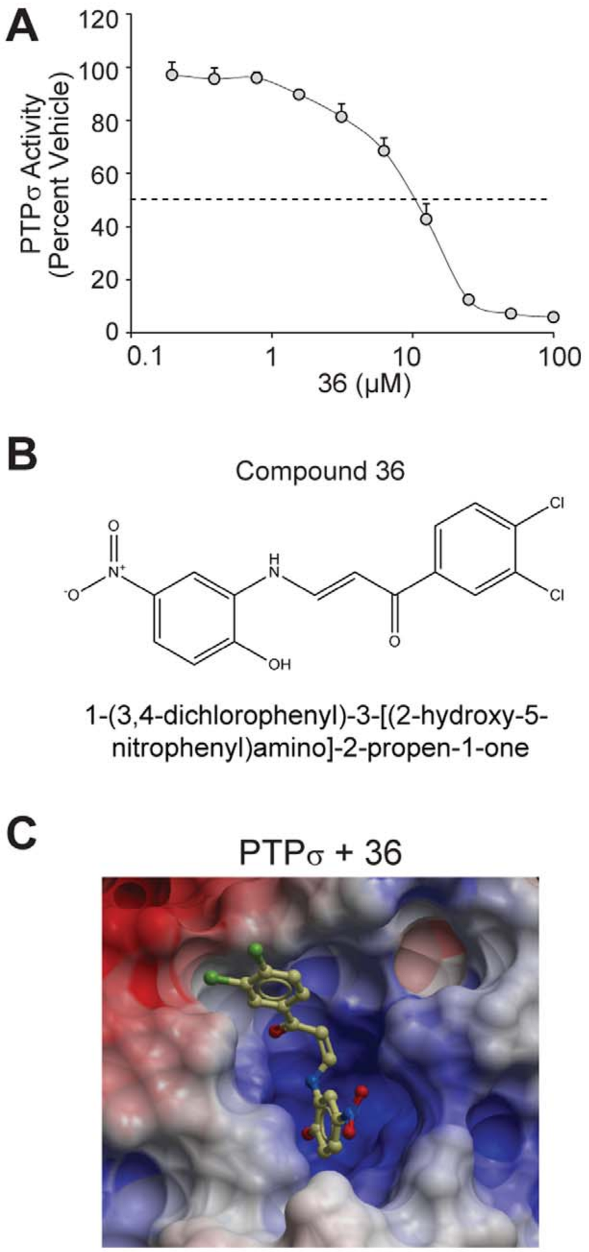

Figure 6. Compound 36 is a μM inhibitor of PTPσ and binds the PTPσ active site *in silico.* (**A**) Compound 36 was tested for inhibition of PTPσ. Compound 36 (at a final concentration from 0 to 100 μM) was pre-incubated with PTPσ for 10 min at 37°C. Reactions were then performed for 10 minutes at 37°C following the addition of 225 μM pNPP substrate. Relative PTPσ activity is plotted (percent of activity in DMSO). Dashed line indicates 50% inhibition (10 μM). Bars represent standard deviation from three experiments. (**B**) The structure of compound 36 is displayed. (**C**) Compound 36 was docked into the active site of PTPσ (PDB ID: 2FH7) using the D1 apo crystal structure. Molecular surface is colored by electrostatic potential. Red corresponds to negative potential and blue to positive potential. Docking was performed using the Schrödinger suite of software as described in *Methods* and figures generated using ICM (MolSoft).
doi:10.1371/journal.pone.0050217.g006

In vitro Phosphatase Assays

Compounds identified *in silico* were purchased from ChemBridge and diluted to 5 or 10 mM in DMSO. GST-tagged recombinant PTPσ containing all residues C-terminal to the transmembrane domain (BC104812 cDNA; aa 883-1501) was generated in pGEXKG [48]. GST-tagged recombinant full-length PTP1B (BC018164) was generated with a 6xHIS tag in pGEXKG. Proteins were purified from BL21 Escherichia coli after isopropyl β-D-1-thiogalactopyranoside (IPTG) induction and purity was confirmed by SDS-PAGE and coomassie blue staining. Compounds were pre-incubated with recombinant enzymes in freshly prepared phosphatase buffer (50 mM sodium acetate, 25 mM Tris-HCl, 3 mM DTT, pH 6.5) for 10 to 30 minutes, as indicated in figure legends. Following, *para*-nitrophenyl phosphate (pNPP; Sigma S0942), initially diluted in assay buffer, was added to reactions for a final volume of 100 μl and reactions were carried out in a 37°C water bath for 15 to 30 minutes. Reactions were quenched with 100 μl 1N sodium hydroxide (NaOH) and 180 μl was transferred to flat-bottom clear 96-well plates. Absorbance of pNP product at 405 nm was measured on a spectrophotometer and plotted. Background absorbance values of compound-only wells were subtracted from the corresponding reactions. DMSO was included as a vehicle control. The IC_{50} value of compound 36 was calculated using the data from Figure 6A and BioDataFit (Chang Biosciences, Castro Valley, CA).

Docking of Compound 36 into PTPσ

Compound 36 was docked to the open conformation of PTPσ (PDB ID: 2FH7) which was retrieved from the Protein Data Bank. Docking was performed using Schrödinger's graphical user interface Maestro (Maestro, version 9.2, Schrödinger, LLC, New York, NY, 2011). The protein was first processed using protein preparation wizard, which assigned bond orders, and added hydrogens and missing atoms, followed by minimization. Compound 36 was prepared in LigPrep (LigPrep, version 2.5, Schrödinger, LLC, New York, NY, 2011) module of Schrödinger in the OPLS-2005 force field [49] generating possible ionization states and stereoisomers for the ligand. Docking of the ligand was performed in Glide module (Glide, version 5.7, Schrödinger, LLC, New York, NY, 2011). A receptor grid was generated, defining the binding site of PTPσ, and the prepared ligand was docked using extra precision scoring function while keeping the ligand flexible. Several poses were generated which were then minimized to optimize them further using MacroModel within the OPLS2005 force field (MacroModel, version 9.9, Schrödinger, LLC, New York, NY, 2011). For Figure 6C, complexes were exported into ICM (MolSoft) and surface representations generated.

Author Contributions

Conceived and designed the experiments: KRM PN YX AK JP NM HEX JM. Performed the experiments: KRM PN YX AK NM JM. Analyzed the data: KRM PN YX AK HEX NM JM. Wrote the paper: KRM PN YX HEX NM JM.

References

1. Lahiry P, Torkamani A, Schork NJ, Hegele RA (2010) Kinase mutations in human disease: interpreting genotype-phenotype relationships. Nat Rev Genet 11: 60–74.
2. Tonks NK (2006) Protein tyrosine phosphatases: from genes, to function, to disease. Nat Rev Mol Cell Biol 7: 833–846.
3. Tautz L, Pellecchia M, Mustelin T (2006) Targeting the PTPome in human disease. Expert Opin Ther Targets 10: 157–177.
4. Tautz L, Mustelin T (2007) Strategies for developing protein tyrosine phosphatase inhibitors. Methods 42: 250–260.
5. Zhang ZY (2002) Protein tyrosine phosphatases: structure and function, substrate specificity, and inhibitor development. Annu Rev Pharmacol Toxicol 42: 209–234.
6. Shen K, Keng YF, Wu L, Guo XL, Lawrence DS, et al. (2001) Acquisition of a specific and potent PTP1B inhibitor from a novel combinatorial library and screening procedure. J Biol Chem 276: 47311–47319.
7. Sun JP, Fedorov AA, Lee SY, Guo XL, Shen K, et al. (2003) Crystal structure of PTP1B complexed with a potent and selective bidentate inhibitor. J Biol Chem 278: 12406–12414.
8. McLean J, Batt J, Doering LC, Rotin D, Bain JR (2002) Enhanced rate of nerve regeneration and directional errors after sciatic nerve injury in receptor protein tyrosine phosphatase sigma knock-out mice. J Neurosci 22: 5481–5491.
9. Thompson KM, Uetani N, Manitt C, Elchebly M, Tremblay ML, et al. (2003) Receptor protein tyrosine phosphatase sigma inhibits axonal regeneration and the rate of axon extension. Mol Cell Neurosci 23: 681–692.
10. Sapieha PS, Duplan L, Uetani N, Joly S, Tremblay ML, et al. (2005) Receptor protein tyrosine phosphatase sigma inhibits axon regrowth in the adult injured CNS. Mol Cell Neurosci 28: 625–635.
11. Siu R, Fladd C, Rotin D (2007) N-cadherin is an in vivo substrate for protein tyrosine phosphatase sigma (PTPsigma) and participates in PTPsigma-mediated inhibition of axon growth. Mol Cell Biol 27: 208–219.
12. Faux C, Hawadle M, Nixon J, Wallace A, Lee S, et al. (2007) PTPsigma binds and dephosphorylates neurotrophin receptors and can suppress NGF-dependent neurite outgrowth from sensory neurons. Biochim Biophys Acta 1773: 1689–1700.
13. Shen Y, Tenney AP, Busch SA, Horn KP, Cuascut FX, et al. (2009) PTPsigma is a receptor for chondroitin sulfate proteoglycan, an inhibitor of neural regeneration. Science 326: 592–596.
14. Fry EJ, Chagnon MJ, Lopez-Vales R, Tremblay ML, David S Corticospinal tract regeneration after spinal cord injury in receptor protein tyrosine phosphatase sigma deficient mice. Glia 58: 423–433.
15. MacKeigan JP, Murphy LO, Blenis J (2005) Sensitized RNAi screen of human kinases and phosphatases identifies new regulators of apoptosis and chemoresistance. Nat Cell Biol 7: 591–600.
16. Martin KR, Xu Y, Looyenga BD, Davis RJ, Wu CL, et al. (2011) Identification of PTPsigma as an autophagic phosphatase. J Cell Sci 124: 812–819.
17. Mattila E, Ivaska J (2011) High-throughput methods in identification of protein tyrosine phosphatase inhibitors and activators. Anticancer Agents Med Chem 11: 141–150.
18. Kitchen DB, Decornez H, Furr JR, Bajorath J (2004) Docking and scoring in virtual screening for drug discovery: methods and applications. Nat Rev Drug Discov 3: 935–949.
19. Blaskovich MA (2009) Drug discovery and protein tyrosine phosphatases. Curr Med Chem 16: 2095–2176.
20. Sarmiento M, Wu L, Keng YF, Song L, Luo Z, et al. (2000) Structure-based discovery of small molecule inhibitors targeted to protein tyrosine phosphatase 1B. J Med Chem 43: 146–155.
21. Doman TN, McGovern SL, Witherbee BJ, Kasten TP, Kurumbail R, et al. (2002) Molecular docking and high-throughput screening for novel inhibitors of protein tyrosine phosphatase-1B. J Med Chem 45: 2213–2221.
22. Murthy VS, Kulkarni VM (2002) 3D-QSAR CoMFA and CoMSIA on protein tyrosine phosphatase 1B inhibitors. Bioorg Med Chem 10: 2267–2282.
23. Wang J, Chan SL, Ramnarayan K (2003) Structure-based prediction of free energy changes of binding of PTP1B inhibitors. J Comput Aided Mol Des 17: 495–513.
24. Floriano WB, Vaidehi N, Zamanakos G, Goddard WA, 3rd (2004) HierVLS hierarchical docking protocol for virtual ligand screening of large-molecule databases. J Med Chem 47: 56–71.
25. Yang C, Cross K, Myatt GJ, Blower PE, Rathman JF (2004) Building predictive models for protein tyrosine phosphatase 1B inhibitors based on discriminating structural features by reassembling medicinal chemistry building blocks. J Med Chem 47: 5984–5994.
26. Sobhia ME, Bharatam PV (2005) Comparative molecular similarity indices analysis (CoMSIA) studies of 1,2-naphthoquinone derivatives as PTP1B inhibitors. Bioorg Med Chem 13: 2331–2338.
27. Shim YS, Kim KC, Lee KA, Shrestha S, Lee KH, et al. (2005) Formylchromone derivatives as irreversible and selective inhibitors of human protein tyrosine phosphatase 1B. Kinetic and modeling studies. Bioorg Med Chem 13: 1325–1332.
28. Taha MO, AlDamen MA (2005) Effects of variable docking conditions and scoring functions on corresponding protein-aligned comparative molecular field analysis models constructed from diverse human protein tyrosine phosphatase 1B inhibitors. J Med Chem 48: 8016–8034.
29. Hu × (2006) In silico modeling of protein tyrosine phosphatase 1B inhibitors with cellular activity. Bioorg Med Chem Lett 16: 6321–6327.
30. Park H, Bhattarai BR, Ham SW, Cho H (2009) Structure-based virtual screening approach to identify novel classes of PTP1B inhibitors. Eur J Med Chem 44: 3280–3284.
31. N Suresh NV (2010) Pharmacophore Modeling and Virtual Screening Studies to Design Potential Protein Tyrosine Phosphatase 1B Inhibitors as New Leads. J Proteomics Bioinform 3.1: 020–028.
32. Hu X, Vujanac M, Stebbins CE (2004) Computational analysis of tyrosine phosphatase inhibitor selectivity for the virulence factors YopH and SptP. J Mol Graph Model 23: 175–187.
33. Vidal D, Blobel J, Perez Y, Thormann M, Pons M (2007) Structure-based discovery of new small molecule inhibitors of low molecular weight protein tyrosine phosphatase. Eur J Med Chem 42: 1102–1108.
34. Hellmuth K, Grosskopf S, Lum CT, Wurtele M, Roder N, et al. (2008) Specific inhibitors of the protein tyrosine phosphatase Shp2 identified by high-throughput docking. Proc Natl Acad Sci U S A 105: 7275–7280.
35. Lavecchia A, Cosconati S, Limongelli V, Novellino E (2006) Modeling of Cdc25B dual specifity protein phosphatase inhibitors: docking of ligands and enzymatic inhibition mechanism. ChemMedChem 1: 540–550.
36. He R, Zeng LF, He Y, Zhang S, Zhang ZY (2012) Small molecule tools for functional interrogation of protein tyrosine phosphatases. FEBS J.
37. Yu X, Sun JP, He Y, Guo X, Liu S, et al. (2007) Structure, inhibitor, and regulatory mechanism of Lyp, a lymphoid-specific tyrosine phosphatase implicated in autoimmune diseases. Proc Natl Acad Sci U S A 104: 19767–19772.
38. Wu S, Bottini M, Rickert RC, Mustelin T, Tautz L (2009) In silico screening for PTPN22 inhibitors: active hits from an inactive phosphatase conformation. ChemMedChem 4: 440–444.
39. Stanford SM, Krishnamurthy D, Falk MD, Messina R, Debnath B, et al. (2011) Discovery of a novel series of inhibitors of lymphoid tyrosine phosphatase with activity in human T cells. J Med Chem 54: 1640–1654.
40. Almo SC, Bonanno JB, Sauder JM, Emtage S, Dilorenzo TP, et al. (2007) Structural genomics of protein phosphatases. J Struct Funct Genomics 8: 121–140.
41. Irwin JJ, Shoichet BK (2005) ZINC–a free database of commercially available compounds for virtual screening. J Chem Inf Model 45: 177–182.
42. Tierno MB, Johnston PA, Foster C, Skoko JJ, Shinde SN, et al. (2007) Development and optimization of high-throughput in vitro protein phosphatase screening assays. Nat Protoc 2: 1134–1144.
43. Tonks NK (2005) Redox redux: revisiting PTPs and the control of cell signaling. Cell 121: 667–670.
44. Salmeen A, Andersen JN, Myers MP, Meng TC, Hinks JA, et al. (2003) Redox regulation of protein tyrosine phosphatase 1B involves a sulphenyl-amide intermediate. Nature 423: 769–773.
45. Urbanek RA, Suchard SJ, Steelman GB, Knappenberger KS, Sygowski LA, et al. (2001) Potent reversible inhibitors of the protein tyrosine phosphatase CD45. J Med Chem 44: 1777–1793.
46. Bova MP, Mattson MN, Vasile S, Tam D, Holsinger L, et al. (2004) The oxidative mechanism of action of ortho-quinone inhibitors of protein-tyrosine phosphatase alpha is mediated by hydrogen peroxide. Arch Biochem Biophys 429: 30–41.
47. Andersen JN, Mortensen OH, Peters GH, Drake PG, Iversen LF, et al. (2001) Structural and evolutionary relationships among protein tyrosine phosphatase domains. Mol Cell Biol 21: 7117–7136.
48. Guan KL, Dixon JE (1991) Eukaryotic proteins expressed in Escherichia coli: an improved thrombin cleavage and purification procedure of fusion proteins with glutathione S-transferase. Anal Biochem 192: 262–267.
49. Kaminski GA, Friesner RA, Tirado-Rives J, Jorgensen WL (2001) Evaluation and Reparametrization of the OPLS-AA Force Field for Proteins via Comparison with Accurate Quantum Chemical Calculations on Peptides†. The Journal of Physical Chemistry B 105: 6474–6487.